Mechanisms of APOE4-Driven Pathogenesis in Alzheimer's Disease and Related Therapeutic Approaches

by
Nicole Koutsodendris

DISSERTATION
Submitted in partial satisfaction of the requirements for degree of
DOCTOR OF PHILOSOPHY

in

Developmental and Stem Cell Biology

in the

GRADUATE DIVISION
of the
UNIVERSITY OF CALIFORNIA, SAN FRANCISCO

Approved:

DocuSigned by:
Jorge Palop
662299671EC0437...

Jorge Palop
Chair

DocuSigned by:
Yadong Huang
DocuSigned by:

Yadong Huang

DocuSigned by:
Lea Grinberg
DocuSigned by:

Lea Grinberg

DocuSigned by:
Sheng Ding
8CDD680BE3E24BD...

Sheng Ding

Committee Members

ACKNOWLEDGMENTS

This thesis was a culmination of effort and support provided by a community of mentors, colleagues, friends, and family. I would like to first thank my mentor, Yadong Huang, who spent an exorbitant amount of time over the past five years supporting my ambitions and reviewing every miniscule detail of my grant applications and manuscripts to ensure they are of high quality. Yadong's endless support and encouragement have allowed me to develop into a rigorous scientist and he has provided me with many invaluable lessons and wisdoms that will guide me for the rest of my career. Second, I would like to thank the wonderful members of the Huang lab for their constant support. I joined the Huang lab at the same time as Antara Rao and Maxine Nelson and we have embarked on this incredible, and at times tumultuous, PhD journey together and I could not even imagine going through my PhD without my best friends working by my side. My younger mentees, Jessica Blumenfeld and Oscar Yip, enriched our lab community when they joined and made lab work much more fun with our brain section mounting parties, themed dress days, and chocolate breaks. Theodora Pak has also been incredibly helpful in planning and organizing important lab-related events throughout my PhD. Third, I would like to that my qualifying exam and thesis committee members - Dr. Robert Mahley, Dr. Jorge Palop, Dr. Lea Grinberg, and Dr. Sheng Ding. These members asked thought-provoking and insightful questions while also offering helpful suggestions and feedback that undoubtably strengthened my scientific work. Fourth, I would like to thank my mother, Alexandra Papageorgiou, for providing her unrelenting love and support and for cheering me on through every little victory. Fifth, I would like to thank my boyfriend, Ryan C. Farber, for his enormous support throughout this very long venture by surprising me with ice cream after a long day at work and making me laugh even on my toughest days. Finally, I would like to thank the students, faculty, and administrators of the DSCB and Gladstone community. Being in such a supportive environment surrounded by amazing colleagues and friends made my graduate experience all the more rewarding.

CONTRIBUTIONS

Chapter I contains text and figures for a manuscript that is currently under revision. Yadong Huang and I designed and coordinated the studies and wrote the manuscript. I performed the majority of studies and data analyses. Jesscia Blumenfeld aided tissue collection and processing and helped on some immunohistochemical studies and data collection. Ayushi Agrawal and Michela Traglia performed the majority of the snRNA-seq analysis. Brian Grone performed some of the snRNA-seq analysis. Misha Zilberter collected and analyzed the electrophysiological data. Oscar Yip, Antara Rao, and Maxine R. Nelson helped on some immunohistochemical studies and data collection. Yanxia Hao. isolated cell nuclei and prepared samples for snRNA sequencing. Reuben Thomas provided guidance on snRNA-seq analyses. Ayushi Agrawal, Michela Traglia, and Reuben Thomas developed and implemented the two Generalized Linear Mixed Effects Models of the snRNA-seq. Seo Yeon Yoon and Patrick Arriola managed all mouse lines and helped on mouse brain collection. Theodora Pak provided editorial assistance. Yadong Huang supervised the project.

Chapter II contains text and figures that are currently under preparation for submission. Yadong Huang and I designed and coordinated the studies and wrote the manuscript. I performed the majority of studies and data analyses. Jessica Blumenfeld conducted the microdialysis surgeries and ISF collection and helped on some immunohistochemical studies and data collection. Ayushi Agrawal, Michela Traglia, Brian Grone, Yanxia Hao, Reuben Thomas, and Misha Zilberter performed some of the data analyses. Oscar Yip, Antara Rao, and Maxine R. helped on some immunohistochemical studies and data collection. Antara Rao also helped on some of the HMGB1 inhibitor injections. Seo Yeon Yoon and Patrick Arriola managed all mouse lines, helped on mouse brain collection, and performed some of the HMGB1 inhibitor injections. Theodora Pak provided editorial assistance. Yadong Huang supervised the project.

Mechanisms of APOE4-Driven Alzheimer's Disease Pathogenesis and Related Therapeutic Approaches

Nicole Koutsodendris

Abstract

Apolipoprotein E4 (*APOE4*) is the strongest known genetic risk factor for late-onset Alzheimer's disease (AD), however, its pathogenic mechanisms remain unclear. We performed in-depth studies on two intriguing, yet understudied, features of APOE4 pathogenesis to better understand their roles in promoting AD. First, APOE can be produced in a variety of cell types and may exert different pathological effects depending on its cellular source. We report a rigorous characterization of neuronal APOE4 effects on prominent AD-related pathologies by selectively removing APOE4 from neurons in an APOE4-expressing tauopathy mouse model. We found that removal of neuronal APOE4 led to a drastic reduction in Tau pathology, gliosis, neurodegeneration, neurodysfunction, and myelin deficits and eliminated disease-associated subpopulations of neurons, oligodendrocytes, astrocytes, and microglia that were enriched in APOE4-expressing tauopathy mice. Thus, neuronal APOE4 plays a central role in promoting the development of major AD pathologies. Second, APOE4 has been shown to be an important driver of Tau pathology, gliosis and degeneration in AD but the mechanisms underlying these APOE4-driven pathological effects remain elusive. We demonstrated in a tauopathy mouse model that APOE4 promotes significantly more nucleo-cytoplasmic translocation and release of high mobility group box 1 (HMGB1) from hippocampal neurons than APOE3. Treatment of APOE4-expressing tauopathy mice with HMGB1 inhibitors effectively blocked the nucleo-cytoplasmic translocation of HMGB1 and ameliorated the development of prominent APOE4-driven AD pathologies. Notably, treatment of APOE3-expressing tauopathy mice with HMGB1 inhibitors did not show significant beneficial effects on these pathological parameters. Thus, APOE4 drives Tau-mediated gliosis and degeneration by promoting neuronal HMGB1 release, and HMGB1 inhibitors represent a promising approach for treating APOE4-related AD and other tauopathies.

This thesis is dedicated to my mother, Alexandra Papageorgiou,

and father, Dimitrios Koutsodendris

TABLE OF CONTENTS

LIST OF FIGURES

Chapter I

LIST OF FIGURES

Chapter II

INTRODUCTION

Alzheimer's Disease and Apolipoprotein E4

Alzheimer's disease (AD) is a highly prevalent neurodegenerative disorder that involves extensive memory loss and cognitive deficits[1]. Currently, there are no viable therapeutic options to slow AD progression[2], which is likely due to an incomplete understanding of its pathogenic mechanisms. Alzheimer's disease (AD) is a major type of tauopathy that is characterized the accumulation of amyloid plaques and Tau tangles[1,3]. Of these two major AD pathological hallmarks, Tau tangles have the strongest correlation with neurodegeneration and cognitive decline[4–7]. Other AD pathological hallmarks that have been understudied include neuroinflammation and gliosis, which have recently been shown to be key drivers of neurodegeneration[8,9]. Additionally, oligodendrocyte deficits and myelin degeneration have been observed in human AD brains[10–12] and in mouse models of AD and tauopathy[13–15]. Thus, AD is a multifactorial disorder that consists of a complex set of pathologies. However, the connections between these pathologies and the mechanisms responsible for their induction or exacerbation remain unclear.

Epidemiological and genome-wide association studies have identified apolipoprotein E4 (*APOE4*) as the strongest genetic risk factor for late-onset AD[16–18]. The human *APOE* gene exists as three common alleles, including $\varepsilon 2$, $\varepsilon 3$, and $\varepsilon 4$. *APOE* $\varepsilon 4$ is considered the most detrimental allele as it dose-dependently increases AD risk and decreases the age of disease onset[16–19]. The lifetime risk estimate of developing AD by the age of 85 is ~10% in apoE3 homozygotes, ~30% in apoE4 heterozygotes, and ~65% in apoE4 homozygotes[20]. ApoE4 homozygosity also decreases the mean age of onset for AD from 84 to 68 years old, emphasizing the importance of apoE4 in AD pathogenesis[21]. This illustrates that APOE4 an important genetic factor linked to increasing AD risk and establishes the importance of understanding its pathogenic mechanisms.

APOE4-Promoted AD Pathologies

There is considerable evidence supporting the notion that APOE4 and APOE3 have vastly different effects on numerous AD pathologies. APOE4 has also been shown to impact such as Aβ fibrillization and clearance[22–24], leading to dramatic increase in the amount of fibrillar Aβ deposits and neuritic plaques relative to APOE3 in apoE/hAPP$_{FAD}$ mice[25]. In addition, APOE4 promotes Tau phosphorylation and aggregation relative to APOE3, as PS19-E4 mice displayed an increase in p-tau staining patterns associated with greater brain atrophy than PS19-E3 mice[26–29]. APOE4 has also been linked to glial dysfunction [30,31], with APOE4 mice exhibiting increased glial activation and cytokine release than APOE3 mice[32,33].

APOE4 also has a potent effect on neurodegeneration and neuronal loss, as structural MRI imaging of APOE4 carriers shows they exhibit accelerated hippocampal volumetric loss in early lifespan and accelerated cortical atrophy in midlife[34]. Furthermore, APOE4-KI mice display an age-dependent loss of hippocampal neurons and extensive learning and memory deficits relative to APOE3-KI mice[35,36]. Although it is unclear exactly how APOE4 induces neurodegeneration, recent studies have shown that APOE4 increases inflammation and gliosis [37,38] and indicated that gliosis is a strong driver of APOE4-related neurodegeneration[9]. Still, the underlying cellular and molecular mechanisms responsible for APOE4-induced gliosis and subsequent neurodegeneration are unknown.

Cellular Source-Dependent Pathogenic Effects of APOE4

Recently, there has been increasing interest in establishing the cell type-specific effects of APOE4 in AD pathogenesis. Within the central nervous system (CNS), APOE is produced by a variety of cell types and previous studies have indicated that APOE exerts different pathological effects depending on its cellular source[27,39–41]. APOE acts as he main lipid transporter in the CNS and it is mainly produced by astrocytes in the CNS. Still, a previous study using EGFP as real-time

location marker of apoE expression *in* vivo observed that kainic acid treatment induces intense apoE-GFP expression in injured neurons, demonstrating that neurons upregulate apoE expression in response to excitotoxic injury[42]. This begs the question of whether the cellular source of apoE determine its pathogenicity.

Recent findings have implicated astrocytic APOE4 in the pathogenesis of AD, as genetic deletion of APOE4 in astrocytes led to a reduction of various AD-related pathologies, including Tau pathology, neurodegeneration, and gliosis[40]. Still, there is an incomplete understanding of the role of neuronal APOE4 in the pathogenesis of AD. Previous studies from our lab have suggested that neuronal APOE4 is important to some AD-related processes, as neuronal APOE4 overexpression increases pTau levels in APOE-KI mice[27] and the removal of neuronal APOE4 prevents inhibitory neuron loss and cognitive deficits in APOE4 knock-in (APOE4-KI) mice with age[39]. However, it is still unclear if neuronal APOE4 represents a key pathogenic factor driving the development of full-scale AD pathologies. It is critically important to elucidate the exact role of neuronal APOE4 in the pathogenesis of AD to gain a better understanding of the cellular source-specific mechanisms that drive the detrimental effects of APOE4 and to potentially reveal new therapeutic targets to combat APOE4-related AD.

References

1. Huang, Y. & Mucke, L. Alzheimer mechanisms and therapeutic strategies. *Cell* **148,** 1204–1222 (2012).
2. Marasco, R. A. Current and evolving treatment strategies for the Alzheimer disease continuum. *Am J Manag Care* **26**, S167–S176 (2020).
3. Rajan, K. B. *et al.* Population estimate of people with clinical Alzheimer's disease and mild cognitive impairment in the United States (2020-2060). *Alzheimers Dement* **17**, 1966–1975 (2021).
4. Josephs, K. A. *et al.* Beta-amyloid burden is not associated with rates of brain atrophy. *Ann Neurol* **63**, 204–212 (2008).
5. Cho, H. *et al.* In vivo cortical spreading pattern of tau and amyloid in the Alzheimer disease spectrum. *Ann Neurol* **80**, 247–258 (2016).
6. Scholl, M. *et al.* PET imaging of tau deposition in the aging human brain. *Neuron* **89**, 971–982 (2016).
7. Ossenkoppele, R. *et al.* Tau PET patterns mirror clinical and neuroanatomical variability in Alzheimer's disease. *Brain* **139**, 1551–1567 (2016).
8. Leyns, C. E. G. & Holtzman, D. M. Glial contributions to neurodegeneration in tauopathies. *Mol Neurodegender* **12**, 50 (2017).
9. Shi, Y. *et al.* Microglia drive APOE-dependent neurodegeneration in a tauopathy mouse model. *J Exp Med* **216**, 2546–2561 (2019).
10. Benitez, A. *et al.* White matter tract integrity metrics reflect the vulnerability of late-myelinating tracts in Alzheimer's disease. *Neuroimage Clin* **4**, 64–71 (2013).
11. Dean III, D. C. *et al.* Association of amyloid pathology with myelin alteration in preclinical Alzheimer disease. *JAMA Neurol* **74**, 41–49 (2017).
12. Nasrabady, S. E., Rizvi, B., Goldman, J. E. & Brickman, A. M. White matter changes in Alzheimer's disease: a focus on myelin and oligodendrocytes. *Acta Neuro Comms* **6**, 22 (2018).

13. Desai, M. K. *et al.* Triple-transgenic Alzheimer's disease mice exhibit region-specific abnormalities in brain myelination patterns prior to appearance of amyloid and tau pathology. *Glia* **57**, 54–65 (2009).

14. Zhang, X. *et al.* Oligodendroglial glycolytic stress triggers inflammasome activation and neuropathology in Alzheimer's disease. *Sci Adv* **6**, eabb8680 (2020).

15. Shi, Y. *et al.* Overexpressing low-density lipoprotein receptor reduces tau-associated neurodegeneration in relation to apoE-linked mechanisms. *Neuron* **109**, 2413-2426.e7 (2021).

16. Corder, E. H. *et al.* Gene dose of apolipoprotein E type 4 allele and the risk of Alzheimer's disease in late onset families. *Science* **261**, 921–923 (1993).

17. Saunders, A. M. *et al.* Association of apolipoprotein E allele ϵ4 with late-onset familial and sporadic alzheimer's disease. *Neurology* **43**, 1467–1472 (1993).

18. Lambert, J. C. *et al.* Meta-analysis of 74,046 individuals identifies 11 new susceptibility loci for Alzheimer's disease. *Nat Genet* **45**, 1452–1458 (2013).

19. Farrer, L. A. *et al.* Effects of age, sex, and ethnicity on the association between apolipoprotein E genotype and Alzheimer disease. A meta-analysis. APOE and Alzheimer Disease Meta Analysis Consortium. *JAMA* **278**, 1349–56 (1997).

20. Genin, E. *et al.* APOE and Alzheimer disease: A major gene with semi-dominant inheritance. *Mol. Psychiatry* **16**, 903–907 (2011).

21. Corder, E. H. *et al.* Gene dose of apolipoprotein E type 4 allele and the risk of Alzheimer's disease in late onset families. *Science* **261**, 921–923 (1993).

22. Bales, K. R. *et al.* Lack of apolipoprotein E dramatically reduces amyloid β-peptide deposition. *Nat. Genet.* vol. 17 263–264 (1997).

23. Kim, J., Basak, J. M. & Holtzman, D. M. The role of apolipoprotein E in Alzheimer's disease. *Neuron* **63**, 287–303 (2009).

24. Kanekiyo, T., Xu, H. & Bu, G. ApoE and Aβ in Alzheimer's disease: accidental encounters or partners? *Neuron* **81**, 740–54 (2014).

25. Holtzman, D. M. *et al. Apolipoprotein E isoform-dependent amyloid deposition and neuritic degeneration in a mouse model of Alzheimer's disease*. *National Institutes of Health* (2000).

26. Wang, C. *et al.* Gain of toxic apolipoprotein E4 effects in human iPSC-derived neurons is ameliorated by a small-molecule structure corrector. *Nat. Med.* **24**, 647–657 (2018).

27. Brecht, W. J. *et al.* Neuron-specific apolipoprotein E4 proteolysis is associated with increased Tau phosphorylation in brains of transgenic mice. *J Neurosci* **24**, 2527–2534 (2004).

28. Lin, Y.-T. *et al.* APOE4 causes widespread molecular and cellular alterations associated with Alzheimer's disease phenotypes in human iPSC-derived brain cell types. *Neuron* **98**, 1141-1154.e7 (2018).

29. Zhao, J. *et al.* APOE4 exacerbates synapse loss and neurodegeneration in Alzheimer's disease patient iPSC-derived cerebral organoids. *Nat Commun* **11**, 1–14 (2020).

30. Muth, C., Hartmann, A., Sepulveda-Falla, D., Glatzel, M. & Krasemann, S. Phagocytosis of apoptotic cells is specifically upregulated in apoe4 expressing microglia in vitro. *Front Cell Neurosci* **13**, 181 (2019).

31. Koutsodendris, N., Nelson, M. R., Rao, A. & Huang, Y. Apolipoprotein E and Alzheimer's disease: findings, hypotheses, and potential mechanisms. *Ann Rev Pathol* **17**, 73–99 (2022).

32. Zhu, Y. *et al.* APOE genotype alters glial activation and loss of synaptic markers in mice. *GLIA* **60**, 559–569 (2012).

33. Shi, Y. *et al.* ApoE4 markedly exacerbates tau-mediated neurodegeneration in a mouse model of tauopathy HHS Public Access. *Nature* **549**, 523–527 (2017).

34. Mishra, S. *et al.* Longitudinal brain imaging in preclinical Alzheimer disease: Impact of APOE ϵ4 genotype. *Brain* **141**, 1828–1839 (2018).

35. Andrews-Zwilling, Y. *et al.* Apolipoprotein E4 causes age-and Tau-dependent impairment of GABAergic interneurons, leading to learning and memory deficits in mice. *J Neurosci* **30**, 13707–13717 (2010).

36. Salomon-Zimri, S., Boehm-Cagan, A., Liraz, O. & Michaelson, D. M. Hippocampus-related cognitive impairments in young apoE4 targeted replacement mice. *Neurodegener. Dis.* **13**, 86–92 (2014).

37. Gale, S. C. *et al.* APOε4 is associated with enhanced in vivo innate immune responses in human subjects. *J. Allergy Clin. Immunol.* **134**, 127–134 (2014).

38. Shi, Y. *et al.* ApoE4 markedly exacerbates tau-mediated neurodegeneration in a mouse model of tauopathy. *Nature* **549**, 523–527 (2017).

39. Knoferle, J. *et al.* Apolipoprotein E4 produced in GABAergic interneurons causes learning and memory deficits in mice. *J. Neurosci.* **34**, 14069–14078 (2014).

Chapter I

Neuronal APOE4 Removal Strongly Protects Against Tau-Mediated Gliosis, Neurodegeneration, and Myelin deficits

Abstract

Apolipoprotein E4 (*APOE4*) is the strongest known genetic risk factor for late-onset Alzheimer's disease (AD). Conditions of stress or injury induce APOE expression within neurons, but the exact roles of neuronal APOE4 in AD pathogenesis are still unclear. Here we report a rigorous characterization of neuronal APOE4 effects on prominent AD-related pathologies by selectively removing APOE4 from neurons in an APOE4-expressing tauopathy mouse model. We found that removal of neuronal APOE4 led to a drastic reduction in Tau pathology accumulation and spread, gliosis, neurodegeneration, neurodysfunction, and myelin deficits in this tauopathy mouse model. Single-nucleus RNA-sequencing revealed that the removal of neuronal APOE4 eliminated neurodegenerative disease-associated subpopulations of neurons, oligodendrocytes, astrocytes, and microglia that were enriched in APOE4-expressing tauopathy mice and correlated to the severity of Tau pathology, neurodegeneration, and myelin deficits. Thus, neuronal APOE4 plays a central role in promoting the development of major AD pathologies and its removal can effectively combat APOE4-driven effects in AD and other tauopathies.

Introduction

Tauopathies are a class of neurodegenerative disorders defined by the abnormal intracellular accumulation of hyperphosphorylated Tau (pTau) protein[43–45]. Alzheimer's disease (AD) is a major type of tauopathy that is characterized by memory loss and the accumulation of amyloid plaques and Tau tangles[1,3]. Of these two major AD pathological hallmarks, Tau tangles have the strongest correlation with neurodegeneration and cognitive decline[4–7]. Other AD pathological hallmarks that have been understudied include neuroinflammation and gliosis, which have recently been shown to be key drivers of neurodegeneration[8,9]. Additionally, oligodendrocyte deficits and myelin degeneration have been observed in human AD brains[10–12] and in mouse models of AD and tauopathy[13–15]. Thus, AD is a multifactorial disorder that consists of a complex set of pathologies. However, the connections between these pathologies and the mechanisms responsible for their induction or exacerbation remain unclear.

Apolipoprotein E4 (*APOE4*) is the major genetic risk factor for AD[16–18]. While the human *APOE* gene has three common alleles, ε2, ε3, and ε4, the *APOE* ε4 allele is considered the most detrimental as it leads to an increase in AD risk and a decrease in the age of disease onset[16–19]. There have been great efforts to understand how APOE4 increases AD risk, with an extensive body of work indicating that APOE4 worsens many prominent AD-related pathologies relative to APOE3[31,46]. In particular, APOE4 has been shown to accelerate hippocampal volume loss in human patients[34] and to increase neurodegeneration in mice[35,38,47,48]. APOE4 also increases Tau burden in human brains[6,7,49,50] and promotes the accumulation of pTau in human neurons[26,28,51] and mouse models[27,38,52]. Furthermore, APOE4 increases neuroinflammation and gliosis in human AD brains[37,53,54] and in tauopathy mouse models[38]. It has also been reported that APOE4 is associated with reduced myelination and white matter integrity in human brains[55]. Together, these studies show clear evidence that APOE4 is implicated in promoting Tau pathology, gliosis, neurodegeneration, and myelin degeneration in AD and other tauopathies. Nonetheless, the

underlying mechanisms responsible for APOE4's wide-ranging effects on these various pathologies remain elusive.

Recently, there has been increasing interest in establishing the cell type-specific effects of APOE4 in AD pathogenesis. Within the central nervous system (CNS), APOE is produced by a variety of cell types and previous studies have indicated that APOE exerts different pathological effects depending on its cellular source[27,39–41]. APOE is mainly produced by astrocytes in the CNS, although conditions of stress or injury induce APOE expression in neurons[42,48,56]. Recent findings have implicated astrocytic APOE4 in the pathogenesis of AD, as genetic deletion of APOE4 in astrocytes led to a reduction of various AD-related pathologies[40]. Still, there is an incomplete understanding of the role of neuronal APOE4 in the pathogenesis of AD. Previous studies from our lab have suggested that neuronal APOE4 is important to some AD-related processes, such as Tau phosphorylation, inhibitory neuron loss, and memory deficits[27,39]. However, it is still unclear if neuronal APOE4 represents a key pathogenic factor driving the development of full-scale AD pathologies. It is critically important to elucidate the exact role of neuronal APOE4 in the pathogenesis of AD to gain a better understanding of the cellular source-specific mechanisms that drive the detrimental effects of APOE4 and to potentially reveal new therapeutic targets to combat APOE4-related AD.

In the current study, we conducted an extensive analysis of APOE4- and APOE3-expressing tauopathy mouse models to investigate the impact of selectively removing APOE4 from neurons on the development of major AD pathologies, including Tau pathology, gliosis, neurodegeneration, neurodysfunction, and myelin deficits. The outcomes of this study should provide new insights into the full-scale roles of neuronal APOE4 in the pathogenesis of AD and other tauopathies.

Materials and Methods

Mice. Human LoxP-floxed APOE knock-in (fE) mice with conditional deletion of the human *APOE* gene were generated as previously described[39]. Briefly, homozygous fE3 and fE4 mice[57] were crossbred with Synapsin 1-Cre transgenic mice [B6.Cg-Tg(Syn1-Cre)671Jxm/J] (The Jackson Laboratory #003966)[58]. The fE/Cre mice were crossbred with Tau-P301S (PS19) transgenic mice [B6;C3-Tg(Prnp-MAPT*P301S)PS19Vle/J] (The Jackson Laboratory #008169) that express human P301S 1N4R Tau driven by the PrP promoter to generate PS19-fE4 and PS19-fE3 mice with no Cre or Syn1-Cre. Littermates that were negative for Syn1-Cre were used as PS19-fE controls. For generation of the PS19-fE/Syn1-Cre line, only female Syn1-Cre mice were used for breeding purposes because germline recombination has been reported to occur in the progeny of male Syn1-Cre mice[59]. All mice were on a pure C57BL/6 genetic background and were housed in a pathogen-free barrier facility on a 12 h light cycle at 19-23ºC and 30-70% humidity. Animals were identified by ear punch under brief isoflurane anesthesia and genotyped by polymerase chain reaction (PCR) of a tail clipping. All animals otherwise received no procedures except those reported in this study. For all studies, both male and female mice were used. All animal experiments were conducted in accordance with the guidelines and regulation of the National Institutes of Health, the University of California, and the Gladstone Institutes under the protocol AN176773.

Brain tissue was collected after mice received intraperitoneal injections of avertin (Henry Schein) and were transcardially perfused with 0.9% saline for 1 min. Depending on the study, brain tissue was fixed as whole brains or hemi-brains. For hemi-brains, the right hemispheres were drop-fixed for 48 h in 4% paraformaldehyde (Electron Microscopy Sciences), washed for 24 h in 1X PBS (Corning), and cryoprotected in 30% sucrose (Sigma) for 48 h at 4ºC. The fixed right hemispheres were cut into 30 µm thick coronal sections on a freeze sliding microtome (Leica) and stored in

cryoprotectant solution at -20ºC (30% Ethylene Glycol, 30% Glycerol, 40% 1X PBS). Left hemispheres were snap frozen on dry ice and stored at -80ºC.

Immunohistochemistry. Several brain sections (~300 µm apart) were washed with 1X PBS-T (PBS + 0.1% Tween-20) (Millipore Sigma) and incubated for 5 min in boiling antigen retrieval buffer (Tris buffer, pH 7.6) (TEKNOVA). Sections were then washed in PBS-T before being incubated in blocking solution (5% normal donkey serum (Jackson Labs), 0.2% Triton-X (Millipore Sigma) in 1X PBS for 1 h at room temperature. Then, sections were washed in PBS-T and incubated in Mouse-on-Mouse (M.O.M.) Blocking Buffer (1 drop M.O.M IgG/4mL PBS-T) (Vector Labs) for 1 h at room temperature. After M.O.M. block, sections were incubated in primary antibody at 4ºC overnight after being diluted to optimal concentrations (anti-APOE 1:200 (Cell Signaling); anti-Calmodulin 1:100 (Thermofisher); anti-CD68 1:100 (Bio-Rad); anti-Cre recombinase 1:800 (Cell Signaling); anti-Cleaved Caspase-3 1:100 (Cell Signaling); anti-GFAP (ms) 1:800 (Millipore Sigma); anti-GFAP (gt) 1:800 (Novus Biological); anti-GFP 1:5000 (Thermofisher); anti-HSP90 1:100 (Abcam); anti-Iba1 (rbt) 1:300 (Wako); anti-Iba1 (gt) 1:100 (Abcaam); anti-MBP 1:500 (Abcam); anti-Mertk 1:100 (Thermofisher); anti-NeuN 1:500 (Millipore Sigma); anti-NG2 1:500 (Abcam); anti-Olig2 (ms) 1:100 (Millipore Sigma); anti-Olig2 (gt) 1:100 (R&D Systems); anti-S100β 1:200 (Abcam); anti-Tmsb4x 1:100 (Thermofisher); anti-Ubiquitin 1:100 (Thermofisher)). After primary antibody incubation, sections were washed in PBS-T and incubated in for 1 h in secondary antibodies (Abcam, Jackson Immuno, 1:1000 in PBS-T) at room temperature. Sections were washed in PBS-T and incubated in DAPI (1:30,000 in PBS-T) (Thermofisher) for 8 min at room temperature. After washing with PBS-T, sections were mounted onto microscope slides (Fisher Scientific), coverslipped with ProLong Gold mounting media (Vector Laboratories), and sealed with clear nail polish. Images were taken using an FV3000 confocal laser scanning microscope (Olympus) or Aperio VERSA slide scanning microscope

(Leica) at 10X, 20X, 40X, or 60X magnifications depending on the stain. For each staining, all samples were stained at the same time to limit batch-to-batch variation and imaged at the same fluorescent intensity. For the % coverage area quantification, an optimal threshold was established for each stain in ImageJ and all samples were quantified utilizing the established threshold for each stain. To exclude the possibility of bias, researchers were blinded to samples.

For DAB (3, 3'-diaminobenzidine) staining, several brain sections (~300 µm apart) were washed in PBS-T and incubated for 5 min in boiling antigen retrieval buffer (1X PBS, 0.1M sodium citrate, 0.1M citric acid) (Fisher Scientific, Fluka). Next, sections were washed in PBS-T and incubated for 15 min in endogenous peroxidase buffer (1X PBS, 10% methanol (Fisher Scientific) , 3% H_2O_2 (Sigma) and washed in PBS-T before being incubated in blocking solution (1X PBS-T, 5% normal donkey serum, 1% non-fat dry milk) for 1 h at room temperature. After blocking, sections were washed in PBS-T and incubated in Avidin/Biotin blockage (4 drops of each block) (Vector Laboratories) for 15 min and then washed in PBS-T. Sections were incubated in M.O.M. Blocking Buffer (1 drop M.O.M IgG/4mL PBS-T) (Vector Labs) for 1 h at room temperature. Following M.O.M. block, sections were washed in PBS-T and incubated in primary antibody at 4ºC overnight (anti-pTau (AT8) 1:100 (Invitrogen); anti-HT7 1:200 (Peter Davies)). After primary antibody incubation, sections were washed in PBS-T and incubated in biotinylated secondary antibody (1:200; Jackson Immuno) at room temperature for 1 h. Next, sections were washed in PBS-T and incubated in ABC buffer (Vector Laboratories) that was prepared 10 min prior to the incubation step. Sections were washed for in PBS-T and then Tris buffer (pH 7.6). Sections were incubated in DAB buffer (5mL 1X PBS, 2 drops Buffer Stock Solution, 2 drops DAB, 2 drops H_2O_2) (Vector Laboratories) for precisely 2 minutes. Staining was halted by washing sections in Tris buffer (pH 7.6) and then in PBS-T. Sections were mounted onto microscope slides and dried at room temperature overnight. Next, mounted sections were submerged into Xylene (Fisher Scientific)

and coverslipped with DPX mounting media (Sigma-Aldrich). Images were taken using an Aperio VERSA slide scanning microscope (Leica) at 10X magnification.

For thioflavine S (Thio-S) staining, several brain sections (300 µm apart) were mounted onto slides and the protocol was adapted from a previous study[60]. The tissue was washed with 1X PBS-T and then incubated in a solution of 0.06% Thio-S in PBS for 8 minutes. Then, sections were washed for 1 minute in 80% ethanol and 5 minutes in PBS-T. Sections were then counterstained with DAPI for 8 minutes, washed with PBS-T and coverslipped. Thio-S staining was imaged in the 488-fluorescent channel on an Aperio VERSA slide scanning microscope (Leica) at 10X magnification.

Volumetric analysis. Hippocampal brain sections (7 sections per mouse, 30 µm thick, 300 µm apart) were mounted onto microscope slides (Fisher Scientific). A 0.1% Sudan Black solution was prepared by adding Sudan Black powder (Sigma) to 70% ethanol (KOPTEC) and mixing the solution using a magnetic stirrer. The solution was then centrifuged at 3,000 RPM for 10 min and the collected supernatant was filtered using a 0.2 µm filter syringe (Thermo Scientific). Sections were then stained with the 0.1% Sudan Black solution for 10 min and washed in 70% ethanol and then in Milli-Q water. Sections were coverslipped with ProLong Gold mounting media (Invitrogen) and imaged on an Aperio VERSA slide scanning microscope (Leica) at 10X magnification. To quantify the volumes of the hippocampus and posterior lateral ventricle, we traced the areas of interest in ImageJ and used the formula: volume = (sum of area) * 0.3 mm^3[38]. We took a sum of all 7 brain sections per mouse, roughly between coordinates AP=-1.2 and AP=-3.4.

Neuronal layer thickness measurements. Two brain sections (30 µm thick, 300µm apart) underwent immunofluorescence staining as described above using the primary antibody NeuN (1:500) to visualize the neuronal cell layers of the hippocampus. Sections were imaged at 20X

magnification using an FV3000 confocal laser scanning microscope (Olympus). The thickness of the CA1 pyramidal cell layer and dentate gyrus granular cell layer of the hippocampus were measured on the Fiji (ImageJ) software by drawing a straight line perpendicular to the NeuN+ cell layers at two points per hippocampal subfield and taking the average value for each mouse.

Biochemical extraction of brain tissue. The hippocampus was dissected from snap frozen mouse hemi-brains after thawing on ice. The hippocampal tissue was weighed and homogenized using a Polytron immersion disperser homogenizer (Kinematica AG) in ice-cold RAB buffer (G Biosciences) at 10 µL/mg tissue, supplemented by phosphatase inhibitors (Roche) and protease inhibitors (Roche). Samples were then centrifuged using an Optima TLX ultracentrifuge (Beckman Coulter) at 50,000g for 20 min at 4ºC and the supernatant was collected as the RAB-soluble fraction. The pellets were resuspended in ice-cold RIPA buffer (Thermo Scientific) at 10 µL/mg tissue and centrifuged at 50,000g for 20 min at 4ºC. The supernatant was collected as the RIPA-soluble fraction and the pellet was stored at -80ºC for further use. All fractions were stored at -80ºC until further analyses.

Western blot analysis. Biochemically extracted mouse hippocampal tissue lysates were loaded onto 12% Bis-Tris SDS-PAGE gels (Invitrogen) and separated by gel electrophoresis at 160V using MOPS buffer. The separated proteins were transferred onto nitrocellulose membranes at 18V for 60 min (Trans-Blot Turbo Transfer System (Bio-rad). Membranes were washed 3x5min in PBS-T and then incubated in Intercept blocking buffer (LI-COR) for 1 h at room temperature to block non-specific binding sites. After blocking, membranes were washed 3x5min in PBS-T and incubated with primary antibody overnight at 4ºC (AT8 1:3,000 (Invitrogen), TUJ1 1:10,000 (Biolegend)). Membranes were washed 3x5min in PBS-T and incubated in fluorescently-labeled secondary antibody (1:20,000; LI-COR) for 1 h in the dark at room temperature. Resulting bands were detected with the Odyssey CLx infrared imaging system (LI-COR), and the fluorescence

intensity of the bands was quantified as a ratio of AT8:TUJ1 signal using the Image Studio software.

Sandwich ELISA. Hippocampal tissue lysates were diluted in H_2O to the appropriate concentration and were run according to the provided manufacturer protocols (human APOE (Abcam); human total Tau (Thermofisher)). Sample reactions were read on a SpectraMaX M5 spectrophotometer (Molecular Devices) and protein concentrations were determined after interpolating a standard curve and adjusting for dilutions.

Stereotaxic surgery on mice. After being anesthetized with an intraperitoneal injection of ketamine (60 mg/kg) and xylazine (30 mg/kg) and maintained on 0.8%-1.0% isofluorane (Henry Schein), mice were secured in a stereotaxic alignment system model 940 using earbars and a tooth bar (Kopf Instruments). We removed hair using Nair and cut the scalp open using a scalpel and sterilized with 70% ethanol. Cranial sutures were visualized using 3% hydrogen peroxide. Following identification of Bregma, a unilateral stereotaxic site was drilled with a 0.5 mm microburr (Fine Science Tools) using coordinates X = +1.5, Y = -2.1, Z = -2.1). Mice were injected with 2µL of the respective virus (AAV2(Y444F)-smCBA-human_P301S_Tau-WPRE, 2.10E+13 vg/mL, Virovek); AAV2-Synapsin-GFP, 1.0E+13 vg/mL, SignaGen) at a rate of 500 nL/min and allowed to diffuse for 3 min. Following surgery, mice were sutured with nylon monofilament non-absorbable 6-0 sutures (Henry Schein), and administered analgesics buprenorphine (0.0375 mg/kg intraperitoneally), ketophen (5 mg/kg subcutaneously), and saline (500µL intraperitoneally). Mice were monitored on a heating pad until ambulatory and provided Hydrogel for hydration.

Brain slices electrophysiological recordings and data analyses. For electrophysiological recording study, 8-month-old PS19-fE3 mice and PS19-fE4 mice with no Cre and Syn1-Cre were

anaesthetized with isoflurane and decapitated. The brain was rapidly removed and placed in ice-cold (2–5°C) slicing solution (in mM): 110 choline chloride, 2.5 KCl, 26 $NaHCO_3$, 10 $MgCl_2$, 1.25 NaH_2PO_4, 0.5 $CaCl_2$, 10 glucose, 3 Na Pyruvate, 1 L-Ascorbic acid, pH 7.4. 350 µm-thick sagittal slices were cut from both hemispheres using a vibratome (VT1200, Leica) and transferred to a 95% O_2-CO_2 vapor interface holding chamber (BSK5, Scientific Systems Design) containing artificial cerebrospinal fluid (ACSF) where they were allowed to recover at 34°C for one hour and held at room temperature (20–22°C) afterwards. ACSF contained (in mM): 126 NaCl, 2.5 KCl, 1.5 $CaCl_2$, 1.5 $MgCl_2$, 26 $NaHCO_3$, 1.25 NaH_2PO_4, 10 glucose, and 1.5 L-Ascorbic acid, pH 7.4.

For input/output recording studies, local field post-synaptic potentials (fPSPs) were elicited by orthodromic stimulation of Schaffer collaterals by concentric bipolar stimulating electrode (FHC) connected to a constant voltage isolated stimulator (DS2A-MKII, Digitimer North America) and placed in CA2 stratum radiatum. fPSPs were recorded with a glass borosilicate microelectrode filled with ACSF and placed in CA1 stratum radiatum. Signals were sampled and digitized by MultiClamp 700B amplifier and Digidata 1550B1 acquisition system with pClamp10 software (Molecular Devices), and analyzed using IgorPro6 software (Wavemetrics) running custom macros. fPSP slopes were analyzed as the linear fit slope values between 10% and 90% of fPSP peak. Input-output relationships were recorded as the fPSP slope values in response to increasing stimulation intensity (20-60µA), with fPSP slope gain calculated as the linear slope of the resulting input-output curve.

Single-nuclei preparation for 10x loading. The mouse hippocampus was dissected on ice and placed into a pre-chilled 2 mL Dounce with 1 mL of cold 1X Homogenization Buffer (1X HB) (250 mM Sucrose, 25 mM KCL, 5 mM $MgCl_2$, 20 mM Tricine-KOH pH7.8, 1 mM DTT, 0.5 mM Sermidine, 0.15 mM Sermine, 0.3% NP40, 0.2 units/µL RNase inhibitor, 0.2 units/µL Protease inhibitor). Dounce with “A” loose pestle (~10 strokes) and then with “B” tight pestle (~15 strokes).

The homogenate was filtered using a 70 µM Flowmi strainer (Eppendorf) and transferred to a pre-chilled 2 mL LoBind tube (Fischer Scientific). Nuclei were pelleted by spinning for 5 min at 4°C at 350 RCF. The supernatant was removed and the nuclei were resuspended in 400 µL 1X HB. Next, 400 µL of 50% Iodixanol solution was added to the nuclei and then slowly layered with 600 µL of 30% Iodixanol solution under the 25% mixture, then layered with 600 µL of 40% Iodixanol solution under the 30% mixture. The nuclei were then spun for 20 min at 4°C at 3,000g in a pre-chilled swinging bucket centrifuge. 200 µL of the nuclei band at the 30%-40% interface was collected and transferred to a fresh tube. Then, 800 µL of 2.5% BSA in PBS plus 0.2 units/µL of RNase inhibitor was added to the nuclei and then were spun for 10 min at 500 RCF at 4C. The nuclei were resuspended with 2% BSA in PBS plus 0.2 units/µL RNase inhibitor to reach ~500 nuclei/µL. The nuclei were then filtered with a 40 µM Flowmi stainer. The nuclei were counted and then ~13,000 nuclei per sample were loaded onto 10x Genomics Next GEM chip G. The snRNA-seq libraries were prepared using the Chromium Next GEM Single Cell 3' Library and Gel Bead kit v3.1 (10x Genomics) according to the manufacturer's instructions. Libraries were sequenced on an Illumina NovaSeq 6000 sequencer at the UCSF CAT Core.

Custom reference genome. PS19 tau mutant floxed APOE knock-in mouse model[57] was used for single-nucleus RNA-sequencing (snRNA-seq). The Homo sapiens microtubule associated protein tau (MAPT) (NCBI Reference Sequence: NM_001123066.4)[61] and the Homo sapiens APOE are genes of interest for this study. These genes are not expected to be a part of the mouse reference genome, so to quantify the reads aligning to these genes of interest, a custom mouse reference genome was made using the reference mouse genome sequence (GRCm38) from Ensembl (release 98)[62] and the mouse gene annotation file from GENCODE (release M23)[63], similar to those used in 10x Genomics Cell Ranger mouse reference package mm10 2020-A. The headers of the Ensembl reference mouse genome sequence fasta file with the chromosome names were modified to match the chromosome names in a fasta file from GENCODE. The

annotation GTF file contains entries from non-polyA transcripts that overlap with the protein coding genes. These reads are flagged as multi-mapped and are not counted by the 10x Genomics Cell Ranger v6.1.1 count pipeline[64]. To avoid this, the GTF file was modified to (1) remove version suffixes from transcript, gene, and exon ids to match the Cell Ranger reference packages, (2) remove non-polyA transcripts. The Homo sapiens MAPT sequence and Homo sapiens APOE sequence were appended as separate chromosomes to the end of the mouse reference genome sequence and the corresponding gene annotations were appended to the filtered mouse reference gene annotation GTF file. The 10x Genomics Cell Ranger v6.1.1 mkref pipeline was used to build the custom reference genome using the modified fasta and GTF file.

Pre-processing and clustering of mouse snRNA-seq samples. The snRNA-seq samples included a total of 12 samples with four mice from each of the three genotype groups (PS19-fE4, PS19-fE4/Syn1-Cre, and PS19-fE3). Each group of four mice had two male and two female mice. The demultiplexed fastq files for these samples were aligned to the custom mouse reference genome (See custom reference genome methods for additional descriptions) using the 10x Genomics Cell Ranger v6.1.1 count pipeline[64], as described in the Cell Ranger documentation. The include-introns flag for the count pipeline was set to true to count the reads mapping to intronic regions. The Cell Ranger count web summaries showed a “Low Fraction Reads in Cells” error for one sample from the PS19-fE3 group, which had only ~40% reads assigned to cell-associated barcodes and <80% reads mapped to the genome. These metrics were much higher for the other 11 samples. Checking the experimental record indicated that this sample had issues at the nuclear isolation step and lower cDNA was recovered due to the use of an expired old batch of sample preparation reagents. All other samples were prepared with a new batch of sample preparation reagents. So, this one sample was excluded and only the remaining 11 samples were used for the downstream analyses with Seurat.

The filtered count matrices generated by the Cell Ranger count pipeline for 11 samples were processed using the R package for single-nucleus analysis Seurat v4.0.5[65]. Each sample was pre-processed as a Seurat object and the top 1% of cells per sample with a high number of unique genes, cells with <=200 unique genes, and cells >=0.25% mitochondrial genes were filtered out for each sample. The 11 samples were merged into a single Seurat object and normalization and variance stabilization was performed using sctransform[66] with the "glmGamPoi" (Bioconductor package version 1.6.0) method[67] for initial parameter estimation.

Graph-based clustering was performed using the Seurat v4.0.5 functions FindNeighbors and FindClusters. First, the cells were embedded in a k-nearest neighbor (KNN) graph based on the Euclidean distance in the PCA space. The edge weights between two cells were further modified using Jaccard similarity. Next, clustering was performed using the Louvain algorithm implementation in the FindClusters Seurat function. Clustering was performed for all combinations of 10,15 and 20 PCs with 0.4, 0.5, 0.6, 0.7,0.8 and 0.9 resolutions. Clustering with 15 PCs and 0.7 resolution resulted in 34 distinct biologically relevant clusters, which was used for further analyses.

Cell type assignment. Data visualization using Seurat v4.0.5 in the UMAP space for the 11 samples revealed no batch effects by age, sex, genotype, date of birth, or nuclear isolation date. The marker genes for each cluster were identified using the FindAllMarkers Seurat function on the SCT assay data. This algorithm uses the Wilcoxon Rank Sum test to iteratively identify differentially expressed genes in a cluster against all the other clusters. Marker genes were filtered to keep only positively expressed genes, detected in at least 25% of the cells in either population and with at least 0.5 log2 fold change. We assigned identities to cell clusters by matching the cell clusters to known cell types with the expression of canonical cell-type-specific genes, the expression of genes identified in publicly available mouse hippocampal single-cell RNA-seq

datasets, and the expression of each cluster's marker genes in a publicly available resource of brain-wide in situ hybridization images, as we reported previously[48].

Subclustering of astrocytic and microglial sn-RNA-seq data. The hippocampal cell cluster 12 was annotated as the astrocyte cells and hippocampal cell clusters 14, 25 and 29 were annotated as the microglial cells. Both these cell types were further sub-clustered. Normalization and variance stabilization was performed using sctransform[66] with the "glmGamPoi" (Bioconductor package version 1.6.0) method[67] for initial parameter estimation. Graph-based clustering was performed using the Seurat v4.0.5 functions FindNeighbors and FindClusters. First, the cells were embedded in a k-nearest neighbor (KNN) graph based on the Euclidean distance in the PCA space. The edge weights between two cells were further modified using Jaccard similarity. Next, clustering was performed using the Louvain algorithm implementation in the FindClusters Seurat function. Clustering was performed for all combinations of 10,15, 20, 25 and 30 PCs with 0.4, 0.5, 0.6, 0.7,0.8 and 0.9 resolutions. Sub-clustering with 15 PCs and 0.9 resolution resulted in 15 distinct biologically relevant subclusters for astrocytes. Sub-clustering with 15 PCs and 0.9 resolution resulted in 15 distinct biologically relevant microglia subclusters.

Gene-set enrichment analysis. Differentially expressed genes between clusters of interest were identified using FindMarkers Seurat function on the SCT assay data. This algorithm uses the Wilcoxon Rank Sum test to identify differentially expressed genes between two populations. Differentially expressed genes were limited to genes detected in at least 10% of the cells in either population and with at least 0.1 log2 fold change. Over-representation (or enrichment) analysis was performed using clusterProfiler v4.2.1[68] to find gene sets in the KEGG database[69] for mouse associated with the differentially expressed genes. The p-values are based on a hypergeometric test and are adjusted for multiple testing using the Benjamini-Hochberg method[70]. Significantly enriched gene sets were filtered to have an adjusted p-value less than 0.8 and at least 10

differentially expressed genes present in the gene set. The same method was used for gene-set enrichment analysis of astrocyte subclusters and microglia subclusters.

Association between clusters and genotype. A Generalized Linear Mixed-Effects Model to assess association with Animal Models (GLMM_AM) was implemented in the lme4 (v1.1-27.1) R package[71] and used to estimate the associations between cluster membership and the mouse model. These models were run separately for each cluster of cells. The GLM model was performed with the family argument set to the binomial probability distribution and with the *bobyqa* control optimizer used for the maximum likelihood estimation. Cluster membership for each cell was modeled as a 0-1 response variable according to whether or not the cell belongs to the cluster under consideration. The corresponding mouse id from which the cell was derived was the random effect variable and the animal model for this mouse id was included as the fixed variable. The reference animal model was set to PS19 fE4. The resulting p-values for the estimated log odds ratio across the two animal models (with respect to the PS19 fE4) and clusters were adjusted for multiple testing using the Benjamini-Hochberg method[70]. The same method was used for estimating the between cluster association with genotype for astrocyte subclusters and microglia subclusters.

Association between proportion of cell types and histopathological parameters. A Generalized Linear Mixed-Effects Model to assess association with histopathology (GLMM_histopathology) was implemented in the lme4 (v1.1-27.1) R package[71] and used to identify cell types whose proportions are significantly associated with changes in histopathology across the samples. These models were performed separately for each combination of the cluster of cells and the four histological parameters: hippocampal volume (mm^3), the percent of AT8 coverage area, the percent of MBP coverage area, and the percent of OPC coverage area. The GLM model was performed with the family argument set to the binomial probability distribution

family and with the '*bobyqa*' control optimizer used for the maximum likelihood estimation. Cluster membership for each cell was modeled as a 0-1 response variable according to whether or not the cell belongs to the cluster under consideration. The corresponding mouse model from which the cell was derived was included as a random effect and further the mouse id within the given mouse model was modeled as a random effect as well. Note, this represents the hierarchical nature of this data for the GLMM, and the mouse models are first assumed to be sampled from an "universe" of mouse models, this is then followed by sampling mice within each mouse model. The modeling choice of including the mouse model as a random effect as opposed to a fixed effect is meant to increase the degrees of freedom (or maximize the statistical power) to detect the association of interest, particularly in light of the relatively small number of replicates (3-4) per animal model. The histological parameter under consideration was modeled as a fixed effect in this model.

We selected a subset of cell types of interest and visualized the logOdds ratio estimates (derived from the GLMM fits) in a heatmap using *pheatmap* package 1.0.12 after adjusting the p-values distribution across histopathological parameters across cell types with *Benjamini-Hochberg* multiple testing correction[70]. We applied the pipeline to the astrocyte and microglia subtypes and visualized the associations between astrocyte and microglia subtypes of interest and the four histopathological parameters in Fig. 7 and 8 respectively. We estimated the first 5 principal component coordinates using the four logOdds ratio for unit change of the histopathological parameters for each of the cell types and astrocyte and microglia sub-cell types of interest. This was implemented using *prcomp(scale=T, center=T)* in *stats* R package. We visualized the first two PCs using fviz_pca_ind() implemented in factoextra 1.0.7 R package.

Immunohistochemical validation of neuronal APOE4-promoted disease-associated (nE4-DA) subpopulations of cells. Two hemibrain sections (30 μm thick, 300μm apart) with

hippocampus from each mouse underwent immunofluorescence staining as described above using antibodies against the appropriate cell type-specific marker and two distinct nE4-DA marker genes (nE4-DANs: NeuN (1:500), HSP90 1:100; Ubb 1:100; nE4-DAOs: Olig2 (1:100), HSP90 (1:100), Ubb (1:100); nE4-DAAs: GFAP (1:800), Mertk (1:100), Calm (1:100); nE4-DAM: (Iba1 (1:100), Ubb (1:100), Tmsb4x (1:100)). Sections were imaged at 10X magnification on an Aperio VERSA slide scanning microscope (Leica) or 40X magnification using an FV3000 confocal laser scanning microscope (Olympus). Utilizing the Fiji (ImageJ) software, we first generated a mask of the channel containing the cell type-specific marker. Then, the image calculator function was used to generate a new image that contains only cells that are positive for both distinct nE4-DA marker genes by selecting the images for both marker genes and using the operation 'AND'. We then took the masked cell type-specific marker image and the combined nE4-DA marker gene image and utilized the image calculator function with the operation 'AND' to generate a new image that combines all 3 stains. Ultimately, this quantification method provided a measure of cells that were double-positive for both nE4-DA distinct marker genes and were also positive for the appropriate cell type-specific marker.

General statistical analysis. The differences between genotype groups were evaluated by ordinary one-way ANOVA with Tukey's multiple comparisons test, where the mean of each column was compared with the mean of every other column. All plotted data are presented as the mean ± SEM. The correlations between two data in the same genotype group were analyzed using simple linear regression and plotted as the mean ± SEM. The analyses were performed and plots were created with GraphPad Prism version 9.2.0.

Data availability. The snRNA-seq datasets generated during the study will be made available at GEO (accession # xxxxxxxx) upon acceptance of the paper. Data associated with Fig. 5, 7, and 8 are also available in the Supplementary Information.

Results

Neuron-specific removal of the *APOE* gene in human APOE-KI mice expressing human mutant Tau

Our laboratory previously generated mouse lines expressing a floxed human *APOE3* or *APOE4* gene[57] and a Cre recombinase gene under the control of a neuron-specific Synapsin-1 promoter (Syn1-Cre)[58]. These floxed *APOE-KI* (fE) mice express homozygous human *APOE3* or *APOE4* in place of the endogenous mouse *Apoe,* and the human *APOE* gene is flanked by a pair of LoxP sites to allow for its precise excision in the presence of cell-type-specific Cre recombinase expression[39]. The fE mice with or without Syn1-Cre were crossbred with mice expressing mutant 1N4R human microtubule-associated protein Tau (*MAPT*) encoding the disease-associated P301S mutation (PS19 line), which has been widely utilized as a tauopathy mouse model[72]. The resulting compound mice are referred to as PS19-fE or PS19-fE/Syn1-Cre mice.

We previously performed a rigorous characterization of fE/Syn1-Cre mice to validate the specificity of Cre recombinase expression under the neuron-specific Syn1 promoter[39]. To further confirm its specificity in 10-month-old PS19-fE mice, we utilized immunohistochemistry to evaluate Cre recombinase expression in multiple relevant cell types known to express APOE, including neurons (NeuN), astrocytes (GFAP), microglia (Iba1), oligodendrocytes (Olig2), and oligodendrocyte progenitor cells (OPCs) (NG2). In PS19-fE4/Syn1-Cre mice, Cre recombinase was expressed exclusively in NeuN-positive neurons and was not expressed in any of the other four cell types (**Fig. 1.1a-d**). Immunostaining for APOE in these relevant cell types showed that both PS19-fE4 and PS19-fE4/Syn1-Cre mice have APOE expression in astrocytes, microglia, oligodendrocytes, and OPCs. (**Fig. 1.1e-h**).

We quantitively analyzed hippocampal lysates of 10-month-old mice by sandwich ELISA. PS19-fE4/Syn1-Cre mice exhibited a ~20% decrease in APOE levels relative to PS19-fE4 mice (**Fig. 1.1i**), which aligns with previous reports from our lab indicating that neuronal APOE contributes to ~20–30% of total APOE protein levels in the hippocampus and cortex[39,48]. Similarly, PS19-fE3/Syn1-Cre mice exhibited a ~25% decrease in APOE levels relative to PS19-fE3 mice (**Fig. 1.1i**). These results provide strong evidence that *APOE* gene expression is selectively eliminated in neurons when Cre recombinase expression is driven under a Syn1 promoter while leaving APOE expression in other relevant APOE-expressing cell types in the brain, which is confirmed by single nucleus RNA-sequencing (snRNA-seq) analysis (see below).

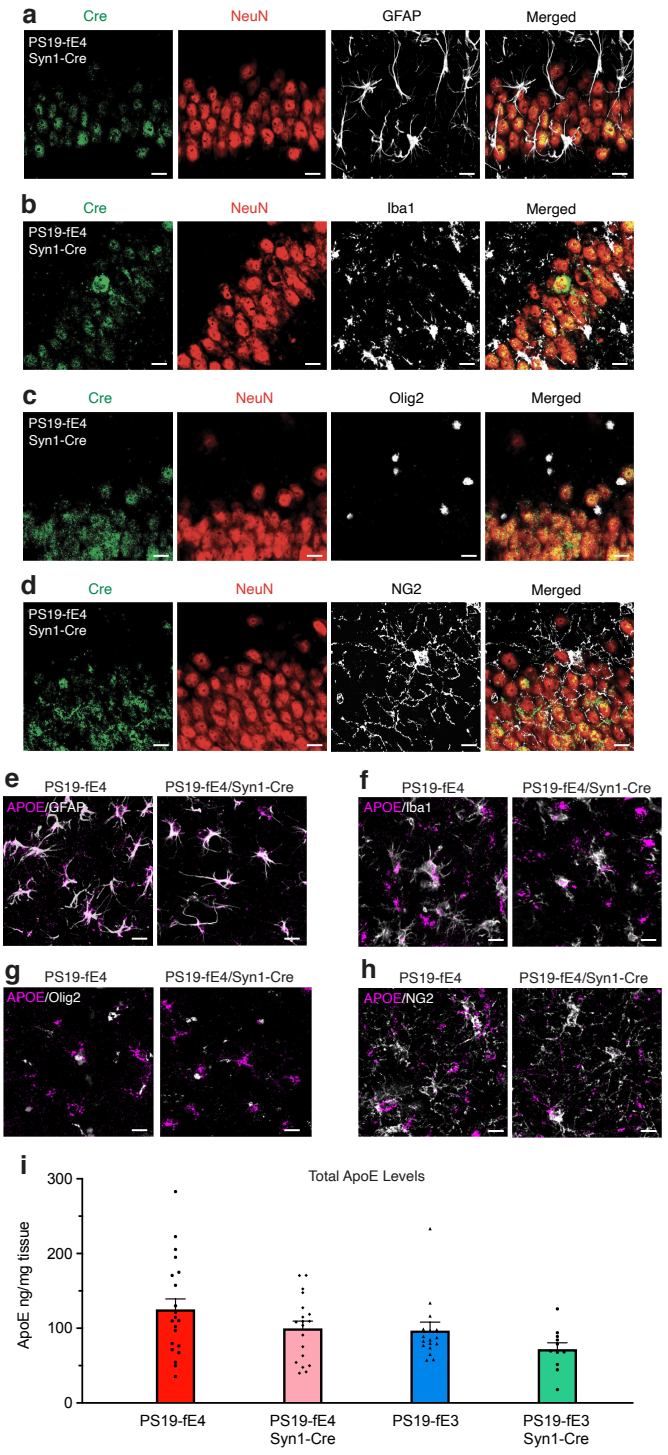

Figure 1.1 Characterization of PS19-fE mouse models with the *APOE* gene specifically removed from neurons by neuron-specific Syn1-Cre expression. a–d, Representative images of the cell type-specificity of Cre recombinase expression in various cell types as determined by immunostaining for Cre recombinase in neurons (NeuN) (a–d), astrocytes (GFAP) (a), microglia (Iba1) (b), oligodendrocytes (Olig2) (c), and OPCs (NG2) (d) in the hippocampus of 10-month-old PS19-fE4 mice with Syn1-Cre (scale bar, 20 μm). **e–h**, Representative images of the cell type-specificity of APOE expression in various cell types by immunostaining for APOE in

astrocytes (e), microglia (f), oligodendrocytes (g), and OPCs (h) in the hippocampus of 10-month-old PS19-fE4 mice with and without Cre (scale bar, 20 μm). **i**, APOE levels measured by ELISA in the hippocampal lysates of 10-month-old PS19-fE4 and PS19-fE3 mice with and without Cre (PS19-fE4: No Cre, n=21; Syn1-Cre, n=18; PS19-fE3: No Cre, n=17; Syn1-Cre, n=11). APOE levels are normalized to the weight of the dissected hippocampal tissue for each individual mouse. Data are represented as mean ± SEM, one-way ANOVA with Tukey's post hoc multiple comparisons test.

Removal of APOE4 from neurons drastically reduces Tau pathology

To determine whether the removal of neuronal APOE affects Tau pathology, we assessed mice at 10 months of age, which is when PS19 mice exhibit extensive Tau pathology throughout the hippocampus[72]. We immunostained with the pTau-specific AT8 antibody and quantified Tau pathology as the percent of AT8 coverage area in the hippocampus. PS19-fE4 mice presented extensive Tau pathology throughout the hippocampus and the extent of Tau pathology was significantly lower in PS19-fE3 mice (**Fig. 1.2a,b**). The PS19-fE4/Syn1-Cre mice exhibited a striking reduction (~81%) in Tau pathology relative to PS19-fE4 mice (**Fig. 1.2a,b**). There was no significant difference in Tau pathology between PS19-fE3 with and without Cre, likely because the Tau pathology in PS19-fE3 mice was already low. Assessment of neurofibrillary tangles by staining with Thioflavine S (Thio-S) revealed a similar pattern, with PS19-fE4 mice exhibiting a much higher number of Thio-S-positive cells in the hippocampus than PS19-fE3 mice and removal of neuronal APOE4 leading to a significant decrease in the number of neurofibrillary tangle-bearing cells (**Fig. 1.2c,d**).

We also utilized western blot to assess levels of $AT8^+$ pTau in mouse hippocampal tissues following sequential biochemical extraction with RAB and RIPA buffers, containing highly soluble and less soluble Tau proteins, respectively[38,73]. There was no significant difference in pTau levels between the various genotype groups in the RAB fraction, although removal of neuronal APOE4 led to a minor decrease (**Fig. 1.2e,g**). However, PS19-fE4/Syn1-Cre and PS19-fE3 mice exhibited a significant reduction in pTau levels in the RIPA fraction relative to PS19-fE4 mice (**Fig. 1.2f,h**). Taken together, these data indicate that neuronal APOE4 is a strong driver of Tau pathology.

Propagation of Tau pathology is reduced after removal of APOE4 in neurons

To investigate the mechanisms by which neuronal APOE4 drives Tau pathology, we determined the effects of neuronal APOE4 expression on the propagation of Tau. In AD and other tauopathies, pathological Tau has been shown to spread between neurons and across interconnected brain regions[60,74]. Previous studies have examined Tau propagation *in vivo* by injecting pathological Tau protein directly into mouse brains and showing that Tau can spread from its injection site to anatomically connected brain regions[75–79]. To study Tau propagation, we injected an adeno-associated virus-2 encoding human P301S mutant Tau (AAV2-Tau-P301S) into the right dorsal hippocampus of fE mice with or without Syn1-Cre and analyzed the extent of Tau propagation from the right (injected) hippocampus to the left (non-injected) hippocampus (**Fig. 1.2i,j**). The mice were injected with the AAV2-Tau-P301S virus at 10 months of age and assessed 12 weeks post-injection at 13 months of age (**Fig. 1.2i**). Notably, the fE mice utilized for this experiment lack human P301S mutant Tau and instead express the endogenous mouse *Mapt* gene, allowing for a more accurate detection of human Tau-P301S spread from the injection site since fE mice exhibit minimal Tau pathology.

To provide evidence that the observed Tau propagation phenotype can truly be attributed to the spread of pathological human Tau between neurons as opposed to an unexpected consequence of the Tau-encoding virus itself traveling to the non-injected hippocampal side, we tested the unilateral injection of an AAV2 of the same serotype that encodes GFP (AAV2-GFP) into the right dorsal hippocampus of a 10-month-old fE4 mouse. Immunostaining with anti-GFP two weeks post-injection revealed that the GFP signal remains localized to neurons within the injected hippocampal side (**Fig. 1.2k**). The non-injected hippocampal side did not have any evident GFP signal in neuronal somas, although there were some GFP-positive neuronal projections, likely stemming from neurons residing on the injected hippocampal side. This illustrates that the AAV2

itself does not spread between the right and left hippocampus following unilateral injection. Furthermore, to quantify the extent of tau spread using immunohistochemical analyses, we quantified the number of soma-positive-Tau-containing neurons in the non-injected side to more accurately reflect human mutant Tau spread between neurons and exclude confounding factors, such as Tau-positive commissural fibers from neurons originating from the injected side.

Immunostaining for HT7 revealed robust human Tau propagation to the non-injected hippocampal side in fE4 mice and minimal Tau propagation in fE3 mice (**Fig. 1.2l,m**), indicating that APOE4 promotes Tau spreading. Intriguingly, fE4/Syn1-Cre mice had a significant reduction in human Tau propagation to the non-injected hippocampal side relative to fE4 mice, with a 55% decrease in the number of $HT7^{+}$ cells with Tau propagation after removal of neuronal APOE4 (**Fig. 1.2l,m**).

We further analyzed the extent of Tau propagation by immunostaining for pTau with the AT8 antibody. The fE4 mice exhibited robust propagation of pTau to the non-injected hippocampal side, while fE4/Syn1-Cre and fE3 mice had drastically reduced pTau propagation (**Fig. 1.2n,o**). Taken together, these data indicate that one mechanism by which neuronal APOE4 drives Tau pathology is by stimulating the propagation of Tau and/or pTau between anatomically connected brain regions.

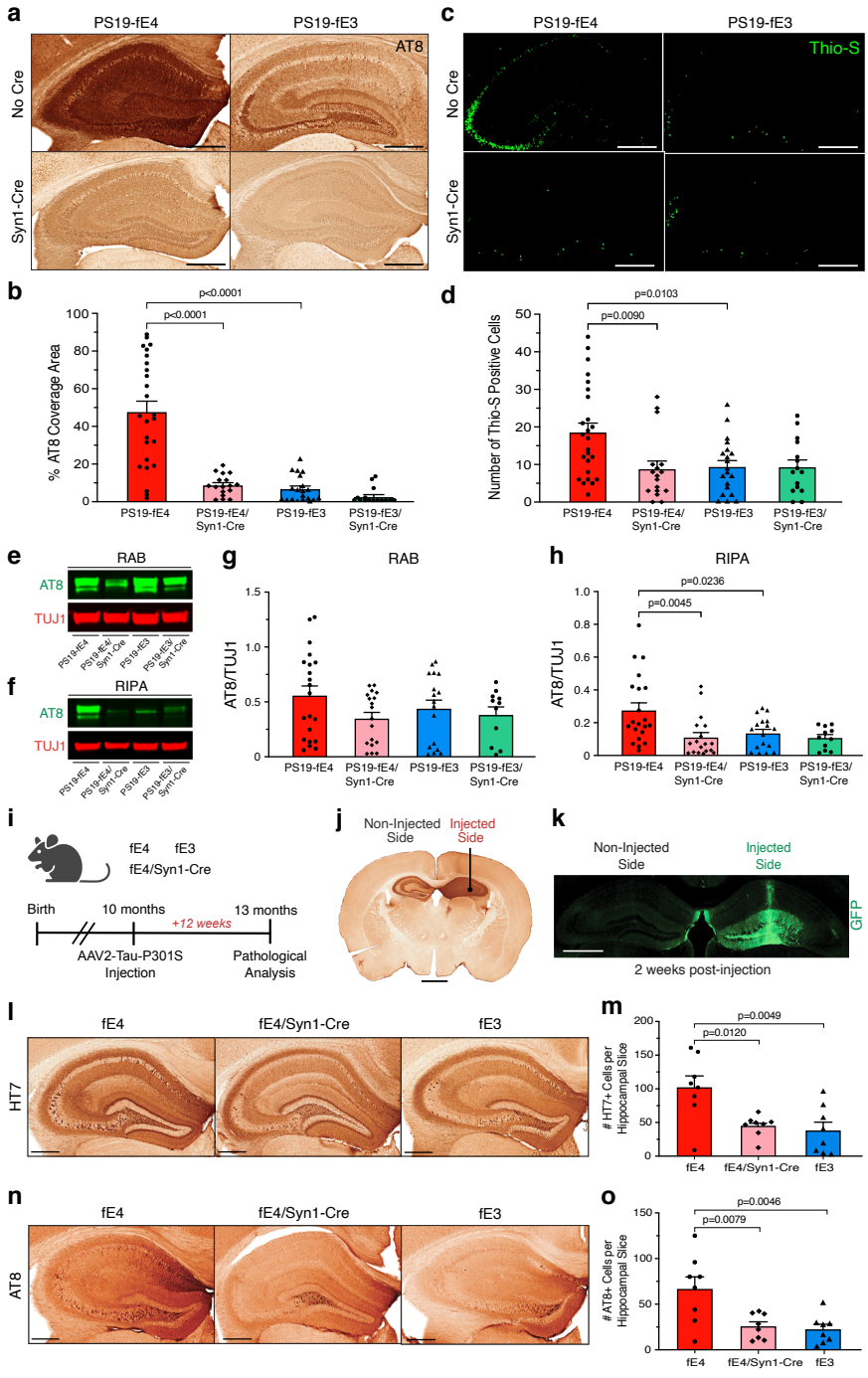

Figure 1.2 Tau pathology accumulation and propagation are significantly reduced in PS19-fE4 mice after removal of APOE4 from neurons. a, Representative images of pTau staining with anti-AT8 in the hippocampus of 10-month-old PS19-fE4 and PS19-fE3 mice with and without Cre (scale bar, 500 μm). **b**, Quantification of the percent pTau (AT8) coverage area in the hippocampus of 10-month-old PS19-fE4 and PS19-fE3 mice with or without Cre. **c,** Representative images of Thioflavine S (Thio-S) staining in the hippocampus of 10-month-old PS19-fE4 and PS19-fE3 mice with and without Cre (scale bar, 500 μm). **d**, Quantification of the number of Thio-S-positive cells in the hippocampus of 10-month-old PS19-fE4 and PS19-fE3

mice with or without Cre. **e,f** Representative images of anti-AT8 (green) and anti-TUJ1 (red) western blots in RAB (e) and RIPA (f) fractions of hippocampal tissue lysates from 10-month-old PS19-fE4 and PS19-fE3 mice with or without Cre. **g,h,** Quantification of AT8-positive pTau levels relative to TUJ1 measured by western blot analysis in RAB (g) and RIPA (h) fractions of the hippocampal lysates from 10-month-old PS19-fE4 and PS19-fE3 mice with or without Cre. **i**, Experimental design of Tau propagation study illustrating the 12-week incubation period following unilateral hippocampal injection of AAV2-Tau-P301S in fE mice with and without Cre. **j**, Representative images of human Tau immunostaining (HT7 antibody) of a fE4 mouse brain 12 weeks post-injection, with the injection site indicated by the black dot and a notch in the left hemisphere to distinguish the non-injected side (scale bar, 1 mm). **k**, Representative image of GFP immunostaining of a 10-month-old fE4 mouse 2 weeks after a unilateral injection with AAV2-GFP, illustrating there is no viral spread to the non-injected hippocampal side (scale bar, 900 µm). **l**, Representative images of human Tau immunostaining (HT7 antibody) on the non-injected hippocampal side of 13-month-old fE mice with and without Cre (scale bar, 500 µm). **m**, Quantification of the average number of HT7 (human Tau)-positive cells in each hippocampal slice on the non-injected hippocampal side of 13-month-old fE mice with or without Cre 12 weeks post-injection. **n**, Representative images of pTau immunostaining (AT8 antibody) on the non-injected hippocampal side of 13-month-old fE mice with or without Cre (scale bar, 500 µm). **o**, Quantification of the average number of AT8 (pTau)-positive cells in each hippocampal slice on the non-injected hippocampal side of 13-month-old fE mice with or without Cre 12 weeks post-injection. For quantifications in b,d, PS19-fE4: No Cre, n=25; Syn1-Cre, n=17; PS19-fE3: No Cre, n=20; Syn1-Cre, n=15. For quantifications in g,h, PS19-fE4: No Cre, n=21; Syn1-Cre, n=18; PS19-fE3: No Cre, n=17; Syn1-Cre, n=11.Quantified data in m,o are n=8 mice per genotype and data in b,d,g,h,m,o are represented as mean ± SEM, one-way ANOVA with Tukey's post hoc multiple comparisons test.

Neurodegeneration is reduced after removal of neuronal APOE4

Next, we evaluated the extent of neurodegeneration in 10-month-old PS19-fE mice after the removal of APOE from neurons. Analyses of hippocampal and posterior lateral ventricle volumes revealed that PS19-fE4 mice exhibited extensive neurodegeneration relative to PS19-fE3 mice (**Fig. 1.3a–c**), which is consistent with a previous study[38]. Neurodegeneration was significantly reduced in PS19-fE4/Syn1-Cre mice, illustrated by increased hippocampal volumes and decreased posterior lateral ventricle volumes (**Fig. 1.3a–c**). Removal of neuronal APOE3 did not significantly impact neurodegeneration (**Fig. 1.3a–c**).

Quantification of the extent of neuronal cell loss within the various subfields of the hippocampus revealed that PS19-fE4 mice had extensive neuron loss in the hippocampal cornu ammonis 1 (CA1) region and the dentate gyrus, while PS19-fE4/Syn1-Cre mice had significantly reduced neuronal cell loss in both CA1 and dentate gyrus subfields of the hippocampus (**Fig. 1.3d–g**). There was no significant difference in neuronal cell layer thickness in PS19-fE3 mice when APOE3 was removed from neurons (**Fig. 1.3d–g**).

Co-immunostaining for cleaved caspase-3 and NeuN was then used to detect postmitotic neurons undergoing apoptosis in the hippocampus (**Fig. 1.3h,i**). Since there were considerable differences in neuronal loss between genotypes (**Fig. 1.3d–g**), we first quantified the number of neurons that were positive or negative for cleaved caspase-3 and then calculated the ratio of cleaved caspase-3 positive to negative neurons to normalize for neuronal cell numbers. Clearly, PS19-fE4 mice had a much higher number of neurons positive for cleaved caspase-3 than PS19-fE3 mice and the removal of neuronal APOE4 significantly decreased the number of neurons positive for cleaved caspase-3 (**Fig. 1.3h,i**), suggesting that neuronal APOE4 promotes apoptosis of postmitotic neurons in the context of tauopathy.

In PS19-fE4 mice, there was a weak, but significant, negative correlation between Tau pathology and hippocampal volume (**Fig. 1.3j**), suggesting that Tau pathology contributes at least to some extent to the neurodegeneration occurring in these mice. There was a strong negative correlation between the volumes of the hippocampus and the posterior lateral ventricle, and a strong positive correlation between the thickness of CA1 and hippocampal volume (**Fig. 1.3k,l**). Taken together, these data illustrate that removal of neuronal APOE4 protects against Tau-mediated neurodegeneration and leads to reduced neuronal cell and hippocampal volume loss.

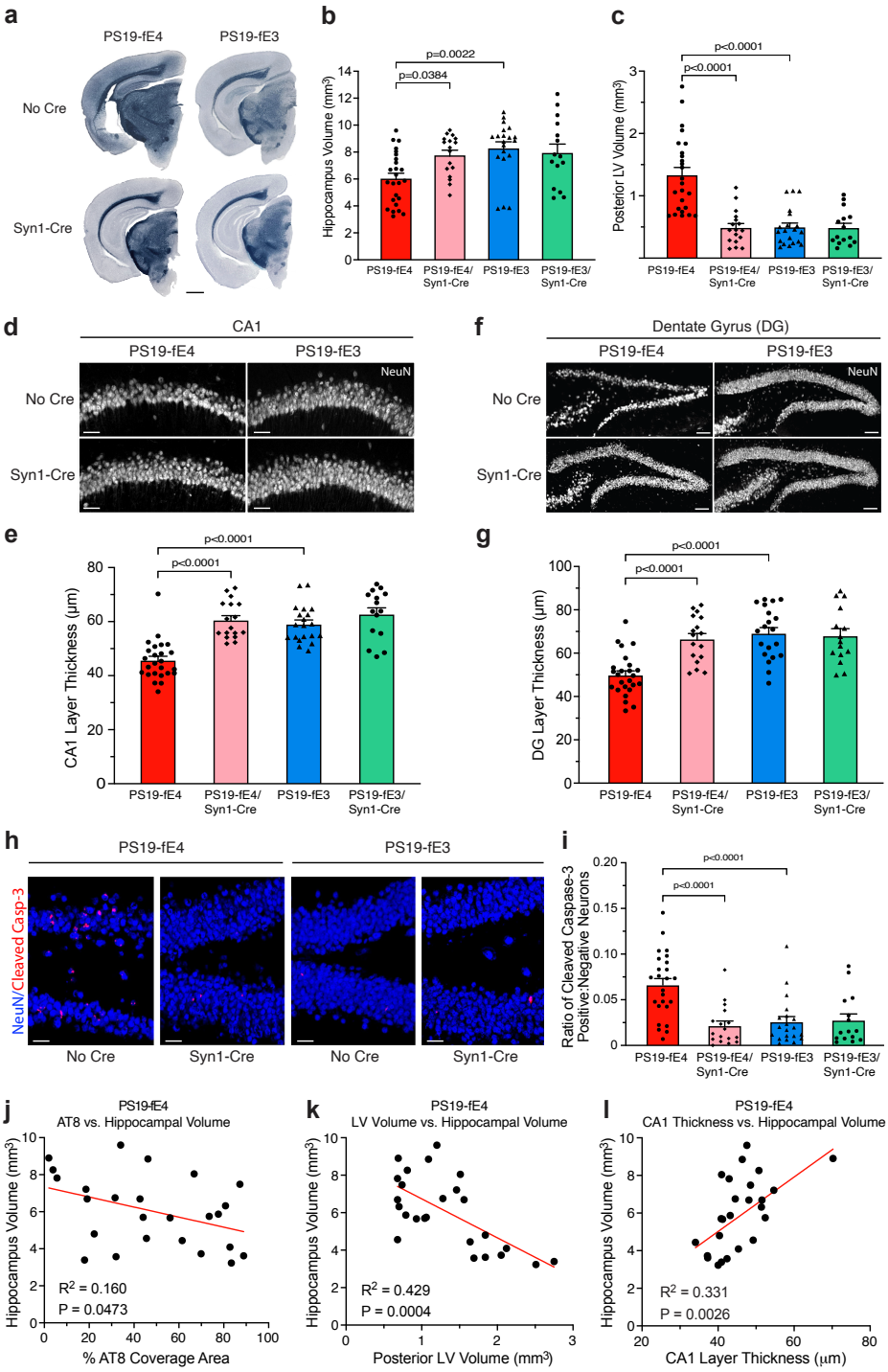

Figure 1.3. Neurodegeneration is significantly reduced after removal of APOE4 from neurons. a, Representative images of the ventral hippocampus of 10-month-old PS19-fE4 and PS19-fE3 mice with and without Cre after staining with Sudan Black to enhance hippocampal visualization (scale bar, 1 mm). **b,c**, Quantification of hippocampal volume (b) and posterior lateral ventricle volume (c) in 10-month-old PS19-fE4 and PS19-fE3 mice with and without Cre. **d**, Representative images of the CA1 hippocampal subfield of 10-month-old PS19-fE4 and PS19-

fE3 mice with and without Cre after immunostaining for neuronal marker NeuN (scale bar, 50 μm). **e**, Quantification of the thickness of the CA1 neuronal cell layer of 10-month-old PS19-fE4 and PS19-fE3 mice with and without Cre. **f**, Representative images of the hippocampal dentate gyrus of 10-month-old PS19-fE4 and PS19-fE3 mice with and without Cre after immunostaining for neuronal marker NeuN (scale bar, 100 μm). **g**, Quantification of the thickness of the dentate gyrus granule cell layer of 10-month-old PS19-fE4 and PS19-fE3 mice with and without Cre. **h**, Representative images of the hippocampal dentate gyrus of 10-month-old PS19-fE4 and PS19-fE3 mice with and without Cre after immunostaining for NeuN and cleaved caspase-3 (scale bar, 50 μm). **i**, Quantification of the ratio of neurons positive:negative for cleaved caspase-3 in the dentate gyrus of 10-month-old PS19-fE4 and PS19-fE3 mice with and without Cre. For all quantifications in b, c, e, g, and i, PS19-fE4: No Cre, n=25; Syn1-Cre, n=17; and PS19-fE3: No Cre, n=20; Syn1-Cre, n=15 mice. All data are represented as mean ± SEM, one-way ANOVA with Tukey's post hoc multiple comparisons test. **j-l**, Correlations between hippocampal volume (mm^3) and AT8 coverage area (%) (j), posterior lateral ventricle volume (mm^3) (k), and CA1 neuronal cell layer thickness (μm) (l) in PS19-fE4 mice (n=25). Pearson's correlation analysis (two-sided). LV, lateral ventricle; CA1, cornu ammonis 1; DG, dentate gyrus.

Myelin deficits and depletion of oligodendrocyte progenitor cells are reduced after removal of APOE4 from neurons

Since myelin degeneration and oligodendrocyte deficits have been observed in human AD brains[10–12] and in mouse models of tauopathy[13–15], we investigated the effects of neuronal APOE4 removal on the maintenance of myelin integrity and the density of hippocampal oligodendrocyte progenitor cells (OPCs). To determine myelin integrity in the hippocampus, we immunostained for myelin basic protein (MBP) and quantified the percent coverage area of MBP in the stratum radiatum underneath the pyramidal cell layer of CA1. PS19-fE4 mice had extensive myelin loss relative to PS19-fE3 mice (**Fig. 1.4a,b**). We observed a significant rescue of myelin loss in PS19-fE4/Syn1-Cre mice that resembled the phenotype of PS19-fE3 mice (**Fig. 1.4a,b**). There were no differences in myelin integrity in PS19-fE3 mice after removal of neuronal APOE3 (**Fig. 1.4a,b**). Immunohistochemical staining for mature oligodendrocytes with anti-Olig2 showed that PS19-fE4 mice had a lower coverage area of oligodendrocytes in the hippocampus relative to PS19-fE3 mice and the removal of neuronal APOE4 significantly increased the coverage area of mature oligodendrocytes (**Fig. 1.4c,d**).

To further characterize the effects of neuronal APOE4 on biological components involved in the myelination process, we immunostained with an NG2 antibody to probe for OPCs, which have been suggested to aid the repair of damaged myelin in conditions of CNS injury and neurodegeneration[15,80]. We observed a significant decrease in the percent OPC coverage area in the hippocampus of PS19-fE4 mice as compared to PS19-fE3 mice (**Fig. 1.4e,f**). Removal of neuronal APOE4 significantly increased the percent OPC coverage area to levels that were similar to those in the PS19-fE3 mice (**Fig. 1.4e,f**). There were no obvious differences in OPC coverage area after removal of neuronal APOE3 in PS19-fE3 mice (**Fig. 1.4e,f**).

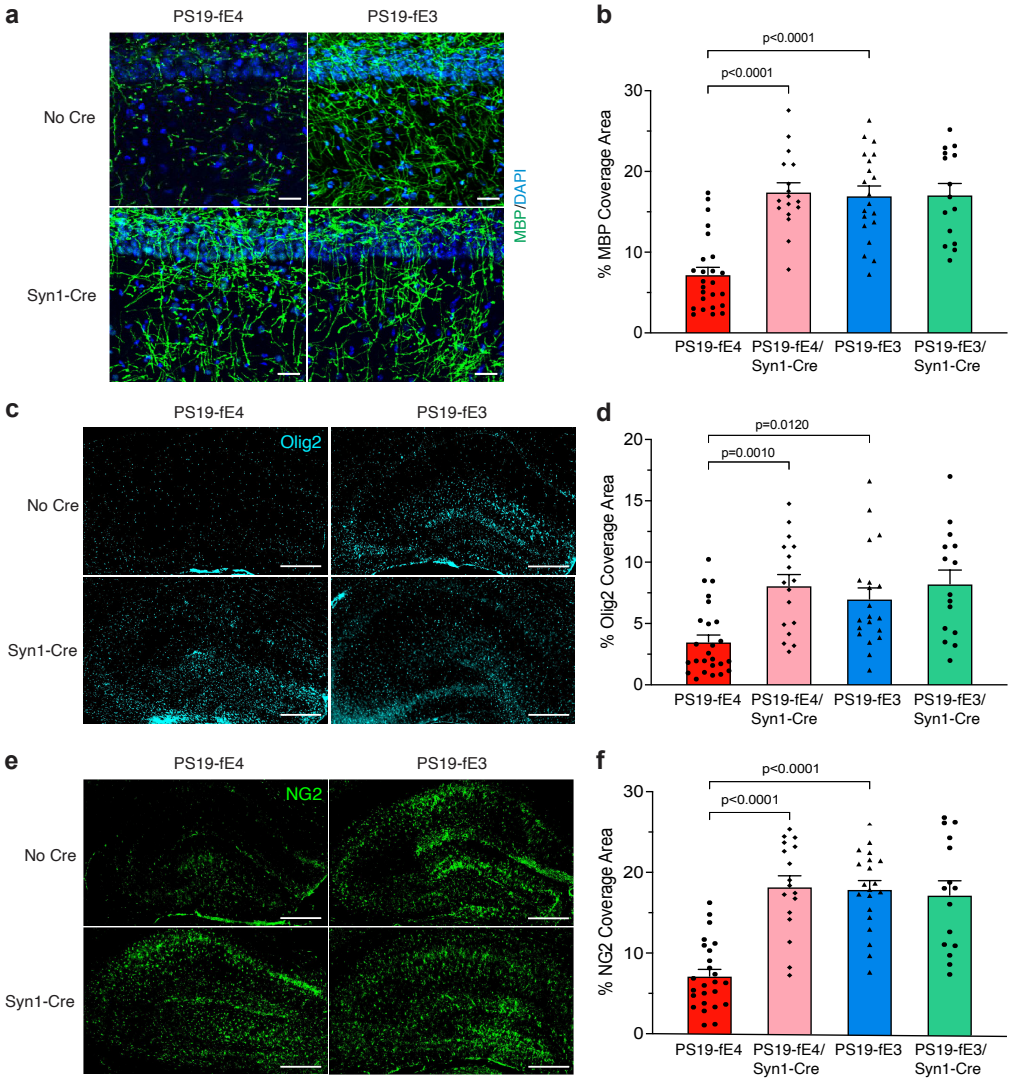

Figure 1.4. Myelin deficits and OPC pool depletion are significantly reduced after removal of APOE4 from neurons. a, Representative images of myelin sheath staining with anti-MBP and DAPI in the stratum radiatum of the hippocampus underneath the pyramidal cell layer of CA1 in 10-month-old PS19-fE4 and PS19-fE3 mice with and without Cre (scale bar, 50 μm). **b**, Quantification of the percent MBP coverage area in the hippocampal CA1 subregion of 10-month-old PS19-fE4 and PS19-fE3 mice with and without Cre. **c**, Representative images of mature oligodendrocytes by immunostaining with anti-Olig2 in the hippocampus of 10-month-old PS19-fE4 and PS19-fE3 mice with and without Cre (scale bar, 500 μm). **d**, Quantification of the percent Olig2 coverage area in the hippocampus of 10-month-old PS19-fE4 and PS19-fE3 mice with and without Cre. **e**, Representative images of oligodendrocyte progenitor cells (OPCs) by immunostaining with anti-NG2 in the hippocampus of 10-month-old PS19-fE4 and PS19-fE3 mice with and without Cre (scale bar, 500 μm). **f**, Quantification of the percent NG2 coverage area in the hippocampus of 10-month-old PS19-fE4 and PS19-fE3 mice with and without Cre. For all quantifications in b,d,f, PS19-fE4: No Cre, n=25; Syn1-Cre, n=17; and PS19-fE3: No Cre, n=20; Syn1-Cre, n=15 mice. All data are represented as mean ± SEM, one-way ANOVA with Tukey's post hoc multiple comparisons test.

Hippocampal network hyperexcitability is eliminated after removal of neuronal APOE4

To determine the effects of neuronal APOE4 on neuronal function in the context of tauopathy, we measured neuronal network excitability in the hippocampal CA1 region of PS19-fE3 mice and PS19-fE4 mice with or without Syn1-Cre by input-output curve analysis of network response to incremental stimulation of Schaffer collaterals (**Fig. 1.5a**)[81]. PS19-fE4 mice had notable CA1 neuron hyperexcitability as compared to PS19-fE3 mice (**Fig. 1.5b**). Removing neuronal APOE4 eliminated neuronal network hyperexcitability (**Fig. 1.5b**), indicating that neuronal APOE4 drives neurodysfunction in the context of tauopathy.

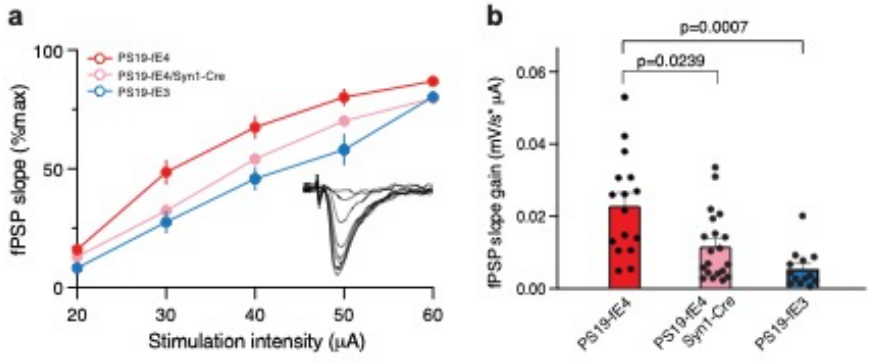

Figure 1.5 Removing neuronal APOE4 ameliorates neuronal hyperexcitability in the hippocampus of PS19-fE4 mice. a, Average normalized fPSP slopes in CA1 stratum radiatum in response to incremental stimulation of Schaffer collaterals. APOE4 expression renders CA3-CA1 network hyperexcitable as evidenced by augmented response to synaptic stimulation. **b**, Calculated individual fPSP slope gain values for all experiments in (a). Note that removal of APOE4 from neurons ameliorates neuronal hyperexcitability in the hippocampus of PS19-fE4 mice. PS19-fE4: n=20,N=4; PS19-fE4/Syn1-Cre: n=25,N=4; PS19-fE3: n=13,N=2. Data is represented as mean ± SEM, one-way ANOVA with Tukey's post hoc multiple comparisons test.

snRNA-seq identifies neurodegenerative disease-associated subpopulations of neurons and oligodendrocytes in APOE4 mice that are largely eliminated by removing neuronal APOE4

In order to gain an in-depth understanding of the cell type-specific effects of neuronal APOE4 at the transcriptomic level across different types of hippocampal cells, we performed snRNA-seq on isolated hippocampi from 10-month-old PS19-fE4 mice with or without Syn1-Cre and PS19-fE3 mice. The snRNA-seq dataset contained 95,156 nuclei covering 25,890 genes after normalization and filtering for quality control. Clustering by the Louvain algorithm[82] and visualization by uniform manifold approximation and projection (UMAP) revealed 34 distinct cell clusters (**Fig. 1.6a**). Based on their expression of marker genes, these clusters were assigned to 17 excitatory (Ex) neuron clusters (4-7, 9, 10, 17-23, 26, 28, 30, 32), 7 inhibitory (In) neuron clusters (3, 8, 11, 13, 24, 27, 31), 3 oligodendrocyte clusters (1, 2, 15), one astrocyte cluster (12), 3 microglia clusters (14, 25, 29), 1 oligodendrocyte progenitor cell (OPC) cluster (16), and 2 unknown clusters (33, 34) (**Fig. 1.6a**). As predicted, APOE was highly expressed in astrocytes (cluster 12) in PS19-fE4 and PS19-fE3 mice and astrocytic APOE4 expression was also high in PS19-fE4/Syn1-Cre mice, validating that the removal of neuronal APOE4 by Syn1-Cre does not alter astrocytic APOE4 expression (**Fig. 1.6b**). As we reported previously[48], some neurons also expressed APOE in PS19-fE4 and PS19-fE3 mice, and neuronal APOE expression was eliminated in PS19-fE4/Syn1-Cre mice (**Fig. 1.6b**). Notably, there seemed to be a reduction in APOE expression in oligodendrocyte clusters 1, 2, and 15 and OPC cluster 16 in PS19-fE4/Syn1-Cre mice after neuronal APOE4 removal (**Fig. 1.6b**). Since $Olig2^+$ oligodendrocytes and $NG2^+$ OPCs did not have any evident Cre recombinase expression by immunohistochemical staining (**Fig. 1.1c,d**) the potential reduction in APOE expression in oligodendrocytes and OPCs in PS19-fE4/Syn1-Cre mice is likely due to a secondary effect in response to the removal of neuronal APOE, which warrants further investigation.

Log odds ratio estimates from a Generalized Linear Mixed Effects Model to assess association with Animal Models (GLMM_AM) was used to identify cell clusters that were altered in PS19-fE3 and PS19-fE4/Syn1-Cre mice versus PS19-fE4 mice. This analysis revealed that excitatory neuron clusters 7 and 18 had significantly lower odds of having cells from PS19-fE4/Syn1-Cre mice than from PS19-fE4 mice, while excitatory neuron clusters 4 and 9 had significantly higher odds of having cells from PS19-fE4/Syn1-Cre mice than from PS19-fE4 mice (**Fig. 1.6c**). Based on differentially expressed (DE) gene analyses, cells in neuron clusters 7 and 18 had significantly upregulated expression of the following genes relative to the other excitatory neuron clusters: three major heat shock proteins (Hspa8, Hsp90aa1, and Hsp90ab1), calmodulin (Calm1 and Calm2), calmodulin-binding protein neurogranin (Nrgn), and ubiquitin B (Ubb) (**Fig. 1.6e,f**). Strikingly, comparison of DE genes in cluster 7 between PS19-fE4/Syn1-Cre and PS19-fE4 mice showed that removal of neuronal APOE4 led to a drastic downregulation of these top upregulated genes (**Fig. 1.6g**). This indicates that excitatory neuron clusters 7 and 18 are not only diminished in PS19-fE4/Syn1-Cre mice, but also that removal of neuronal APOE4 led to a dramatic reversal of the expression of many top upregulated genes in these clusters.

For the cohort of mice used for snRNA-seq analysis, we utilized the left hemisphere of their brains for single nuclei isolation as well as sequencing analysis and performed extensive pathological characterizations of the right hemisphere for each mouse. Therefore, we can assess the relationships between the transcriptomic and pathological data for each cell cluster in this cohort of mice (**Fig. 1.6h**). Log odd ratio estimates from another Generalized Linear Mixed Effects Model to assess associations with histopathology (GLMM_histopathology) revealed that the proportion of cells in clusters 7 and 18 exhibited significant negative associations with hippocampal volume and positive associations with the coverage area of pTau (**Fig. 1.6h**), indicating that clusters 7 and 18 represent neuronal APOE4-promoted disease-associated neurons (nE4-DANs). The

proportion of cells in excitatory neuron cluster 7 also had a significant negative association with OPC coverage area (**Fig. 1.6h**). Furthermore, the proportion of cells in neuronal clusters 4 and 9, which were enriched in PS19-fE4/Syn1-Cre versus PS19-fE4 mice (**Fig. 1.6d**), exhibited significant positive associations with hippocampal volume and negative associations with pTau coverage area (**Fig. 1.6h**). All these associations further support the notion that neuronal clusters 7 and 18 are nE4-DANs and that neuronal clusters 4 and 9 are associated with protection against Tau pathology and hippocampal degeneration. Taken together, all these data illustrate that neuronal APOE4 removal diminishes the presence of the nE4-DANs and enriches the protective neuronal clusters.

Additionally, oligodendrocyte cluster 15 had significantly lower odds and oligodendrocyte cluster 1 had significantly higher odds of having cells from PS19-fE4/Syn1-Cre mice than from PS19-fE4 mice (**Fig. 1.7a,b**). DE pathway analysis revealed the enrichment of KEGG pathways related to general neurodegeneration, AD, and other neurodegenerative diseases (**Fig. 1.7c**), indicating that cluster 15 represents neuronal APOE4-promoted disease-associated oligodendrocytes (nE4-DAOs). DE gene analysis revealed that cells in oligodendrocyte cluster 15 exhibited a drastically upregulated expression of the following genes: three major heat shock proteins (Hspa8, Hsp90aa1, and Hsp90ab1), calmodulin (Calm1 and Calm2), calmodulin-binding protein neurogranin (Nrgn), and ubiquitin B (Ubb), (**Fig. 1.7d,e**) and a significantly downregulated expression of myelin basic protein (Mbp) and myelin associated oligodendrocyte basic protein (Mobp) genes relative to the other oligodendrocyte clusters.

A recent study identified a subset of disease-associated oligodendrocytes in mouse models of neurodegenerative diseases[83]. Comparison of the marker genes of our nE4-DAOs with this previous study showed some overlap, as nE4-DAOs also had upregulation of Snca, APOE, Fxyd7, B2M, and H2-D1 gene expression compared to the other oligodendrocyte clusters (**Fig.**

1.7d). However, we also saw a dramatically upregulated (Hspa8, Hsp90aa1, Hsp90ab1, Calm1, Calm2, Nrgn, and Ubb) and downregulated (Frmd5, Kirrel3, Pcdh9, Prr5l, Pde4b, Rnf220, and St18) gene expression patterns that were unique to the nE4-DAOs identified in the current study, indicating that these are nE4-DAO marker genes (**Fig. 1.7d,e**). Furthermore, comparison of DE genes in cluster 15 between PS19-fE4/Syn1-Cre and PS19-fE4 mice showed that many of the top upregulated marker genes, such as Calm1, Calm2, Nrgn, and Ubb, were drastically downregulated after removal of neuronal APOE4 (**Fig. 1.7f**). Taken together, these data indicate that the removal of neuronal APOE4 not only diminishes the nE4-DAO cluster 15, but also leads to a dramatic reversal of the expression of many top upregulated marker genes in nE4-DAOs.

Log odd ratio estimates from a Generalized Linear Mixed Effects Model to assess associations with histopathology (GLMM_histopathology) revealed that the proportion of cells in the nE4-DAO cluster 15 exhibited significant negative associations with hippocampal volume and MBP coverage area and positive association with the coverage area of pTau (**Fig. 1.6h**). On the other hand, oligodendrocyte cluster 1, which was significantly enriched in PS19-fE4/Syn1-Cre versus PS19-fE4 mice (**Fig. 1.7b**), exhibited a significant positive association with hippocampal volume and OPC coverage area and negative associations with pTau coverage area (**Fig. 1.6h**). All these associations further support the notion that oligodendrocytes in cluster 15 are nE4-DAOs and that oligodendrocytes in cluster 1 are protective oligodendrocytes against degeneration. Immunohistochemical staining for $Olig2^{+}$ oligodendrocytes that were double-positive for two distinct gene markers of nE4-DAOs in cluster 15, HSP90 and Ubb (**Fig. 1.7d,e**), in the hippocampus of 10-month-old mice showed that these nE4-DAOs are highly present in PS19-fE4 mice and significantly decreased in PS19-fE4/Syn1-Cre mice (**Fig. 1.7g,h**). Taken together, all these data illustrate that neuronal APOE4 removal diminishes the presence of the nE4-DAOs and enriches the disease-protective oligodendrocytes.

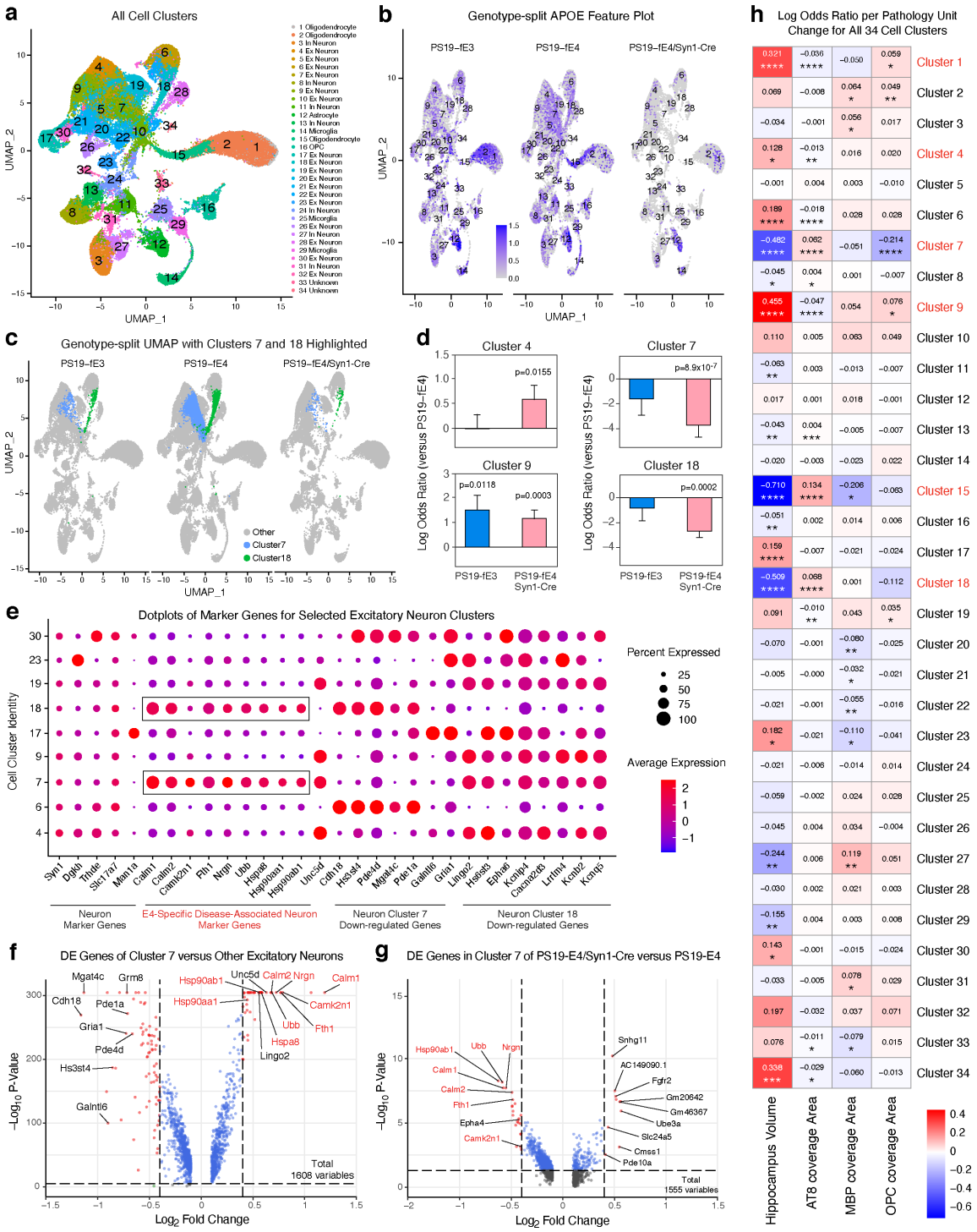

Figure 1.6. Neuronal APOE4 removal eliminates neurodegenerative disease-associated subpopulations of neurons identified by snRNA-seq analysis. a, UMAP plot of all 34 distinct cell clusters in the hippocampi of 10-month-old PS19-fE4 mice with no Cre (n=4), or Syn1-Cre (n=4), and PS19-fE3 mice with no Cre (n=3). **b**, Feature plot illustrating the relative levels of normalized human *APOE* gene expression across all 34 hippocampal cell clusters in the various mouse genotype groups. **c**, UMAP plot highlighting cells in hippocampal cell clusters 7 and 18 (excitatory neurons) for each mouse genotype group. **d**, Bar plot of the mean estimates of log

odds ratio for clusters 4, 7, 9, and 18, which represents the change in the log odds of cells per sample from PS19-fE4/Syn1-Cre and PS19-fE3 mice belonging to the respective clusters compared to the log odds of cells per sample from PS19-fE4 mice. **e**, Dot-plot of normalized average expression of marker genes for selected excitatory neuron clusters, highlighting genes that are significantly upregulated and downregulated in excitatory neuron cluster 7 and 18. The size of the dots is proportional to the percentage of cells expressing a given gene. **f,** Volcano plot of the differentially expressed (DE) genes between excitatory neuron cluster 7 and all other excitatory neuron clusters. **g,** Volcano plot of the DE genes in excitatory neuron cluster 7 in PS19-fE4/Syn1-Cre mice versus PS19-fE4 mice. **h**, Heatmap plot of the log odds ratio per unit change in each pathological parameter for all cell clusters, with clusters that have significantly increased or decreased logs odds ratio after neuronal APOE4 removal highlighted in red (refer to d). The log odds ratio represents the mean estimate of the change in the log odds of cells per sample from a given animal model, corresponding to a unit change in a given histopathological parameter. Negative associations are shown in blue and positive associations are shown in red. P-values in d are from fits to a GLMM_AM and p-values in h are unadjusted from fits to a GLMM_histopathology (see Supplementary Table 2 and Methods for details). All error bars represent the standard error. Ex Neuron, excitatory neuron; In Neuron, inhibitory neuron; OPC, oligodendrocyte precursor cell.

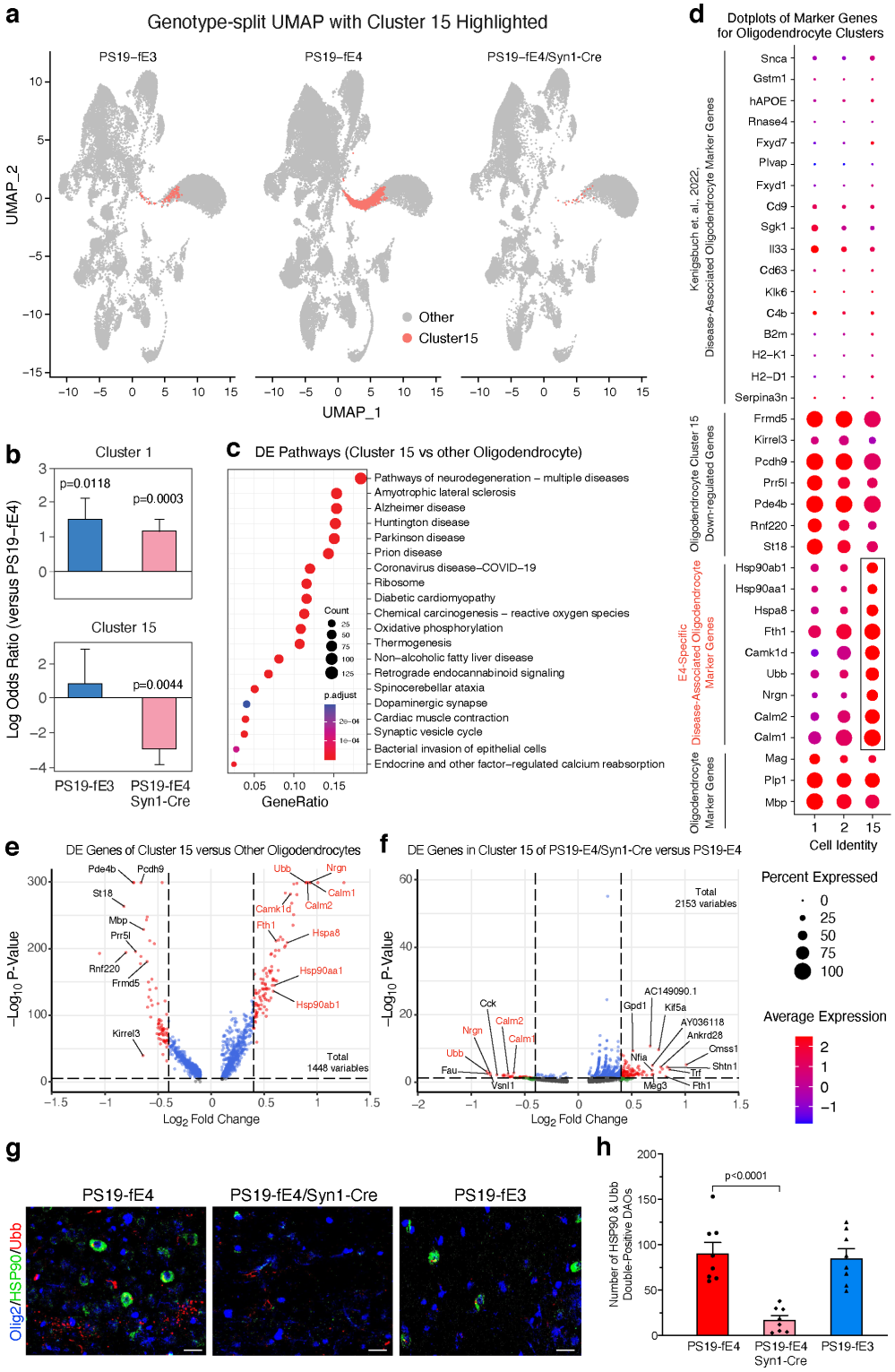

Fig. 1.7 Neuronal APOE4 removal reduces disease-associated oligodendrocytes (DAOs). **a**, UMAP plot highlighting cells in hippocampal cell cluster 15 for each mouse genotype group. **b**, Bar plot of the mean estimates of log odds ratio for clusters 1 and 15, which represents the change in the log odds of cells per sample from PS19-fE4/Syn1-Cre and PS19-fE3 mice belonging to the

respective clusters compared to the log odds of cells per sample from PS19-fE4 mice. **f**, Dot-plots of the top 20 KEGG pathways significantly enriched for the differentially expressed genes of oligodendrocyte cluster 15 versus all other oligodendrocyte clusters. **d**, Dot-plot of normalized average expression of marker genes for oligodendrocyte clusters, highlighting genes that are significantly upregulated in oligodendrocyte cluster 15. The size of the dots is proportional to the percentage of cells expressing a given gene. **e,** Volcano plot of the differentially expressed (DE) genes between oligodendrocyte cluster 15 and all other oligodendrocyte clusters. **f,** Volcano plot of the DE genes in oligodendrocyte cluster 15 in PS19-fE4/Syn1-Cre mice versus PS19-fE4 mice. **g**, Immunohistochemical staining for Olig2 and two markers (Hsp90 and Ubb) that are upregulated in the disease-associated oligodendrocyte cluster 15 in the hippocampus of 10-month-old PS19-fE4, PS19-fE4/Syn1-Cre, and PS19-fE3 mice (scale bar, 50 μm). **h**, Quantification of the number of Olig2+ oligodendrocytes that are double-positive for Hsp90 and Ubb in the hippocampus of 10-month-old PS19-fE4, PS19-fE4/Syn1-Cre, and PS19-fE3 mice. Data in h are represented as mean ± SEM, one-way ANOVA with Tukey's post hoc multiple comparisons test.

Gliosis is drastically reduced after removal of neuronal APOE4

Based on our observation that neuronal APOE4 removal reduces the extent of neurodegeneration as well as myelin and OPC deficits and diminishes disease-associated subpopulations of neurons and oligodendrocytes, we then investigated the effect of neuronal APOE4 on gliosis since it has been suggested that glial cells drive degeneration in this tauopathy model[9]. We examined the extent of microgliosis and astrogliosis within these various genotype groups at 10 months of age. PS19-fE4 mice had a high percent coverage area of Iba1$^+$ microglia in the hippocampus while PS19-fE4/Syn1-Cre mice had a significantly lower coverage area of Iba1$^+$ microglia (**Fig. 1.8a,b**). We also immunostained with a CD68 antibody, which is a marker of activated microglia[84]. PS19-fE4 mice exhibited extensive microglial activation that was significantly reduced after removal of neuronal APOE4 (**Fig. 1.8d,e**). In PS19-fE3 mice, there was no significant reduction in the coverage areas of Iba1$^+$ microglia and CD68$^+$ activated microglia after removal of neuronal APOE3 (**Fig. 1.8a,b,d,e**). These data indicate that microgliosis is strongly increased by APOE4 relative to APOE3 in the setting of tauopathy, and that removal of APOE4 from neurons attenuates the extent of microgliosis.

There was also a strong negative correlation between Iba1 coverage area and hippocampal volume in PS19-fE4 mice (**Fig. 1.8c**). Interestingly, of all pathological correlations made in PS19-fE4 mice, the coverage area of CD68$^+$ activated microglia had the strongest negative correlation with hippocampal volume (**Fig. 1.8f**), suggesting that the extent of microglial activation is the strongest indicator and potential contributor to APOE4-promoted hippocampal degeneration in tauopathy.

We next assessed the extent of astrogliosis after removal of APOE from neurons. PS19-fE4 mice exhibited a significantly higher coverage area of GFAP$^+$ astrocytes in the hippocampus relative to

PS19-fE3 mice (**Fig. 1.8g,h**). The coverage area of $GFAP^+$ astrocytes was greatly reduced after removal of neuronal APOE4 (**Fig. 1.8g,h**). These observations were also supported by immunohistochemical staining for an activated astrocytic marker, S100β[85], showing that removal of neuronal APOE4 greatly reduces the coverage area of activated astrocytes (**Fig. 1.8j,k**). There was no obvious difference in the extent of astrogliosis after removal of neuronal APOE3 relative to PS19-fE3 mice (**Fig. 1.8g,h,j,k**). Neither the coverage area of astrocytes nor activated astrocytes was significantly correlated with hippocampal volume in this cohort (**Fig. 1.8i,l**). These data indicate that APOE4 strongly enhances astrogliosis relative to APOE3 in tauopathy, and that the removal of APOE4 from neurons eliminates this phenotype.

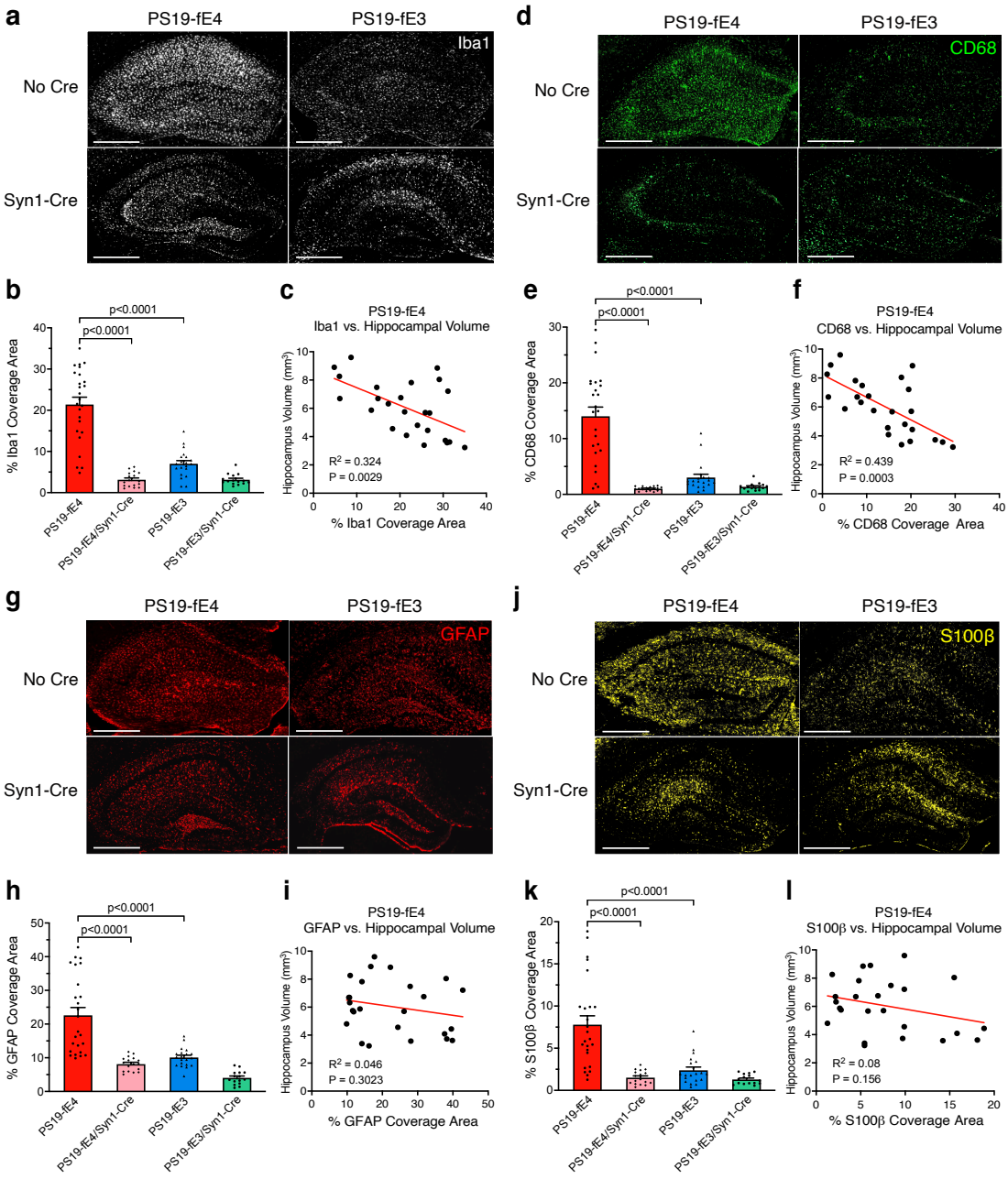

Figure 1.8. Microgliosis and astrogliosis are significantly reduced after APOE4 is removed from neurons. **a**, Representative images of microglia immunostaining with anti-Iba1 in the hippocampus of 10-month-old PS19-fE4 and PS19-fE3 mice with and without Cre (scale bar, 500 μm). **b**, Quantification of the percent Iba1 coverage area in the hippocampus of 10-month-old PS19-fE4 and PS19-fE3 mice with and without Cre. **c**, Correlation between percent Iba1 coverage area and hippocampal volume of PS19-fE4 mice (n=25). **d**, Representative images of activated microglia immunostaining with anti-CD68 in the hippocampus of 10-month-old PS19-fE4 and PS19-fE3 mice with and without Cre (scale bar, 500 μm). **e**, Quantification of percent CD68 coverage area in the hippocampus of 10-month-old PS19-fE4 and PS19-fE3 mice with and without Cre. **f**, Correlation between percent CD68 coverage area and hippocampal volume of

PS19-fE4 mice (n=25). **g**, Representative images of astrocyte immunostaining with anti-GFAP in the hippocampus of 10-month-old PS19-fE4 and PS19-fE3 mice with and without Cre (scale bar, 500 μm). **h**, Quantification of percent GFAP coverage area in the hippocampus of 10-month-old PS19-fE4 and PS19-fE3 mice with and without Cre. **i**, Correlation between percent GFAP coverage area and hippocampal volume of PS19-fE4 mice (n=25). **j**, Representative images of activated astrocyte immunostaining with anti-S100β in the hippocampus of 10-month-old PS19-fE4 and PS19-fE3 mice with and without Cre (scale bar, 500 μm). **k**, Quantification of percent S100β coverage area in the hippocampus of 10-month-old PS19-fE4 and PS19-fE3 mice with and without Cre. **l**, Correlation between percent S100β coverage area and hippocampal volume of PS19-fE4 mice (n=25). For quantifications in b, e, h, and k, PS19-fE4: No Cre, n=25; Syn1-Cre, n=17; and PS19-fE3: No Cre, n=20; Syn1-Cre, n=15 mice. All data are represented as mean ± SEM, one-way ANOVA with Tukey's post hoc multiple comparisons test. Pearson's correlation analysis (two-sided).

Removal of neuronal APOE4 increases disease-protective astrocytes and decreases disease-associated astrocytes

Based on our observation that neuronal APOE4 significantly reduces the extent of gliosis, we aimed to gain deeper insights into the cell type-specific effects of neuronal APOE4 on subtypes of glial cells by additional analyses of our snRNA-seq dataset. Further subclustering of astrocytes (cluster 12 in **Fig. 1.6a**) identified 15 astrocyte subpopulations (**Fig. 1.9a**). Log odds ratio estimates from a GLMM_AM revealed that astrocyte subcluster 1 had higher odds of having cells from PS19-fE4/Syn1-Cre mice than from PS19-fE4 mice, whereas astrocyte subcluster 5 had lower odds of having cells from PS19-fE4/Syn1-Cre mice than from PS19-fE4 mice, with a complete elimination of subcluster 5 in PS19-fE4/Syn1-Cre mice (**Fig. 1.9b,c**). Interestingly, astrocyte subcluster 5 highly expressed APOE (**Fig. 1.9d**). DE gene analysis revealed that astrocyte subcluster 1 highly expressed the homeostatic astrocyte genes Luzp2, Trpm2, Slc7a10, and GPC5, while astrocyte subcluster 5 had downregulation of these homeostatic gene expression and drastic upregulation of Hsp8a, Hsp90aa1, Hsp90ab1, Calm1, Calm2, Nrgn, and Ubb gene expression relative to other astrocyte subclusters (**Fig. 1.9e**). Since astrocyte subcluster 5 was completely eliminated in PS19-fE4/Syn1-Cre mice (**Fig. 1.9b**), we could not analyze the effect of removing neuronal APOE4 on the marker gene expression in this subcluster.

Log odds ratio estimates from a GLMM_histopathology revealed that the proportion of cells in astrocyte subcluster 5 exhibited a significant negative association with hippocampal volume and MBP coverage area and a significant positive association with the coverage area of pTau (**Fig. 1.9f**), indicating that this subcluster represents neuronal APOE4-promoted disease-associated astrocytes (nE4-DAAs). Meanwhile, astrocyte subcluster 1 exhibited a significant positive association with hippocampal volume and a significant negative association with the coverage area of pTau (**Fig. 1.9f**), supporting the notion that astrocyte subcluster 1 represents disease-

protective astrocytes. Comparison with a recent study that described a subset of DAAs in mouse models of AD showed a similar upregulation of some of the specific marker genes, such as Ctsb, Vim, and APOE, as observed in the previously described subset of DAAs[86]. Still, we saw a strong upregulation of a set of marker genes (Hspa8, Hsp90aa1, Hsp90ab1, Calm1, Calm2, Nrgn, and Ubb) unique to the nE4-DAAs identified in this study (**Fig. 1.9e**), supporting the notion that these are nE4-DAA marker genes. Taken together, all these data illustrate that neuronal APOE4 removal diminishes the presence of the nE4-DAAs and enriches the disease-protective astrocytes.

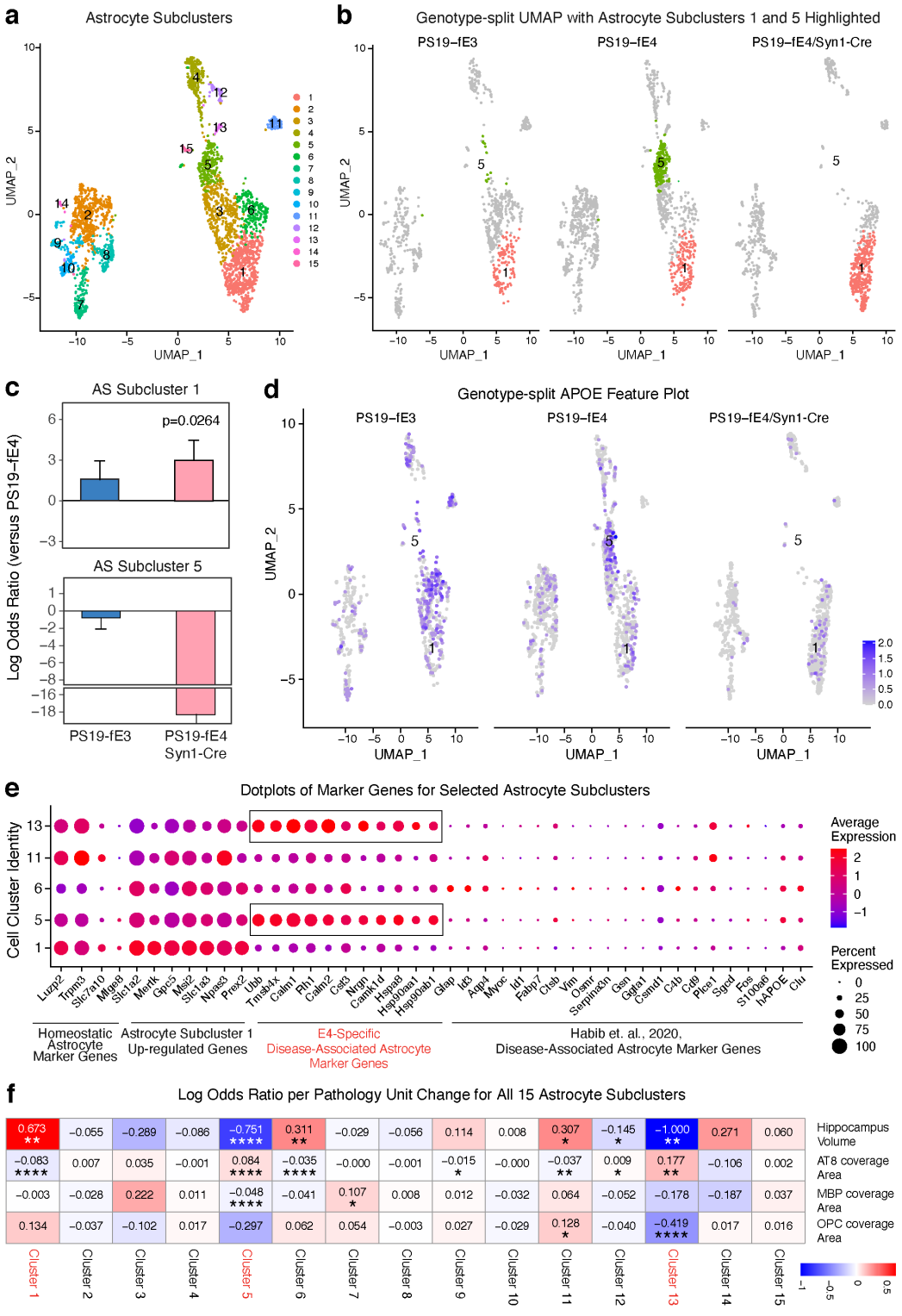

Figure 1.9. Neuronal APOE4 removal increases disease-protective astrocytes and eliminates disease-associated astrocytes identified by snRNA-seq analysis. a, UMAP plot of 15 astrocyte subclusters after sub-clustering hippocampal cell cluster 12. **b**, UMAP plot highlighting cells in astrocyte subclusters 1 and 5 in PS19-fE4 mice with no Cre (n=4), Syn1-Cre

(n=4), and PS19-fE3 mice with no Cre (n=3). **c**, Bar plot of the mean estimates of log odds ratio for astrocyte subclusters 1 and 5. There are no cells from PS19-fE4 Syn1-Cre mice in astrocyte subcluster 5, so statistical significance and standard errors are not reported. **d**, Feature plot illustrating the relative levels of normalized human *APOE* gene expression across all astrocyte subclusters for each mouse genotype group. **e**, Dot-plot of normalized average expression of marker genes for selected astrocyte subclusters, highlighting genes that are significantly upregulated and downregulated in astrocyte subclusters 5 and 13. **f**, Heatmap plot of the log odds ratio per unit change in each pathological parameter for all astrocyte subclusters, with clusters that have significantly increased or decreased logs odds ratio after neuronal APOE4 removal highlighted in red (refer to c). Negative associations are shown in blue and positive associations are shown in red. P-values in c are from fits to a GLMM_AM and p-values in f are unadjusted from fits to a GLMM_histopathology (see Methods for details). All error bars represent the standard error. AS, astrocytes.

Removal of neuronal APOE4 increases disease-protective microglia and decreases disease-associated microglia

Further subclustering microglia (clusters 14, 25, and 29 in **Fig. 5a**) identified 15 microglial subpopulations (**Fig. 1.10a**). Log odds ratio estimates from a GLMM_AM revealed that microglia subclusters 6 and 8 had lower odds of having cells from PS19-fE4/Syn1-Cre mice than from PS19-fE4 mice, while microglia subcluster 4 have higher odds of having cells from PS19-fE4/Syn1-Cre mice than from PS19-fE4 mice (**Fig. 1.10b,c**). Interestingly, microglia subcluster 6 highly expressed APOE (**Fig. 1.10d**). DE gene analysis revealed that microglia subcluster 4 had an upregulated expression of Pde4b, Nkain2, St18, Prr5l, and Pcdh9 genes, while microglia subclusters 6 and 8 had an upregulated expression of Hspa8, Hsp90aa1, Hsp90ab1, Calm1, Calm2, Nrgn, and Ubb genes, relative to other microglia subclusters (**Fig. 1.10e**).

Log odds ratio estimates from a GLMM_histopathology revealed that the proportion of cells in microglia subcluster 6 and 8 both exhibited significant negative associations with hippocampal volume and significant positive associations with the coverage area of pTau (**Fig. 1.10f**), suggesting that subcluster 4 represents synaptic-function-supporting microglia and subclusters 6 and 8 represent neuronal APOE4-promoted disease-associated microglia (nE4-DAMs). Meanwhile, microglia subcluster 4 exhibited a significant positive association with hippocampal volume and a negative association with the coverage area of pTau (**Fig. 1.10f**), supporting the notion that microglia subcluster 4 represents a disease-protective subpopulation of microglia. Microglia subcluster 3 also exhibited a significant positive association with hippocampal volume and a significant positive association with the coverage area of pTau (**Fig. 1.10f**), although there were no differences in log odds ratio between PS19-fE4 and PS19-fE4/Syn1-Cre or PS19-fE3 mice for this subcluster. Comparison with a recent study that described a subset of DAMs in AD mouse models showed a similar upregulation of specific gene markers Ctsb and Fth1 as observed

in the previously described subset of DAM[87]. On the other hand, we also observed considerable upregulation of a set of genes (Hspa8, Hsp90aa1, Hsp90ab1, Calm1, Calm2, Nrgn, and Ubb) unique to the nE4-DAMs identified in this study (**Fig. 1.10e**), supporting the notion that these are nE4-DAM marker genes.

Taken together, this data illustrates that neuronal APOE4 promotes the accumulation of disease-associated astrocytes and microglia but diminishes disease-protective astrocytes and microglia and that its removal can effectively eliminate these detrimental effects of neuronal APOE4.

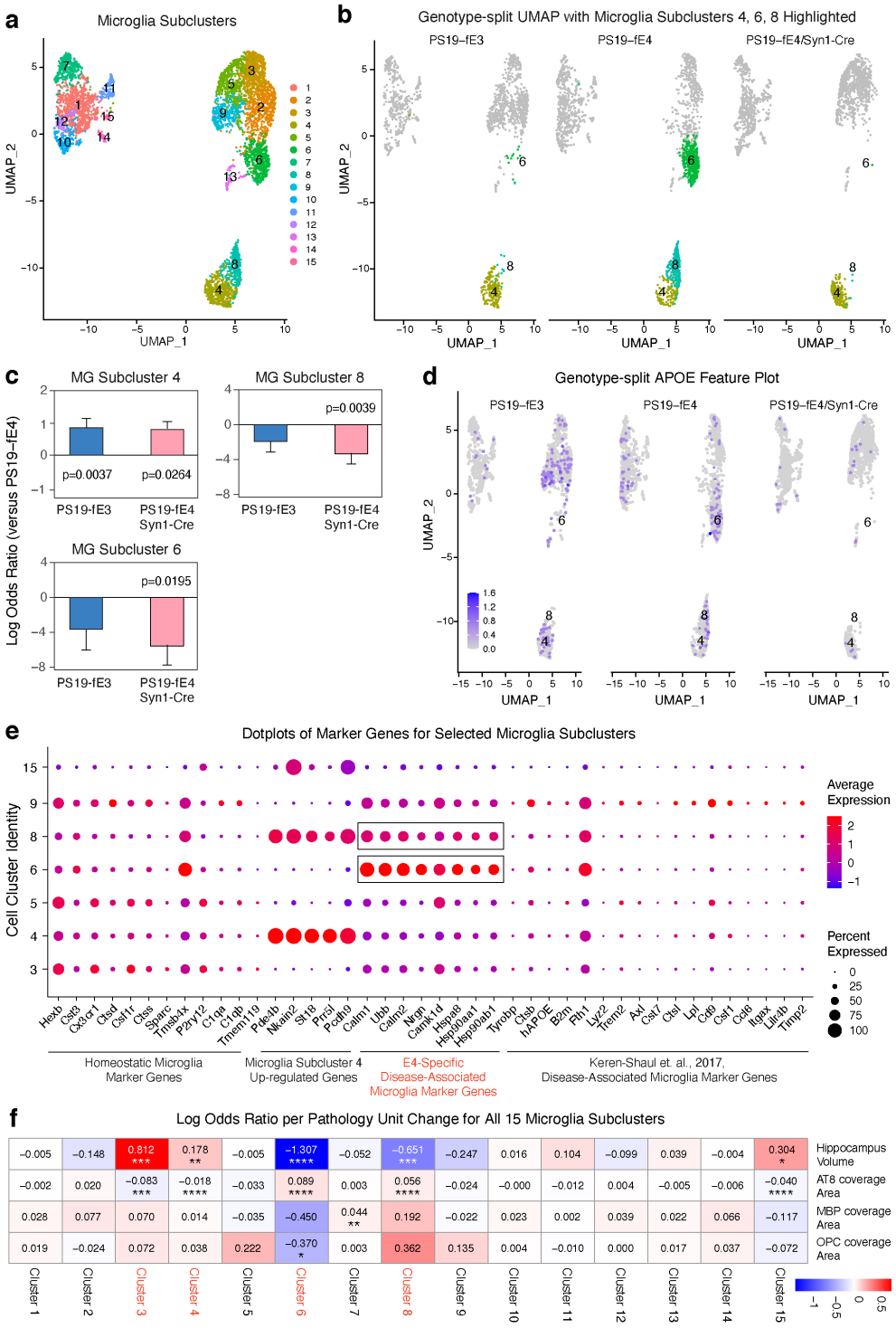

Figure 1.10. Neuronal APOE4 removal increases disease-protective microglia and eliminates disease-associated microglia identified by snRNA-seq analysis. a, UMAP plot of 15 microglia subclusters after sub-clustering hippocampal cell clusters 14, 25, and 29. **b**, UMAP plot highlighting cells in microglia subclusters 4, 6, and 8 in PS19-fE4 mice with no Cre (n=4), Syn1-Cre (n=4), and PS19-fE3 mice with no Cre (n=3). **c**, Bar plot of the mean estimates of log

odds ratio for microglia subclusters 4, 6, and 8. **d**, Feature plot illustrating the relative levels of normalized human *APOE* gene expression across all microglia subclusters for each mouse genotype group. **e**, Dot-plot of normalized average expression of marker genes for selected microglia subclusters, highlighting genes that are significantly upregulated and downregulated in microglia subclusters 6 and 8. **f**, Heatmap plot of the log odds ratio per unit change in each pathological parameter for all microglia subclusters, with clusters that have significantly increased or decreased logs odds ratio after neuronal APOE4 removal highlighted in red (refer to c). Negative associations are shown in blue and positive associations are shown in red. P-values in c are from fits to a GLMM_AM and p-values in f are unadjusted from fits to a GLMM_histopathology (see Methods for details). All error bars represent the standard error. MG, microglia.

Discussion

APOE4 is produced by a variety of cell types within the CNS, the majority of which is produced by astrocytes while a lesser portion is produced by neurons under conditions of stress or injury[31,42,48,56]. It has been suggested that APOE4 exerts different pathogenic effects depending on its cellular source[39–41]. While previous studies have provided a detailed characterization of astrocytic APOE4 effects in the context of tauopathy[40], there is a considerable gap in our understanding of the exact roles of neuronal APOE4 in the development of Tau-mediated deficits in AD pathogenesis.

In the present study, we investigate the roles of neuronal APOE4 in promoting the development of prominent AD pathologies in a tauopathy mouse model. We demonstrate that the removal of neuronal APOE4 has wide-ranging beneficial effects, leading to drastic reductions in [1] the accumulation of Tau pathology and spread of pathological Tau throughout the hippocampus, [2] neurodegeneration and hippocampal neuron loss, [3] myelin deficits and depletion of OPCs, [4] neuronal network hyperexcitability, [5] microgliosis and astrogliosis, and [6] the accumulation of neuronal APOE4-promoted disease-associated cell subpopulations. These findings illustrate that neuronal APOE4 is a potent driver of these AD-related pathologies and that its removal is sufficient to attenuate these phenotypes. Thus, this study reveals a central role of neuronal APOE4 in the pathogenesis of APOE4-driven AD and provides new insights into potential therapeutic targets to combat APOE4-related AD, such as through the removal or reduction of neuronal APOE4.

The detrimental effects of neuronal APOE4 were further exemplified by snRNA-sequencing analysis, which revealed that removal of neuronal APOE4 eliminated the presence of neuronal APOE4-promoted disease-associated subpopulations of neurons (nE4-DANs), oligodendrocytes (nE4-DAOs), astrocytes (nE4-DAAs), and microglia (nE4-DAMs) that were enriched in APOE4-

expressing tauopathy mice and correlated to the severity of Tau pathology, neurodegeneration, and myelin deficits. This data indicates that neuronal APOE4 not only drives overt pathological changes in the loss of neurons and myelin and the accumulation of activated glial cells, but it also drives subpopulations of these important cell types towards unhealthy states marked by neuronal APOE4-promoted disease-associated gene signatures. The identified nE4-DANs are reported for the first time in our study. The disease-associated oligodendrocytes (DAOs)[83,88],disease-associated astrocytes (DAAs)[86], and disease-associated microglia (DAMs)[87] have been reported in previous studies using AD mouse models or human AD brain tissues and have provided critical information for better understanding of AD pathogenesis at a cell type-specific level. However, all these previously identified disease-associated subpopulations of cells are not justified for APOE genotype-promoted effects. Our identified nE4-DAOs, nE4-DAAs, and nE4-DAMs have unique gene expression signatures promoted by neuronal expression of APOE4. Interestingly, these unique gene expression signatures focus on heat shock proteins, calmodulin and its signaling-related proteins, and ubiquitin, all of which are involved in tauopathy and AD pathogenesis[89–91]. Further analysis and validation of these gene signatures in future studies may provide clues to the underlying pathogenic mechanism of neuronal APOE4.

All in all, our study identifies neuronal APOE4 as a strong driver of many important AD pathologies and demonstrates that it has a potent effect on promoting Tau pathology, gliosis and accumulation of disease-associated glial subpopulations, and subsequent degenerative phenotypes. Thus, neuronal APOE4 plays a central role in the pathogenesis of APOE4-related AD and should be considered as a therapeutic target for developing drugs combating APOE4's detrimental effects in AD and other tauopathies.

References

1. Orr, M. E., Sullivan, A. C. & Frost, B. A brief overview of tauopathy: causes, consequences, and therapeutic strategies. *Trends Pharmacol Sci* **38**, 637–648 (2017).
2. Kosik, K. S. & Shimura, H. Phosphorylated tau and the neurodegenerative foldopathies. *Biochim Biophys Acta* **1739**, 298–310 (2005).
3. Ballatore, C., Lee, V. M. Y. & Trojanowski, J. Q. Tau-mediated neurodegeneration in Alzheimer's disease and related disorders. *Nat Rev Neurosci* **8**, 663–672 (2007).
4. Huang, Y. & Mucke, L. Alzheimer mechanisms and therapeutic strategies. *Cell* **148**, 1204–1222 (2012).
5. Rajan, K. B. *et al.* Population estimate of people with clinical Alzheimer's disease and mild cognitive impairment in the United States (2020-2060). *Alzheimers Dement* **17**, 1966–1975 (2021).
6. Josephs, K. A. *et al.* Beta-amyloid burden is not associated with rates of brain atrophy. *Ann Neurol* **63**, 204–212 (2008).
7. Cho, H. *et al.* In vivo cortical spreading pattern of tau and amyloid in the Alzheimer disease spectrum. *Ann Neurol* **80**, 247–258 (2016).
8. Scholl, M. *et al.* PET imaging of tau deposition in the aging human brain. *Neuron* **89**, 971–982 (2016).
9. Ossenkoppele, R. *et al.* Tau PET patterns mirror clinical and neuroanatomical variability in Alzheimer's disease. *Brain* **139**, 1551–1567 (2016).
10. Leyns, C. E. G. & Holtzman, D. M. Glial contributions to neurodegeneration in tauopathies. *Mol Neurodegender* **12**, 50 (2017).
11. Shi, Y. *et al.* Microglia drive APOE-dependent neurodegeneration in a tauopathy mouse model. *J Exp Med* **216**, 2546–2561 (2019).
12. Benitez, A. *et al.* White matter tract integrity metrics reflect the vulnerability of late-myelinating tracts in Alzheimer's disease. *Neuroimage Clin* **4**, 64–71 (2013).

13. Dean III, D. C. *et al.* Association of amyloid pathology with myelin alteration in preclinical Alzheimer disease. *JAMA Neurol* **74**, 41–49 (2017).

14. Nasrabady, S. E., Rizvi, B., Goldman, J. E. & Brickman, A. M. White matter changes in Alzheimer's disease: a focus on myelin and oligodendrocytes. *Acta Neuro Comms* **6**, 22 (2018).

15. Desai, M. K. *et al.* Triple-transgenic Alzheimer's disease mice exhibit region-specific abnormalities in brain myelination patterns prior to appearance of amyloid and tau pathology. *Glia* **57**, 54–65 (2009).

16. Zhang, X. *et al.* Oligodendroglial glycolytic stress triggers inflammasome activation and neuropathology in Alzheimer's disease. *Sci Adv* **6**, eabb8680 (2020).

17. Shi, Y. *et al.* Overexpressing low-density lipoprotein receptor reduces tau-associated neurodegeneration in relation to apoE-linked mechanisms. *Neuron* **109**, 2413-2426.e7 (2021).

18.Cord er, E. H. *et al.* Gene dose of apolipoprotein E type 4 allele and the risk of Alzheimer's disease in late onset families. *Science* **261**, 921–923 (1993).

19. Saunders, A. M. *et al.* Association of apolipoprotein E allele ϵ4 with late-onset familial and sporadic alzheimer's disease. *Neurology* **43**, 1467–1472 (1993).

20. Lambert, J. C. *et al.* Meta-analysis of 74,046 individuals identifies 11 new susceptibility loci for Alzheimer's disease. *Nat Genet* **45**, 1452–1458 (2013).

21. Farrer, L. A. *et al.* Effects of age, sex, and ethnicity on the association between apolipoprotein E genotype and Alzheimer disease. A meta-analysis. APOE and Alzheimer Disease Meta Analysis Consortium. *JAMA* **278**, 1349–56 (1997).

22. Yamazaki, Y., Zhao, N., Caulfield, T. R., Liu, C. C. & Bu, G. Apolipoprotein E and Alzheimer disease: pathobiology and targeting strategies. *Nature Reviews Neurology* vol. 15 501–518

23. Koutsodendris, N., Nelson, M. R., Rao, A. & Huang, Y. Apolipoprotein E and Alzheimer's disease: findings, hypotheses, and potential mechanisms. *Ann Rev Pathol* **17**, 73–99 (2022).

24. Mishra, S. *et al.* Longitudinal brain imaging in preclinical Alzheimer disease: Impact of APOE ϵ4 genotype. *Brain* **141**, 1828–1839 (2018).

25. Buttini, M. *et al.* Expression of human apolipoprotein E3 or E4 in the brains of Apoe−/− mice: isoform-specific effects on neurodegeneration. *J Neurosci* **19**, 4867–4880 (1999).

26. Andrews-Zwilling, Y. *et al.* Apolipoprotein E4 causes age-and Tau-dependent impairment of GABAergic interneurons, leading to learning and memory deficits in mice. *J Neurosci* **30**, 13707–13717 (2010).

27. Zalocusky, K. A. *et al.* Neuronal apoE upregulates MHC pathways to drive selective neurodegeneration in Alzheimer's disease. *Nat Neurosci* **24**, 786–798 (2021).

28. Shi, Y. *et al.* ApoE4 markedly exacerbates tau-mediated neurodegeneration in a mouse model of tauopathy. *Nature* **549**, 523–527 (2017).

29. Therriault, J. *et al.* Association of Apolipoprotein e ϵ4 with Medial Temporal Tau Independent of Amyloid-β. *JAMA Neurol.* **77**, 470–479 (2020).

30. Baek, M. S. *et al.* Effect of APOE ε4 genotype on amyloid-β and tau accumulation in Alzheimer's disease. *Alzheimers Res. Ther.* **12**, 140 (2020).

31. Wang, C. *et al.* Gain of toxic apolipoprotein E4 effects in human iPSC-derived neurons is ameliorated by a small-molecule structure corrector. *Nat. Med.* **24**, 647–657 (2018).

32. Lin, Y.-T. *et al.* APOE4 causes widespread molecular and cellular alterations associated with Alzheimer's disease phenotypes in human iPSC-derived brain cell types. *Neuron* **98**, 1141-1154.e7 (2018).

33. Zhao, J. *et al.* APOE4 exacerbates synapse loss and neurodegeneration in Alzheimer's disease patient iPSC-derived cerebral organoids. *Nat. Commun.* **11**, 1–14 (2020).

34. Tesseur, I. *et al.* Expression of human apolipoprotein E4 in neurons causes hyperphosphorylation of protein tau in the brains of transgenic mice. *Am J Pathol* **156**, 951–964 (2000).

35. Brecht, W. J. *et al.* Neuron-specific apolipoprotein E4 proteolysis is associated with increased Tau phosphorylation in brains of transgenic mice. *J Neurosci* **24**, 2527–2534 (2004).

36. Gale, S. C. *et al.* APOε4 is associated with enhanced in vivo innate immune responses in human subjects. *J. Allergy Clin. Immunol.* **134**, 127–134 (2014).

37. Egensperger, R., Kösel, S., Von Eitzen, U. & Graeber, M. B. Microglial activation in Alzheimer disease: association with APOE genotype. *Brain Pathol* **8**, 439–447 (1998).

38. Overmyer, M. *et al.* Astrogliosis and the ApoE genotype: an immunohistochemical study of postmortem human brain tissue. *Demet Geriatr Cogn Disord* **10**, 252–257 (1999).

39. Operto, G. *et al.* Interactive effect of age and APOE-E4 allele load on white matter myelin content in cognitively normal middle-aged subjects. *Neuroimage Clin* **24**, 101983 (2019).

40. Knoferle, J. *et al.* Apolipoprotein E4 produced in GABAergic interneurons causes learning and memory deficits in mice. *J. Neurosci.* **34**, 14069–14078 (2014).

41. Wang, C. *et al.* Selective removal of astrocytic APOE4 strongly protects against tau-mediated neurodegeneration and decreases synaptic phagocytosis by microglia. *Neuron* **109**, 1657-1674.e7 (2021).

42. Huang, Y., Weisgraber, K. H., Mucke, L. & Mahley, R. W. Apolipoprotein E Diversity of Cellular Origins, Structural and Biophysical Properties, and Effects in Alzheimer's Disease. *J Mol Neurosci* **189**, 189–204 (2004).

43. Xu, Q. *et al.* Profile and regulation of apolipoprotein E (ApoE) expression in the CNS in mice with targeting of green fluorescent protein gene to the apoE locus. *J Neurosci* **26**, 4985–4994 (2006).

44. Xu, Q. *et al.* Intron-3 retention/splicing controls neuronal expression of apolipoprotein E in the CNS. *J Neurosci* **28**, 1452–9 (2008).

45. Bien-Ly, N., Gillespie, A. K., Walker, D., Yoon, S. Y. & Huang, Y. Reducing human apolipoprotein E levels attenuates age-aependent Aβ accumulation in mutant human amyloid precursor protein transgenic mice. *J Neurosci* **32**, 4803–4811 (2012).

46. Zhu, Y. *et al.* Ablation of NF1 function in neurons induces abnormal development of cerebral cortex and reactive gliosis in the brain. *Genes Dev* **15**, 859–876 (2001).

47. Rempe, D. *et al.* Synapsin I Cre transgene expression in male mice produces germline recombination in progeny. *Genesis* **44**, 44–49 (2006).

48. DeVos, S. L. *et al.* Synaptic tau seeding precedes tau pathology in human Alzheimer's disease brain. *Front. Neurosci.* **12**, 267 (2018).

49. Agarwala, R. *et al.* Database resources of the National Center for Biotechnology Information. *Nucleic Acids Res* **44**, D7–D19 (2016).

50. Howe, K. L. *et al.* Ensembl 2021. *Nucleic Acids Res* **49**, D884–D891 (2021).

51. Frankish, A. *et al.* GENCODE 2021. *Nucleic Acids Res* **49**, D916–D923 (2021).

52. Zheng, G. X. Y. *et al.* Massively parallel digital transcriptional profiling of single cells. *Nat Commun* **8**, (2017).

53. Hao, Y. *et al.* Integrated analysis of multimodal single-cell data. *Cell* **184**, 3573-3587.e29 (2021).

54. Hafemeister, C. & Satija, R. Normalization and variance stabilization of single-cell RNA-seq data using regularized negative binomial regression. *Genome Biol* **20**, 296 (2019).

55. Ahlmann-Eltze, C. & Huber, W. glmGamPoi: fitting Gamma-Poisson generalized linear models on single cell count data. *Bioinformatics* **36**, 5701–5702 (2021).

56. Wu, T. *et al.* clusterProfiler 4.0: A universal enrichment tool for interpreting omics data. *Innov. N* **2**, 100141 (2021).

57. Kanehisa, M., Sato, Y., Kawashima, M., Furumichi, M. & Tanabe, M. KEGG as a reference resource for gene and protein annotation. *Nucleic Acids Res* **44**, D457–D462 (2016).

58. Benjamini, Y. & Hochberg, Y. Controlling the False Discovery Rate: A Practical and Powerful Approach to Multiple Testing. *J R Stat Soc Ser. B Stat Methodol* **57**, 289–300 (1995).

59. Bates, D., Mächler, M., Bolker, B. M. & Walker, S. C. Fitting Linear Mixed-Effects Models Using lme4. *J Stat Soft* **67**, 1–48 (2015).

60. Yoshiyama, Y. *et al.* Synapse loss and microglial activation precede tangles in a P301S tauopathy mouse model. *Neuron* **53**, 337–351 (2007).

61. Ishihara, T. *et al.* Age-dependent emergence and progression of tauopathy in transgenic mice overexpressing the shortest human tau isoform. *Neuron* **24**, 751–762 (1999).

62. Zhang, H., Cao, Y., Ma, L., Wei, Y. & Li, H. Possible Mechanisms of Tau Spread and Toxicity in Alzheimer's Disease. *Front Cell Dev Biol* **9**, 2064 (2021).

63. Boluda, S. *et al.* Differential induction and spread of tau pathology in young PS19 tau transgenic mice following intracerebral injections of pathological tau from Alzheimer's disease or corticobasal degeneration brains. *Acta Neuropathol* **129**, 221–237 (2015).

64. Peeraer, E. *et al.* Intracerebral injection of preformed synthetic tau fibrils initiates widespread tauopathy and neuronal loss in the brains of tau transgenic mice. *Neurobiol Dis* **73**, 83–95 (2015).

65. Guo, J. L. *et al.* Unique pathological tau conformers from alzheimer's brains transmit tau pathology in nontransgenic mice. *J Exp Med* **213**, 2635–2654 (2016).

66. Kaufman, S. K. *et al.* Tau Prion Strains Dictate Patterns of Cell Pathology, Progression Rate, and Regional Vulnerability In Vivo. *Neuron* **92**, 796–812 (2016).

67. Rauch, J. N. *et al.* LRP1 is a master regulator of tau uptake and spread. *Nature* **580**, 381–385 (2020).

68. Tripathi, R. B., Rivers, L. E., Young, K. M., Jamen, F. & Richardson, W. D. NG2 glia generate new oligodendrocytes but few astrocytes in a murine experimental autoimmune encephalomyelitis model of demyelinating disease. *J Neurosci* **30**, 16383–16390 (2010).

69. Taubes, A. *et al.* Experimental and real-world evidence supporting the computational repurposing of bumetanide for APOE4-related Alzheimer's disease. *Nat Aging* **1**, 932–947 (2021).

70. Blondel, V. D., Guillaume, J. L., Lambiotte, R. & Lefebvre, E. Fast unfolding of communities in large networks. *J Stat Mech* **2008**, P10008 (2008).

71. Changes in the expression profiles of oligodendrocytes are shared in different brain pathologies. *Nat Neurosci* **25**, 845–846 (2022).

72. Minett, T. *et al.* Microglial immunophenotype in dementia with Alzheimer's pathology. *J Neuroinflammation* **13**, 135 (2016).

73. Cerutti, S. M. & Chadi, G. S100 immunoreactivity is increased in reactive astrocytes of the visual pathways following a mechanical lesion of the rat occipital cortex. *Cell Biol Int* **24**, 35–49 (2000).

74. Habib, N. *et al.* Disease-associated astrocytes in Alzheimer's disease and aging. *Nat Neurosci* **23**, 701–706 (2020).

75. Keren-Shaul, H. *et al.* A Unique Microglia Type Associated with Restricting Development of Alzheimer's Disease. *Cell* **169**, 1276-1290.e17 (2017).

76. Pandey, S. *et al.* Disease-associated oligodendrocyte responses across neurodegenerative diseases. *Cell Rep* **40**, 111189 (2022).

77. Otero-Garcia, M. *et al.* Molecular signatures underlying neurofibrillary tangle susceptibility in Alzheimer's disease. *Neuron* **110**, 2929-2948.e8 (2022).

78. Li, L., Jiang, Y., Wang, J. Z., Liu, R. & Wang, X. Tau Ubiquitination in Alzheimer's Disease. *Front Neurol* **12**, 786353 (2022).

79. Luo, W. *et al.* Roles of heat-shock protein 90 in maintaining and facilitating the neurodegenerative phenotype in tauopathies. *Proc Natl Acad Sci USA* **104**, 9511–9516 (2007).

Chapter II

APOE4-Promoted Gliosis and Degeneration are Driven by Neuronal HMGB1 Release and Ameliorated by Small Molecule Inhibition of HMGB1 in a Tauopathy Model

Abstract

Apolipoprotein E4 (*APOE4*) is the major genetic risk factor for Alzheimer's disease (AD) and is an important driver of Tau pathology, gliosis and degeneration in AD. Still, the mechanisms underlying these APOE4-driven pathological effects remain elusive. In this study, we demonstrated in a tauopathy mouse model that APOE4 promotes significantly more nucleo-cytoplasmic translocation and release of high mobility group box 1 (HMGB1) from hippocampal neurons than APOE3, which correlated with the extent of microgliosis and the severity of neurodegeneration. Intracerebral injection of recombinant HMGB1 into young APOE4-tauopathy mice induced considerable and persistent hippocampal gliosis 8 weeks after injection. Therapeutic treatment of APOE4-tauopathy mice with small molecule inhibitors of HMGB1 effectively blocked the nucleo-cytoplasmic translocation and release of HMGB1 and ameliorated the development of prominent APOE4-driven AD pathologies, including gliosis, Tau pathology, myelin deficits, and neurodegeneration. Notably, treatment of APOE3-tauopathy mice with HMGB1 inhibitors did not show significant beneficial effects on these pathological parameters. Thus, APOE4 drives Tau-mediated gliosis and degeneration by promoting neuronal HMGB1 release, and HMGB1 inhibitors represent a promising approach for treating APOE4-related AD and other tauopathies.

Introduction

Alzheimer's disease (AD) is a highly prevalent neurodegenerative disorder that involves extensive memory loss and cognitive deficits[1]. Currently, there are no viable therapeutic options to slow AD progression[2], which is likely due to an incomplete understanding of its pathogenic mechanisms. Since AD is classified as a major tauopathy disorder, one of its main pathological hallmarks is the accumulation of Tau protein aggregates within neurons[3–5]. Other important pathological hallmarks of AD include neuroinflammation and gliosis, which have recently been identified as major contributing factors to neurodegeneration[6,7].

Epidemiological and genome-wide association studies have identified apolipoprotein E4 (*APOE4*) as the strongest genetic risk factor for late-onset AD[8–10]. The human *APOE* gene exists as three common alleles, including ε2, ε3, and ε4. *APOE* ε4 is considered the most detrimental allele as it dose-dependently increases AD risk and decreases the age of disease onset[8–11]. There is considerable evidence supporting the notion that APOE4 and APOE3 have vastly different effects on numerous AD pathologies, such as Aβ fibrillization and clearance[12–14], Tau phosphorylation and aggregation[15–18], and glial dysfunction[19,20], with APOE4 worsening these pathologies relative to APOE3. In addition to these pathologies, APOE4 has also been shown to accelerate hippocampal volume loss[21] and reduce myelination[22] in human patients [21] and to increase neurodegeneration in mice with[23] or without tauopathy[24–26] relative to APOE3. Although it is unclear exactly how APOE4 induces neurodegeneration, recent studies have shown that APOE4 increases inflammation and gliosis[23,27] and indicated that gliosis is a strong driver of APOE4-related neurodegeneration[7]. Still, the underlying cellular and molecular mechanisms responsible for APOE4-induced gliosis and subsequent neurodegeneration are unknown.

High mobility group box 1 (HMGB1) is a ubiquitous nuclear protein that has been implicated in mediating pathogenic inflammatory responses in a variety of neurodegenerative disorders,

including epilepsy[28], traumatic brain injury[29], Parkinson's disease[30], and multiple sclerosis[31]. Under physiological conditions, HMGB1 is localized to the nucleus and it operates as a transcriptional regulator[32,33]. Under pathological conditions, HMGB1 translocates from the nucleus to the cytoplasm of the cell[34,35] and it is then released to act as a key neuroinflammatory cytokine that activates the immune system and promotes inflammation[36–38]. The role of HMGB1 translocation and release in AD pathogenesis is still unclear and understudied, although some studies have shown that HMGB1 release is elevated in the CSF of human AD patients[39] and that Aβ[40] and Tau[41] oligomers can induce HMGB1 translocation and release from brain cells.

While previous studies suggest a role for HMGB1 in AD, there is an evident gap in knowledge in whether HMGB1 is a key player in the mechanisms of APOE4-driven AD pathogenesis. As 60–75% of late-onset AD patients are APOE4 carriers[11,42], it is critically important to study the potential relationship between APOE4 and HMGB1 in AD pathogenesis. In the current study, we aimed to gain an in-depth understanding of the relationship between HMGB1 and APOE4 in the setting of tauopathy by [1] evaluating the differential effects of APOE4 and APOE3 on the nucleo-cytoplasmic translocation and release of HMGB1 protein; [2] elucidating the potential APOE isoform-specific connection between HMGB1 and neurodegeneration; and [3] determining the therapeutic efficacy of utilizing HMGB1 inhibitors to mitigate the development of APOE4-driven AD pathologies in a tauopathy mouse model. Ultimately, the goal of the study is to understand the role of HMGB1 in APOE4-driven AD pathogenesis and identify new therapeutic approaches combating APOE4-related AD and other tauopathies.

Materials and Methods

Study Design. The first objective of this study was to investigate the role of HMGB1 in the pathogenic mechanism of APOE4- versus APOE3-driven AD pathogenesis. We performed pathological characterization of tauopathy mice expressing human APOE4 or APOE3 using immunohistochemical analysis. The second objective of the study was to determine the therapeutic efficacy of HMGB1 inhibitors in combating the development of prominent APOE4-driven AD pathologies. We treated APOE4 and APOE3 tauopathy mice with saline or HMGB1 inhibitors and then analyzed their brain tissues by immunohistochemical analysis. Research methods and results are reported in compliance with the Animal Research: Reporting of In Vivo Experiments (ARRIVE) guidelines. Sample sizes were chosen on the basis of previous results to allow for adequate statistical power. Mice were matched for age and gender and were randomized to treatment groups. Researchers were blinded to mouse genotype and treatment to exclude the possibility of bias. For specific experiments, refer to the relevant Materials and Methods section and figure legends for outcome measures, statistical methods, and experimental procedures.

Mice. We utilized human APOE4 and APOE3 knock-in mice that were generated as previously described[43]. These APOE knock-in mice contain a LoxP-floxed APOE gene for use in other studies, although we did not utilize the conditional deletion of APOE in this study. The APOE knock-in mice were further crossbred with Tau-P301S (PS19) transgenic mice [B6;C3-Tg(Prnp-MAPT*P301S)PS19Vle/J] (The Jackson Laboratory #:008169) expressing human P301S 1N4R Tau driven by the PrP promoter[44] to generate PS19-E4 and PS19-E3. Wildtype (WT) mice [C57BL/6J] were obtained from the Jackson Laboratory. All mice were on a pure C57BL/6 genetic background and were housed in a pathogen-free barrier facility on a 12 h light cycle at 19-23ºC and 30-70% humidity. Animals were identified by ear punch under brief isoflurane anesthesia and genotyped by polymerase chain reaction (PCR) of a tail clipping. All animals otherwise received

no procedures except those reported in this study. All animal experiments were conducted in accordance with the guidelines and regulation of the National Institutes of Health, the University of California, and the Gladstone Institutes under the protocol AN176773.

For brain tissue collections, mice were deeply anesthetized with intraperitoneal injections of avertin (Henry Schein) and transcardially perfused for 1 min with 0.9% saline. Brains were either fixed as whole brains or hemi-brains, depending on the study. Right hemi-brains were drop-fixed for 48 h in 4% paraformaldehyde (16% PFA diluted in MilliQ H_2O) (Electron Microscopy Sciences), rinsed in 1X PBS (Corning) for 24 h, and cryoprotected in 30% sucrose (Sigma) for 48 h at 4ºC. The fixed hemi-brains were cut into 30 µm thick coronal sections on a freeze sliding microtome (Leica) and stored in cryoprotectant solution (30% Ethylene Glycol, 30% Glycerol, 40% 1X PBS) at -20ºC. Left hemi-brains were snap frozen on dry ice and stored at -80ºC.

Immunohistochemistry. For immunofluorescent staining, several sections from each mouse (~300 µm apart) were transferred to a 12-well plate in 1X PBS-T (PBS + 0.1% Tween-20) (Millipore Sigma) and were washed 3x5min in PBS-T to remove cryoprotectant solution. Sections were incubated for 5 min in boiling antigen retrieval buffer (Tris buffer, pH 7.6) (TEKNOVA) and washed 2x5min in PBS-T. Sections were then incubated in blocking solution (5% normal donkey serum (Jackson Labs), 0.2% Triton-X (Millipore Sigma) in 1X PBS) for 1 h at room temperature to prevent non-specific antibody binding. After blocking, sections were washed 1x5min in PBS-T and incubated in Mouse-on-Mouse (M.O.M.) Blocking Buffer (1 drop M.O.M IgG/4mL PBS-T) (Vector Labs) for 1 h at room temperature. After M.O.M. block, sections were incubated in primary antibody at 4ºC overnight after being diluted to optimal concentrations: anti-CD68 1:100 (Bio-Rad); anti-GFAP 1:800 (Millipore Sigma); anti-HMGB1 1:100 (Abcam); anti-Iba1 (rbt) 1:200 (Wako); anti-MBP 1:500 (Abcam); anti-S100β 1:200 (Abcam). Following primary antibody

incubation, sections were washed 3x5min in PBS-T and then incubated in fluorescence-labeled secondary antibodies (Abcam, Jackson Immuno, 1:1000 in PBS-T) for 1 h at room temperature protected from light after being diluted in PBS-T. Sections were then washed 2x5min in PBS-T and incubated in DAPI (1:50,000 in PBS-T) (Thermofisher) for 8 min at room temperature protected from light. Sections were then washed 2x5min in PBS-T, mounted onto microscope slides (Fisher Scientific), coverslipped with ProLong Gold mounting media (Vector Laboratories), and sealed with clear nail polish. Images were taken using an FV3000 confocal laser scanning microscope (Olympus) or Aperio VERSA slide scanning microscope (Leica) at 10X, 20X, 40X, or 60X magnifications depending on the stain. Image analyses of percent coverage area were performed using the open-source Fiji (ImageJ) software after setting a standard threshold value that is applied to all images. Researchers were also blinded to samples to exclude the possibility of bias.

For DAB (3, 3'-diaminobenzidine) staining, several sections from each mouse (~300 µm apart) were transferred to a 12-well plate in 1X PBS-T and then washed 3x5min in PBS-T to remove cryoprotectant solution. Sections were then incubated for 5 min in boiling antigen retrieval buffer (1X PBS, 0.1M sodium citrate, 0.1M citric acid) (Fisher Scientific, Fluka) and washed 2x5min in PBS-T. Next, sections were incubated for 15 min in endogenous peroxidase buffer (1X PBS, 10% methanol (Fisher Scientific) , 3% H_2O_2 (Sigma) and washed 3x5min in PBS-T. Sections were then incubated in blocking solution (1X PBS-T, 5% normal donkey serum, 1% non-fat dry milk) for 1 h at room temperature. After blocking, sections were washed 2x5min in PBS-T and then incubated in Avidin/Biotin blockage (4 drops of each block) (Vector Laboratories) for 15 min and then washed 2x5min in PBS-T. Sections were incubated in M.O.M. Blocking Buffer (1 drop M.O.M IgG/4mL PBS-T) (Vector Labs) for 1 h at room temperature. Following M.O.M. block, sections were washed 2x5min and incubated in primary antibody at 4ºC overnight after being diluted in PBS-T to optimal concentrations (anti-pTau (AT8) 1:100 (Invitrogen). After primary antibody incubation, sections

were washed 3x5min in PBS-T and then incubated in biotinylated secondary antibody (1:200; Jackson Immuno) at room temperature for 1 h. Next, sections were washed 3x5min in PBS-T and incubated in ABC buffer (Vector Laboratories) that was prepared 10 min prior to the incubation step. Sections were washed for 2x5min in PBS-T and 1x5min in Tris buffer (pH 7.6). Sections were incubated in DAB buffer (5mL 1X PBS, 2 drops Buffer Stock Solution, 2 drops DAB, 2 drops H_2O_2) (Vector Laboratories) for precisely 2 minutes. Staining was halted by washing sections 3x5min in Tris buffer (pH 7.6) and 2x5min in PBS-T. Sections were mounted onto microscope slides and dried at room temperature overnight. Next, mounted sections were submerged into Xylene (Fisher Scientific) 2x5min and coverslipped with DPX mounting media (Sigma-Aldrich). Images were taken using an Aperio VERSA slide scanning microscope (Leica) at 10X magnification.

Volumetric analysis. Serial coronal hippocampal brain sections (7 sections per mouse, 30 µm thick, 300 µm apart) were mounted onto microscope slides (Fisher Scientific) and dried at room temperature for 1 h. The 0.1% Sudan Black solution was prepared by adding the appropriate amount of Sudan Black powder (Sigma) to 70% ethanol (KOPTEC) and mixing the solution using a magnetic stirrer while and protected from light. The solution was then centrifuged at 3,000 RPM for 10 min and the collected supernatant was filtered using a 0.2 µm filter syringe (Thermo Scientific) to remove undissolved dye. Sections were then stained with the 0.1% Sudan Black solution at room temperature for 10 min and washed 3x2min in 70% ethanol and 3x5min in Milli-Q water. Sections were then coverslipped with ProLong Gold mounting media (Invitrogen) and imaged on an Aperio VERSA slide scanning microscope (Leica) at 10X magnification. For hippocampal and posterior lateral ventricle volumetric analyses, the areas of interest were traced in ImageJ using the segmented line tool and the volume was calculated using the formula: volume = (sum of area) * 0.3 mm^{23}. The sum of area value was obtained by taking a sum of the quantified

area measurements of all 7 brain sections per mouse, roughly between coordinates AP=-1.2 and AP=-3.4.

Nuclear-cytoplasmic localization of HMGB1 measurements. Two brain sections (30 µm thick, 300 µm apart) were immunostained with anti-HMGB1 (1:100) and DAPI (1:50,000) as described above. Sections were imaged at 60X magnification with or without 3X Zoom using an FV3000 confocal laser scanning microscope (Olympus). All image processing and quantification was performed on the Fiji (ImageJ) software. Briefly, a 1-pixel median filter was applied to the DAPI channel and an appropriate threshold was set to create a mask of DAPI. The image calculator function was then used to overlay the DAPI mask and HMGB1 channel, which provided the HMGB1 staining that was only localized to the nucleus. After obtaining values for integrated density and particles, the image calculator was used to subtract the DAPI mask from HMGB1, which provided HMGB1 staining that was excluded from the nucleus.

Sandwich ELISA. Biochemically extracted mouse hippocampal tissue lysates were diluted in Milli-Q H_2O to the appropriate concentration and were run according to the provided manufacturer protocols (mouse HMGB1; (Novus Biologicals). Reactions of samples were read on a SpectraMaX M5 spectrophotometer (Molecular Devices) and protein concentrations were determined after interpolating a standard curve and adjusting for dilutions.

Stereotaxic surgery on mice. Mice were anesthetized with an intraperitoneal injection of ketamine (60 mg/kg) and xylazine (30 mg/kg) and maintained on 0.8%-1.0% isofluorane (Henry Schein). Mice were secured in a stereotaxic alignment system model 940 using earbars and a tooth bar (Kopf Instruments). The scalp was prepared by removing hair using Nair and sterilizing with 70% ethanol. The scalp was then cut open using a scalpel and sterilized with 70% ethanol. The cranial sutures were better visualized using 3% hydrogen peroxide. Following identification

of Bregma, a unilateral stereotaxic site was drilled with a 0.5 mm microburr (Fine Science Tools) using coordinates X = +1.5, Y = -2.1, Z = -2.1, with Z measured from the surface of the brain. Mice were injected with 2μL of the ISF fraction, recombinant HMGB1, or saline at a rate of 500 nL/min and allowed to diffuse for 3 min. Following surgery, mice were sutured with nylon monofilament non-absorbable 6-0 sutures (Henry Schein), and administered analgesics buprenorphine (0.0375 mg/kg intraperitoneally), ketophen (5 mg/kg subcutaneously), and saline (500μL intraperitoneally). Mice were monitored on a heating pad until ambulatory and provided Hydrogel for hydration.

Microdialysis of mouse hippocampus. Brain interstitial fluid was collected using *in vivo* microdialysis of the hippocampus. Surgical procedures, including pre- and post-operative care, were conducted as described above for stereotaxic surgeries. During the surgery, a unilateral stereotaxic site was drilled with a 1.2mm bone drill bit (BASi) and an AtmosLM guide cannula PEG-4 (Amuza) was stereotaxically implanted above the right hippocampus at coordinates X = +1.5, Y = -2.1, Z = -1.1. The cannula was secured in place using dental cement (GC America), and a temporary PEG-4 AtmosLM dummy probe (Amuza) was inserted and fixed with an AC-5 cap nut screw (Eicom). Two days post-surgery, mice were placed in a microdialysis stand-alone system (BASi) overnight to assimilate, and the following afternoon a 1000kDa AtmosLM collection probe (Eicom) was inserted through the guide cannula into the hippocampus, which extends 1mm father down to Z = -2.1 to target the dentate gyrus. Artificial CSF (Harvard Apparatus) made with 0.15% BSA (Thermo Scientific) was circulated through the system at a rate of 0.5 μL/min using a push-pull method, and ISF was collected in a refrigerated fraction collector (BASI) each hour for roughly 24 hours. To prevent clogging of the tubing, pumps were operated at 10X collection speed for the first two hours before being adjusted to a 0.5 μL/min flow rate. Following completion of ISF collection, mice were euthanized and perfused with 0.9% saline, as described above. The brain

was dissected into hemispheres, with the right hemi-brain postfixed for 48 hours in 4% PFA and the left hemi-brain fresh frozen. ISF fractions were frozen at -80ºC for further analysis.

Treatment with HMGB1 inhibitors. At 6.5 months of age, male and female PS19-E4 and PS19-E3 mice were randomly assigned to the control or treatment group. Mice received intraperitoneal injections with either sterile grade 0.9% saline (Fisher Scientific) or a mixture of HMGB1 inhibitors: ethyl pyruvate (80mg/kg) (Sigma-Aldrich) and glycyrrhizic acid (20mg/kg) (Sigma-Aldrich) dissolved in 0.9% saline. The mice received three injections per week for 12 weeks, starting at 6.5 months of age until they reached 9.5 months of age. All mice were monitored for weight changes, grooming changes, and posture during the experiments and no changes were observed. Following treatment, the animals were perfused and their brain tissue was processed for histopathological analysis, as described above.

General statistical analysis. All plotted data are presented as the mean ± SEM, unless otherwise specified. Data were analyzed using unpaired two-sided t test and ordinary one-way analysis of variance (ANOVA) followed by Tukey's multiple comparisons test. We utilized two-sided tests and all analyzed data met the assumption for the specific statistical test that was performed. The correlations between two data in the same genotype group were analyzed using simple linear regression and plotted as the mean ± SEM. Probability levels of $P < 0.05$ were considered statistically significant. The analyses were performed and plots were created with GraphPad Prism version 9.2.0.

Acknowledgments: We thank Huang lab staff for their valuable discussions about the experimental design as well as data analyses and interpretation. We also thank **Theodora Pak for editorial assistance.**

Author Contributions: N.K. and Y.Huang. designed and coordinated the studies and wrote the manuscript. N.K. performed the majority of studies and data analyses. J.B. conducted the microdialysis surgeries and ISF collection and helped on some immunohistochemical studies and data collection. A.A., M.T, B.G, Y.Hao, R.T. and M.Z. performed some of the data analyses. O.Y., A.R., and M.R.N. helped on some immunohistochemical studies and data collection. A.R. also helped on some of the HMGB1 inhibitor injections. S.Y.Y. and P.A. managed all mouse lines, helped on mouse brain collection, and performed some of the HMGB1 inhibitor injections. Y.H. supervised the project.

Funding: This work was partially supported by the National Institutes of Health grants R01AG071697 and P01AG073082 to Y.Huang, F31AG074672 to N.K., and F31AG074690 to M.N.

Competing interests: Y.H. is a co-founder and scientific advisory board member of E-Scape Bio, Inc. and GABAeron, Inc. Other authors declare no competing financial interests.

Data and materials availability: All data associated with this study and the information of used materials are available in the main text, the Materials and Methods, or the Supplementary Information section.

Results

APOE4 exacerbates degeneration and gliosis in a mouse model of tauopathy

In order to investigate the relationship between APOE4 and HMGB1 in the setting of tauopathy, we utilized a humanized APOE and Tau-P301S compound mouse model. This mouse model expresses a homozygous human *APOE4* or *APOE3* gene knocked in place of the endogenous mouse *Apoe* locus, as was previously generated in our lab[43]. The APOE knock-in mouse line was crossbred with a widely utilized tauopathy mouse model (PS19 line) that express P301S mutant human microtubule-associated protein Tau (*MAPT)*[44].

We first performed an in-depth characterization of the pathological differences between 10-month-old PS19-E4 and PS19-E3 mice. The PS19-E4 mice displayed extensive neurodegeneration relative to PS19-E3 mice, as they had a significant decrease in hippocampal volume and increase in posterior lateral ventricle volume (**Fig. 2.1A-C**). PS19-E4 mice also had more pronounced Tau pathology relative to PS19-E3 mice, as determined by measuring the area coverage of $AT8^+$ phosphorylated Tau (pTau) within the hippocampus (**Fig. 2.1D,E**). To further validate the differences in pathological Tau between genotypes, we performed sequential biochemical extraction of mouse hippocampal tissue lysates to separate highly soluble Tau proteins in the RAB buffer fraction and less soluble Tau proteins in the RIPA buffer fraction. Analysis of myelin basic protein (MBP) in the stratum radiatum of CA1 showed that APOE4 led to significant myelin deficits relative to APOE3, as PS19-E4 mice had a low coverage area of MBP relative to PS19-E3 mice (**Fig. 2.1F,G**).

Assessment of glial cells revealed that PS19-E4 mice had significantly higher hippocampal coverage areas of $Iba1^+$ microglia (**Fig. 2.1H,I**) and $GFAP^+$ astrocytes (**Fig. 2.1J,K**). This suggests that APOE4 promotes both microgliosis and astrogliosis in the hippocampus in this mouse model

of tauopathy. Strikingly, there was a strong negative correlation between the coverage area of Iba1$^+$ microglia (**Fig. 2.1L**) and hippocampal volume in PS19-E4 mice. Notably, there was a weak, but significant, negative correlation between the coverage area of GFAP$^+$ astrocytes (**Fig. 2.1M**) and hippocampal volume in PS19-E4 mice. This indicates that the extent of microgliosis and neurodegeneration are tightly related to one another and suggests that microgliosis is a better indicator and/or contributor to neurodegeneration than astrogliosis. Taken together, this detailed pathological characterization shows that APOE4 has wide-ranging detrimental effects that exacerbate various AD-related pathologies, including neurodegeneration, Tau pathology, myelin deficits, and gliosis, and is complementary to what has been previously reported[23,45,46].

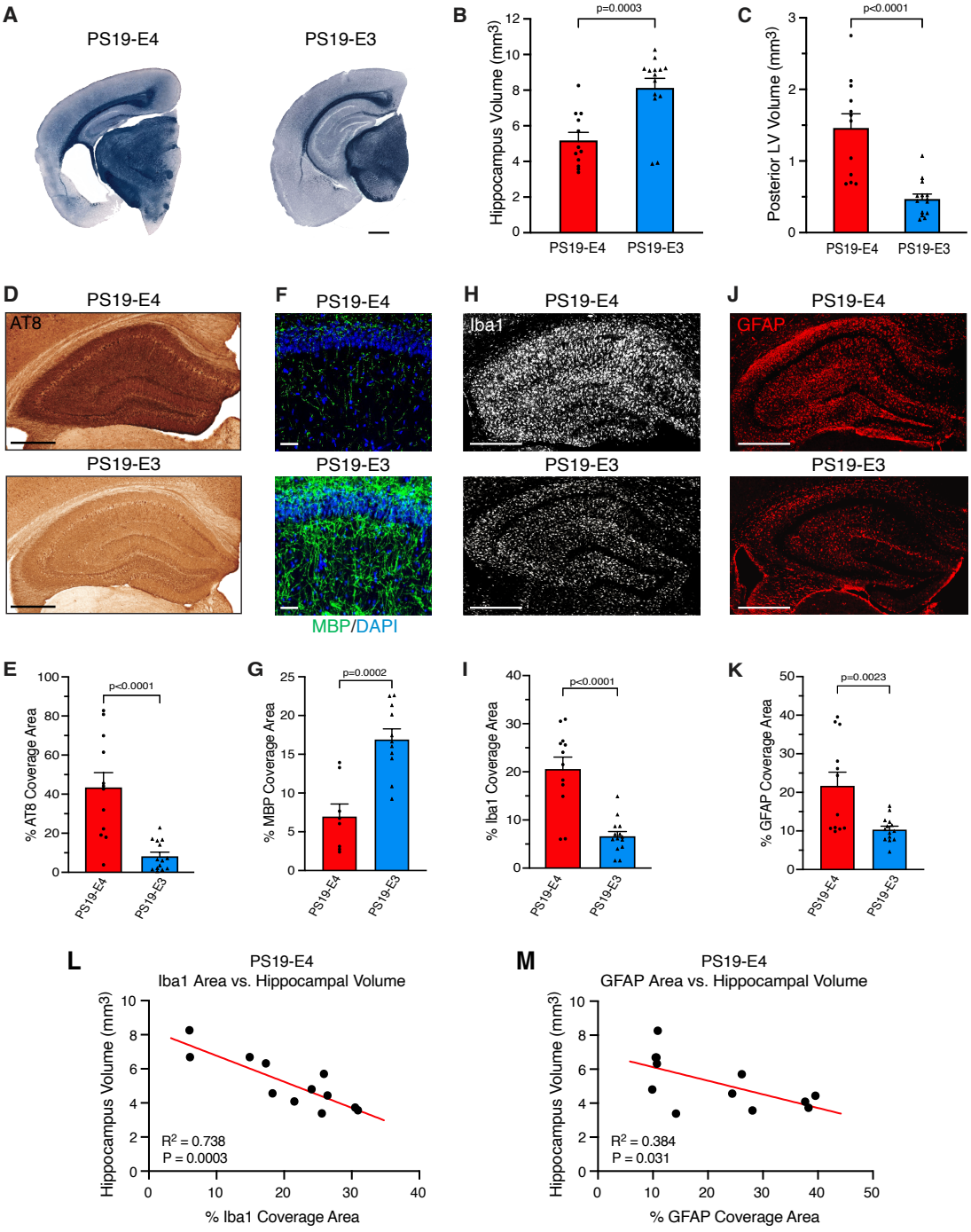

Figure 2.1. APOE4 increases neurodegeneration, Tau pathology, myelin deficits, and gliosis relative to APOE3 in a mouse model of tauopathy. A, Representative images of the ventral hippocampus after staining with Sudan Black (scale bar, 1 mm). **B,C**, Quantification of hippocampal volume (B) and posterior lateral ventricle volume (C). **D,** Representative images of pTau staining with anti-AT8 in the hippocampus (scale bar, 500 μm). **E**, Quantification of the percent pTau (AT8) coverage area in the hippocampus. **F**, Representative images of myelin basic protein (MBP) immunostaining with anti-MBP in the stratum radiatum of the hippocampus underneath the pyramidal cell layer of CA1 (scale bar, 50 μm). **G**, Quantification of the percent

MBP coverage area in the stratum radiatum of the hippocampus. **H**, Representative images of microglia immunostaining with anti-Iba1 in the hippocampus (scale bar, 500 μm). **I**, Quantification of the percent Iba1 coverage area in the hippocampus. **J**, Representative images of astrocyte immunostaining with anti-GFAP in the hippocampus (scale bar, 500 μm). **K**, Quantification of percent GFAP coverage area in the hippocampus. **L,** Correlation between percent Iba1 coverage area and hippocampal volume in PS19-E4 mice. **M,** Correlation between GFAP coverage area and hippocampal volume of PS19-E4 mice. For all representative images and quantified data, mice were 10-months-old and belonged to either the PS19-E4 or PS19-E3 genotype groups. Quantified data in B,C,E,I,K (PS19-E4, n=12; PS19-E3, n=14) and G (PS19-E4, n=8, PS19-E3, n=11) are represented as mean±SEM, unpaired two-sided t test. Data in L,M (PS19-E4, n=12) are Pearson's correlation analysis (two-sided).

APOE4 promotes the nucleo-cytoplasmic translocation of HMGB1 in hippocampal neurons

The HMGB1 protein is a nuclear protein that is widely recognized as a critical factor for glial cell activation[35]. Under pathological conditions, HMGB1 translocates from the nucleus to the cytoplasm of stressed or dying cells and it is then released to act as a proinflammatory cytokine to activate glial cells[32,34,37]. Since gliosis is the earliest pathological manifestation in the PS19 tauopathy mouse model[44] and we illustrate that APOE4 promotes gliosis in this same mouse model (**Fig. 2.1H–1K**), we investigated if APOE4 affects the nucleo-cytoplasmic translocation of HMGB1 that can trigger glial response. Immunohistochemical staining for HMGB1 protein and the nuclear marker DAPI in 10-month-old mice showed that PS19-E4 mice had a remarkably high amount of nucleo-cytoplasmic translocation of HMGB1 protein, as a significant majority of the protein can be found located outside of the nucleus of hippocampal neurons (**Fig. 2.2A-D**). On the other hand, HMGB1 protein in PS19-E3 mice was largely retained within the nucleus and there was minimal translocation outside of the nucleus relative to PS19-E4 mice (**Fig. 2.2A-D**). Further analysis showed that PS19-E4 mice also contained a greater number of HMGB1-positive puncta both within the nucleus and outside of the nucleus relative to PS19-E3 mice (**Fig. 2.2A, B, E and F**).

Importantly, when comparing the relative amount of extranuclear HMGB1 protein with the hippocampal volume of PS19-E4 mice, we observed a negative correlation between these two pathologies (**Fig. 2.2G**). There was also a positive correlation between the relative amount of extranuclear HMGB1 protein and the coverage area of $Iba1^+$ microglia (**Fig. 2.2H**) in PS19-E4 mice. This indicates that higher amounts of extranuclear HMGB1 protein correlates with lower hippocampal volume and higher levels of microgliosis. These correlation analyses reveal an intriguing relationship between the extent of intraneuronal HMGB1 translocation and the severity of neurodegeneration and microgliosis in the presence of APOE4, suggesting that HMGB1 plays

an important role in the pathogenic mechanism of APOE4-driven gliosis and neurodegeneration in the context of tauopathy.

To investigate whether APOE4 is able to promote the translocation of HMGB1 in the absence of mutant Tau, we analyzed human E4 and E3 knock-in mice that lacked human mutant Tau-P301S and instead contained the endogenous mouse MAPT. Immunostaining for HMGB1 protein showed that it remained localized within the nucleus in both E4 and E3 mice (**Fig. 2.3A-F**), illustrating that the nucleo-cytoplasmic translocation of HMGB1 requires the coexistence of both APOE4 and tauopathy, as illustrated in the PS19-E4 mice (**Fig. 2.2A-2F**). These data provide evidence that APOE4 strongly promotes HMGB1 nucleo-cytoplasmic translocation in the context of tauopathy, whereas APOE3 does not significantly affect HMGB1 translocation.

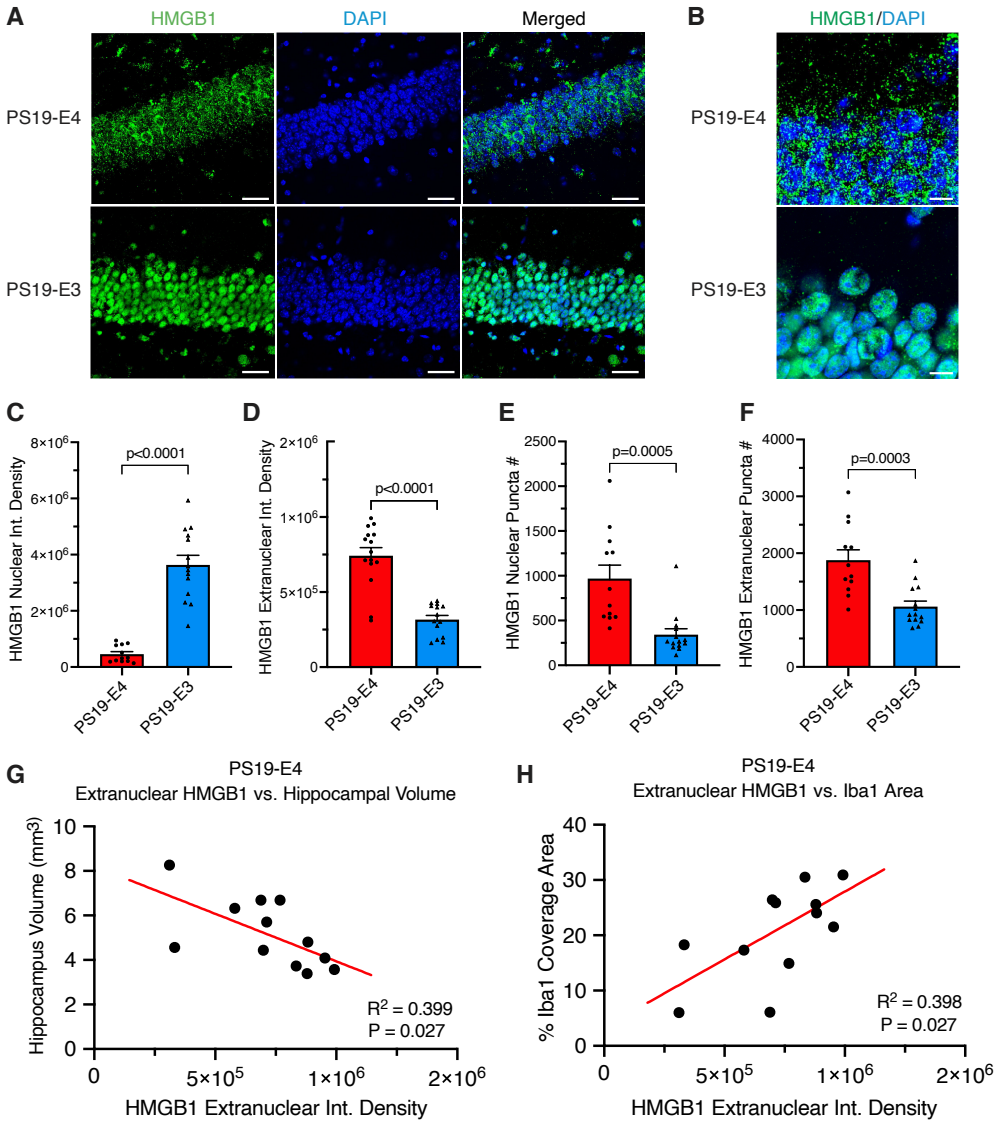

Figure 2.2. APOE4 promotes the nucleo-cytoplasmic translocation of HMGB1 in hippocampal neurons, which correlates with microgliosis and neurodegeneration. A, Representative images of immunostaining with anti-HMGB1 and DAPI in the dentate gyrus of the hippocampus (scale bar, 40 µm). **B**, Representative high magnification images of immunostaining with anti-HMGB1 and DAPI in the dentate gyrus (scale bar, 10 µm). **C**, Quantification of nuclear integrated density of HMGB1 immunostaining in hippocampal neurons. **D**, Quantification of extranuclear integrated density of HMGB1 immunostaining in hippocampal neurons. **E**, Quantification of the number of nuclear HMGB1^{+} puncta in hippocampal neurons. **F**, Quantification of the number of extranuclear HMGB1^{+} puncta in hippocampal neurons. **G,** Correlation between HMGB1 extranuclear integrated density and hippocampal volume in PS19-E4 mice. **H,** Correlation between HMGB1 extranuclear integrated density and the percent Iba1 coverage area in PS19-E4 mice. For all representative images and quantified data, mice were 10-months-old and belonged to either the PS19-E4 or PS19-E3 genotype groups. Quantified data in C,D,E,F (PS19-E4, n=12; PS19-E3, n=14) are represented as mean±SEM, unpaired two-sided t test. Data in G,H (PS19-E4, n=12) are Pearson's correlation analysis (two-sided).

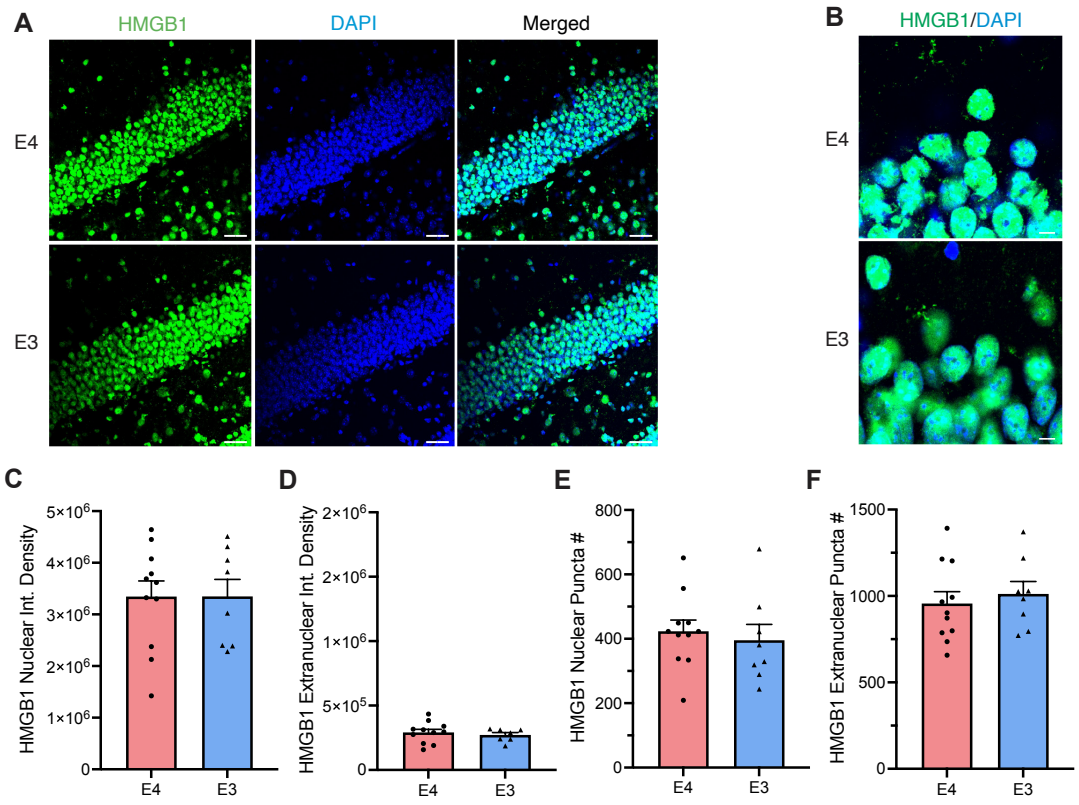

Figure 2.3 APOE4 does not induce the nucleo-cytoplasmic translocation of HMGB1 in hippocampal neurons in mice without tauopathy. **A**, Representative images of immunostaining with anti-HMGB1 and DAPI in the dentate gyrus of 10-month-old E4 and E3 mice (scale bar, 40 μm). **B**, Representative high magnification images of immunostaining with anti-HMGB1 and DAPI in the dentate gyrus of 10-month-old E4 and E3 mice that do not contain P301S mutant Tau (scale bar, 10 μm). **C**, Quantification of nuclear integrated density of HMGB1 immunostaining in hippocampal neurons. **D**, Quantification of extranuclear integrated density of HMGB1 immunostaining in hippocampal neurons. **E**, Quantification of the number of nuclear $HMGB1^+$ puncta in hippocampal neurons. **F**, Quantification of the number of extranuclear $HMGB1^+$ puncta in hippocampal neurons. For all representative images and quantified data, mice were 10-months-old and belonged to either the E4 or E3 genotype groups. Quantified data in C,D,E,F (E4, n=11; E3, n=8) are represented as mean±SEM, unpaired two-sided t test.

APOE4-driven release of HMGB1 induces acute and persistent gliosis in the hippocampus

To further evaluate the differential effects of APOE4 and APOE3 on the cellular release of HMGB1 protein, we collected the hippocampal interstitial fluid (ISF) from 10-month-old PS19-E4 and PS19-E3 mice over a 24-hour period using *in vivo* microdialysis[47]. We quantitatively determined the levels of extracellular HMGB1 protein in the ISF using sandwich ELISA. Strikingly, PS19-E4 mice exhibited high levels of HMGB1 protein within their hippocampal ISF while PS19-E3 mice had undetectable levels of HMGB1 protein in their ISF (**Fig. 2.4A,B**). This indicates that APOE4 plays a critical role in promoting the cellular release of HMGB1.

It has been reported that, following its cellular release, HMGB1 can act as a neuroinflammatory cytokine that induces gliosis[37,48]. To determine the importance of released HMGB1 in triggering gliosis in APOE4-related tauopathies, we injected the collected hippocampal ISF from a 10-month-old PS19-E4 mouse into the hippocampi of 10-month-old wildtype mice, which do not typically display hippocampal gliosis. The injected ISF fractions were either enriched with relatively high concentrations of HMGB1 protein (fractions 19–22 in **Fig. 2.4C**) or had undetectable levels of HMGB1 protein as a control (fractions 3–7 in **Fig. 2.4C**), as determined by sandwich ELISA. The wildtype mice received a unilateral injection into the right dorsal hippocampus of either HMGB1-enriched ($HMGB1^+$) or control ($HMGB1^-$) ISF and were analyzed 6 days post-injection to assess acute changes in glial response in the hippocampus (**Fig. 2.4D**).

Wildtype mice that were injected with the control ($HMGB1^-$) ISF exhibited relatively low coverage areas of $Iba1^+$ microglia and $GFAP^+$ astrocytes on both the injected and non-injected hippocampal sides, indicating that the majority of glial response induced by the injection surgery itself subsided following the 6-day recovery period post-injection (**Fig. 2.4F-I**). On the contrary, wildtype mice injected with the $HMGB1^+$ ISF displayed a significant increase in the coverage area of microglia

on the injected hippocampal side relative to the non-injected side (**Fig. 2.4F,G**). Interestingly, injection of $HMGB1^{+}$ ISF led to a minor, but insignificant, increase in the coverage area of astrocytes in the injected hippocampal side relative to the non-injected side (**Fig. 2.4H,I**). This suggests that the presence of extracellular HMGB1 leads to a strong acute recruitment/activation of microglia, while only showing a weak increase in the amount of acute astrogliosis.

To further validate the ability of HMGB1 to induce gliosis in the context of APOE4, we injected recombinant HMGB1 (rHMGB1) or saline directly into the hippocampus of young 3-month-old PS19-E4 mice (**Fig. 2.4E**). These mice received a second injection of rHMGB1 or saline 2-weeks after the initial injection to mimic the repeated cellular release of HMGB1. Immunohistochemical analysis of the injected PS19-E4 mice 8-weeks after the initial injection at 5-months-of-age showed that injection with rHMGB1 led to a significant increase in the extent of microgliosis and astrogliosis compared to the saline control (**Fig. 2.4J-M**). This illustrates that HMGB1 is able to induce early and persistent gliosis in young PS19-E4 mice even several weeks after its injection. Taken together, these data suggest that the release of HMGB1 from hippocampal cells represents a novel mechanism by which APOE4 promotes gliosis in the context of tauopathy. Taken together, these data suggest that the release of HMGB1 from hippocampal cells represents a novel mechanism by which APOE4 promotes gliosis in the context of tauopathy.

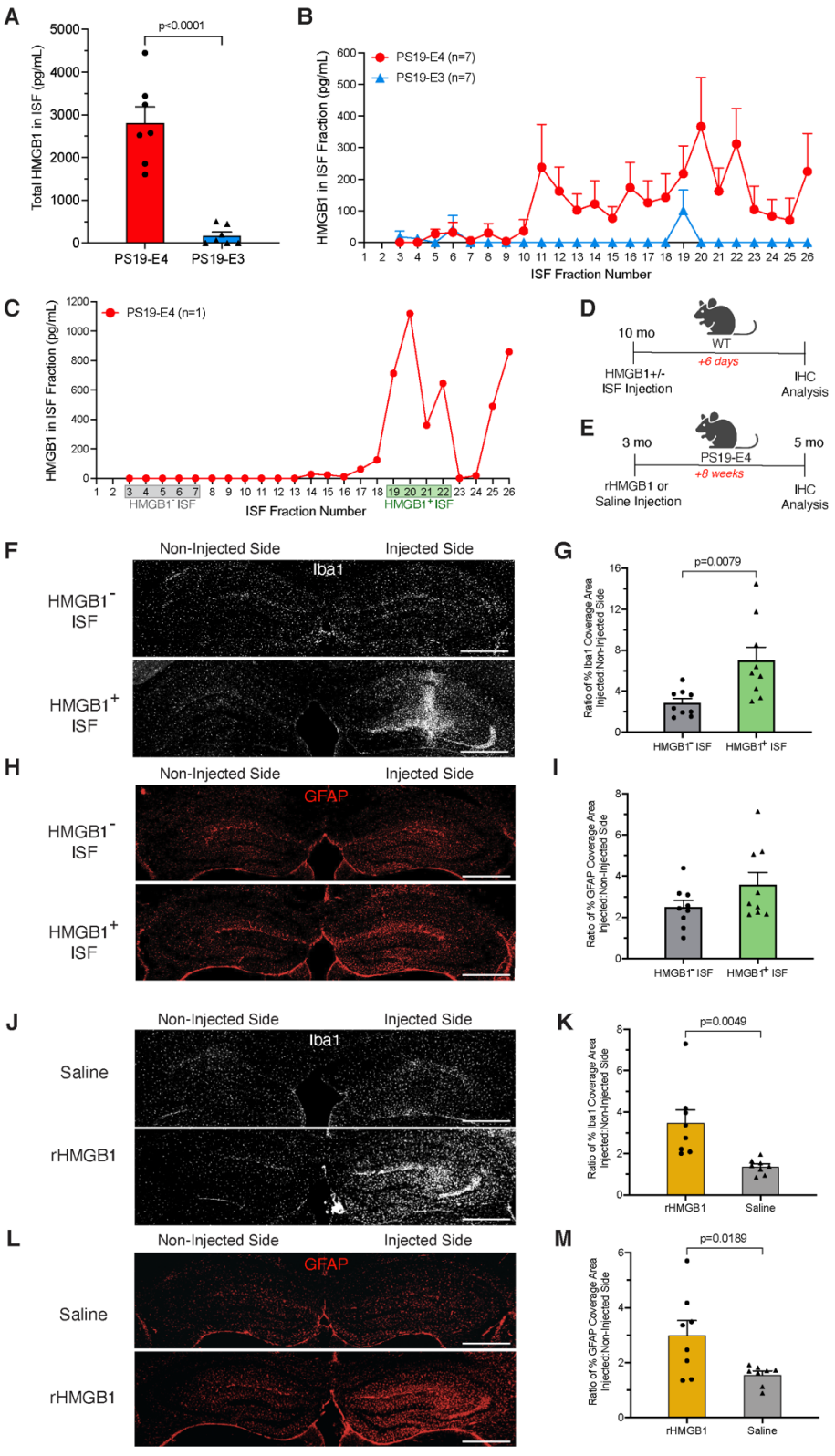

Figure 2.4. APOE4 induces the cellular release of HMGB1 to stimulate gliosis. A, Total extracellular HMGB1 protein levels measured by ELISA in the hippocampal ISF of 10-month-old PS19-E4 and PS19-E3 mice. **B**, Extracellular HMGB1 protein levels measured by ELISA in each

collected ISF fraction of 10-month-old PS19-E4 mice. Fractions 1-2 were excluded from analyses in A,B since artificial CSF was circulated at a higher flow rate for the first two hours to prevent clogging of the tubing. **C**, Extracellular HMGB1 protein levels measured by ELISA in each collected ISF fraction of one PS19-E4 mouse used for experiments in D, F-I. Fractions 3-7 were designated as HMGB1-absent fractions and fractions 19-22 were designated as HMGB1-enriched fractions. **D**, Experimental design of a study involving the injection of HMGB1-enriched or HMGB1-absent ISF into the hippocampus of 10-month-old WT mice and assessment of acute gliosis 6 days after the initial injection. **E**, Experimental design of a study involving the injection of rHMGB1 or saline into the hippocampus of 3-month-old PS19-E4 mice and assessment of gliosis 8-weeks after the initial injection. **F**, Representative images of microglia stained with anti-Iba1 in the hippocampus of 10-month-old WT mice following a unilateral injection of HMGB1-absent ($HMGB1^-$) or HMGB1-enriched ($HMGB1^+$) ISF collected from a PS19-E4 mouse (scale bar, 500 μm). **G**, Quantification of the ratio of percent Iba1 coverage area between the injected and non-injected hippocampal sides 6 days post-injection. **H**, Representative images of astrocytes stained with anti-GFAP in the hippocampus of 10-month-old wildtype mice following a unilateral injection of injection of HMGB1-absent or HMGB1-enriched ISF collected from a PS19-E4 mouse (scale bar, 500 μm). **I**, Quantification of the ratio of percent GFAP coverage area between the injected and non-injected hippocampal sides 6 days post-injection. **J**, Representative images of microglia stained with anti-Iba1 in the hippocampus of 5-month-old PS19-E4 mice following a unilateral injection of rHMGB1 or saline (scale bar, 500 μm). **K**, Quantification of the ratio of percent Iba1 coverage area between the injected and non-injected hippocampal sides 8-weeks after the initial injection. **L**, Representative images of astrocytes stained with anti-GFAP in the hippocampus of 3-month-old PS19-E4 mice following a unilateral injection of rHMGB1 or saline (scale bar, 500 μm). **I**, Quantification of the ratio of percent GFAP coverage area between the injected and non-injected hippocampal sides 8-weeks after the initial injection. Data in A,B include n=7 mice per genotype. For quantifications in G,I, n=9 mice were used for control ($HMGB1^-$) and experimental ($HMGB1^+$) groups. For quantifications in K,M, n=8 mice were used for rHMGB1 and saline control groups. All data are represented as mean±SEM, unpaired two-sided t test. ISF, interstitial fluid; WT, wildtype; rHMGB1, recombinant HMGB1.

Mechanisms of HMGB1 translocation and release

While APOE is produced by several cell types in the central nervous system, previous studies from our lab have indicated that neuronal APOE4 exerts detrimental effects that promote increased p-Tau[16] and AβI levels[15], inhibitory neuronal loss, and learning and memory deficits[49]. To understand if neuronal APOE4 plays a role in promoting the HMGB1 translocation and release observed in PS19-E4 mice, we utilized a PS19-E4 mouse model that contains a floxed human APOE gene and has Cre recombinase driven under a neuron-specific Syn1 promoter (PS19-fE4/Syn1-Cre mice). These mice have APOE4 selectively removed from neurons. Immunohistochemical staining of HMGB1 protein in 10-month-old PS19-fE4/Syn1-Cre mice reveals that there is minimal HMGB1 translocation after neuronal APOE4 removal, with the majority of HMGB1 remaining localized in the nucleus (**Fig. 2.5A-D**). We also observed a significant decrease in the number of HMGB1 puncta in the nucleus and outside the nucleus (**Fig. 2.5A-D**).

We also determined the effect of neuronal APOE4 on the cellular release of HMGB1 by performing *in vivo* microdialysis to collect the hippocampal interstitial fluid from 10-month-old PS19-fE4/Syn1-Cre mice. Quantitation of HMGB1 levels via ELISA showed that the removal of neuronal APOE4 eliminates the release of HMGB1 protein into the ISF, as there were no detectable levels of HMGB1 protein in the ISF of PS19-fE4/Syn1-Cre mice (**Fig. 2.5G,H**). Taken together, these data indicate that the expression of APOE4 in neurons is a strong driver of HMGB1 translocation and release.

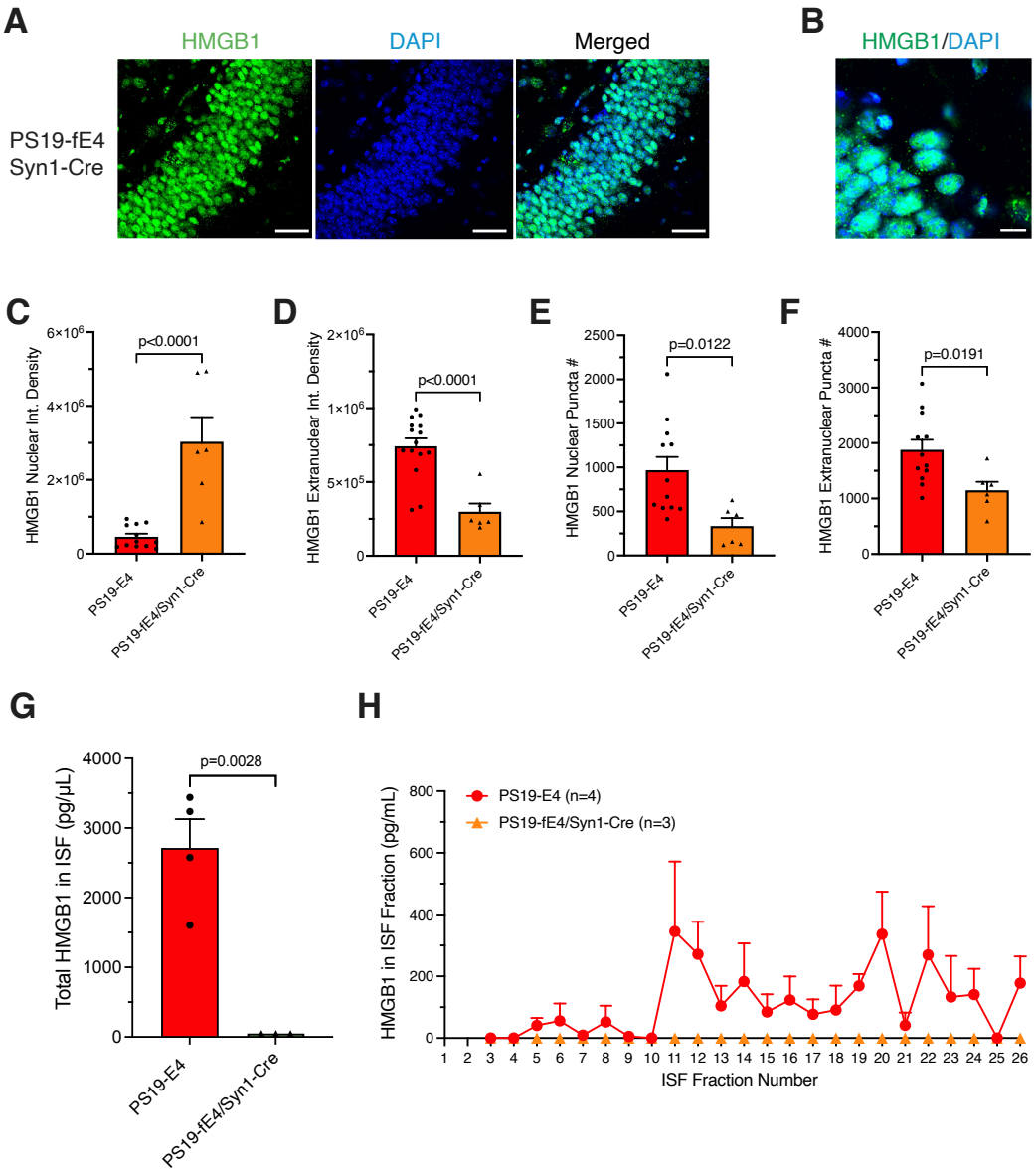

Figure 2.5. Removal of neuronal APOE4 blocks the nucleo-cytoplasmic translocation and release of HMGB1 in hippocampal neurons. A, Representative images of immunostaining with anti-HMGB1 and DAPI in the dentate gyrus of the hippocampus of PS19-fE4/Syn1-Cre mice (scale bar, 40 μm). **B**, Representative high magnification images of immunostaining with anti-HMGB1 and DAPI in the dentate gyrus (scale bar, 10 μm). **C**, Quantification of nuclear integrated density of HMGB1 immunostaining in hippocampal neurons. **D**, Quantification of extranuclear integrated density of HMGB1 immunostaining in hippocampal neurons. **E**, Quantification of the number of nuclear HMGB1^{+} puncta in hippocampal neurons. **F**, Quantification of the number of extranuclear HMGB1^{+} puncta in hippocampal neurons. **G**, Total extracellular HMGB1 protein levels measured by ELISA in the hippocampal interstitial fluid (ISF) of 10-month-old PS19-E4 and PS19-fE4/Syn1-Cre mice. **H**, Extracellular HMGB1 protein levels measured by ELISA in each collected ISF fraction of 10-month-old PS19-E4 and PS19-fE4/Syn1-Cre mice. Fractions 1-2 were excluded from analyses in G,H. Quantified data in C,D,E,F (PS19-E4, n=12; PS19-fE4/Syn1-Cre, n=6) and G,H (PS19-E4, n=4; PS19-fE4/Syn1-Cre, n=3) are represented as mean±SEM, unpaired two-sided t test.

Treatment with HMGB1 inhibitors blocks APOE4-driven HMGB1 translocation in hippocampal neurons

Based on our findings that APOE4 is a potent driver of HMGB1 translocation and release from neurons, we sought to test the therapeutic efficacy of HMGB1 inhibitors in combating APOE4-driven AD pathogenesis in the context of tauopathy. To this end, we utilized two well-characterized HMGB1 inhibitors, ethyl pyruvate (EP) and glycyrrhizic acid (GA), which are selective inhibitors of HMGB1 translocation and release[50–53]. We administered a mixed solution of EP (80 mg/kg) and GA (20 mg/kg) or saline vehicle to PS19-E4 and PS19-E3 mice at three doses per week for 12 weeks via intraperitoneal injections (**Fig. 2.6A**). Treatment began when the mice were 6.5 months of age, at about the onset of adverse pathology, and completed when the mice were 9.5 months of age, when severe neurodegeneration and pathological changes are present, as demonstrated in this and another study[44]. All mice were monitored for weight changes during the treatment period and no changes were observed.

We first confirmed the effectiveness of EP and GA at blocking HMGB1 protein nucleo-cytoplasmic translocation in hippocampal neurons by immunostaining with anti-HMGB1 and DAPI. Saline-treated PS19-E4 mice exhibited extensive translocation of HMGB1 protein out of the nucleus, whereas PS19-E4 mice treated with the HMGB1 inhibitors had the majority of HMGB1 protein retained within the nucleus (**Fig. 2.6B-D**). In PS19-E3 mice, there was no significant difference in HMGB1 translocation between saline- and inhibitor-treated groups (**Fig. 2.6B-D**). Thus, HMGB1 inhibitors can effectively block APOE4-promoted HMGB1 translocation in hippocampal neurons. To determine whether the small molecules could also reduce the release of HMGB1 from cells, we collected the hippocampal interstitial fluid (ISF) from 9.5-month-old PS19-E4 mice that had underwent a 3-week treatment with EP + GA using *in vivo* microdialysis[108]. We quantitatively determined the levels of extracellular HMGB1 protein in the ISF using sandwich ELISA.

Encouragingly, PS19-E4 mice treated with EP + GA significantly reduced HMGB1 protein within their hippocampal ISF compared to untreated PS19-E4 mice (**Fig. 2.6E,F**). This indicates that EP + GA can effectively inhibit the nucleo-cytoplasmic translocation and cellular release of HMGB1. As such, we will refer to EP + GA collectively as HMGB1 inhibitors below.

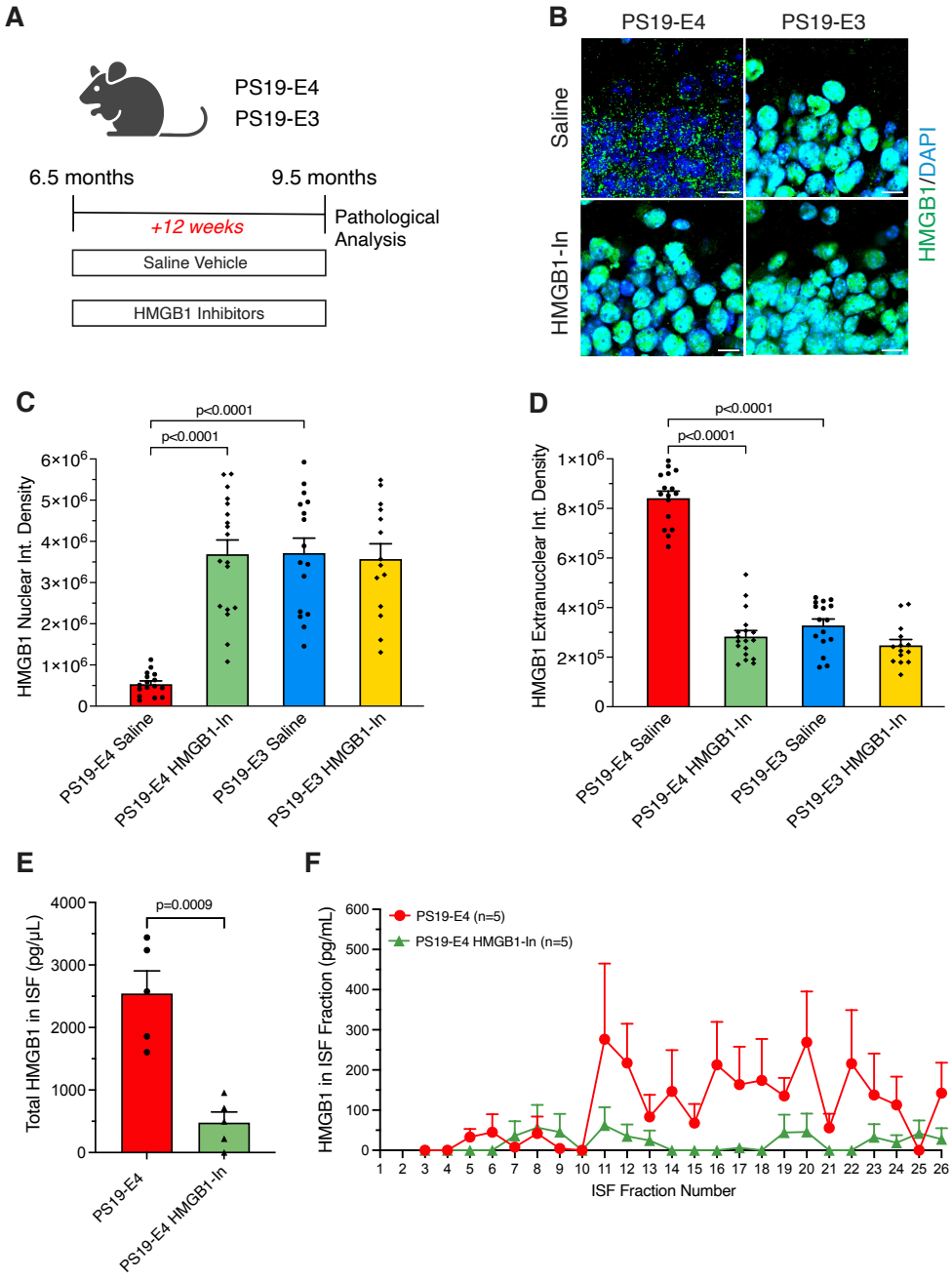

Figure 2.6. Treatment of PS19-E4 mice with HMGB1 inhibitors blocks the nucleo-cytoplasmic translocation of HMGB1 in hippocampal neurons. A, Experimental design of the HMGB1 inhibitor study illustrating the 12-week treatment period of PS19-E4 and PS19-E3 mice with either a 0.9% saline vehicle or HMGB1 inhibitors (a mixture of 80mg/kg of ethyl pyruvate and 20mg/kg of glycyrrhizic acid dissolved in 0.9% saline), starting at 6.5 months of age and ending at 9.5 months of age. **B**, Representative high magnification images of immunostaining with anti-HMGB1 and DAPI in the dentate gyrus of saline- or HMGB1 inhibitor-treated mice (scale bar, 10 µm). **C,D**, Quantification of nuclear integrated density (C) and extranuclear integrated density (D) of HMGB1 immunostaining in hippocampal neurons of saline- or HMGB1 inhibitor-treated mice. **E**, Total extracellular HMGB1 protein levels measured by ELISA in the hippocampal interstitial

fluid (ISF) of HMGB1 inhibitor-treated PS19-E4 mice. **F**, Extracellular HMGB1 protein levels measured by ELISA in each collected ISF fraction of HMGB1inhibitor-treated PS19-E4 mice. Fractions 1-2 were excluded from analyses in E,F. For representative images and quantified data, mice were 9.5-months-old and belonged to either the PS19-E4 or PS19-E3 genotype groups treated with saline or HMGB1 inhibitors. Quantified data in C,D (PS19-E4 saline, n=16; PS19-E4 HMGB1-In, n=18; PS19-E3 saline, n=16, PS19-E3 HMGB1-In, n=14) are represented as mean±SEM, one-way ANOVA with Tukey's post hoc multiple comparisons test. Quantified data in E,F (PS19-E4, n=5; PS19-E4 HMGB1-In, n=5) and are represented as mean±SEM, unpaired two-sided t test. HMGB1-In, HMGB1-Inhibitors.

Treatment with HMGB1 inhibitors ameliorates APOE4-driven gliosis

Next, we evaluated the effect of HMGB1 inhibitor treatment on APOE4-driven gliosis. Saline-treated PS19-E4 mice displayed considerable microgliosis, as exemplified by high coverage areas of Iba1$^+$ microglia (**Fig. 2.7A,B**) and CD68$^+$ activated microglia (**Fig. 2.7C,D**), whereas HMGB1 inhibitor-treated PS19-E4 mice displayed a significant decrease in microgliosis (**Fig. 2.7A-D).** Furthermore, immunostaining with anti-GFAP and anti-S100β revealed that saline-treated PS19-E4 mice had a high coverage area of GFAP$^+$ astrocytes (**Fig. 2.7E,F**) and S100β$^+$ activated astrocytes (**Fig. 2.7G,H**) throughout the hippocampus, which was significantly reduced following treatment with HMGB1 inhibitors. PS19-E3 mice did not display significant differences in microgliosis or astrogliosis whether treated with saline or HMGB1 inhibitors (**Fig. 2.7A-F**). These findings demonstrate that HMGB1 inhibitors ameliorate APOE4-driven gliosis.

Treatment with HMGB1 inhibitors ameliorates APOE4-driven Tau pathology, myelin deficits, and neurodegeneration

Since the HMGB1 inhibitors were effective at preventing APOE4-driven HMGB1 translocation and gliosis, we then sought to determine whether the inhibitors are also effective at protecting against the development of other AD-relevant pathologies. We first evaluated the extent of Tau pathology in these mice by immunostaining for AT8$^+$ pTau. PS19-E4 mice treated with saline exhibited substantial Tau pathology throughout the hippocampus, whereas PS19-E4 mice treated with HMGB1 inhibitors had a drastic reduction in Tau pathology (**Fig. 2.8A,B**). Furthermore, we determined the effectiveness of HMGB1 inhibitors in combating myelin deficits by immunostaining for MBP. Saline-treated PS19-E4 mice displayed severe myelin loss in the stratum radiatum of CA1, while HMGB1 inhibitor-treated PS19-E4 mice displayed a rescue of the deficit with a high coverage area of MBP (**Fig. 2.8C,D**). There were no discernable differences in Tau pathology or myelin coverage area between saline- and inhibitor-treated PS19-E3 mice (**Fig. 2.8A-D**).

We also determined the effectiveness of HMGB1 inhibitors at preventing APOE4-driven neurodegeneration by quantifying the hippocampal and posterior lateral ventricle volumes. Saline-treated PS19-E4 mice displayed considerable neurodegeneration, whereas HMGB1 inhibitor-treated PS19-E4 mice exhibited a rescue of neurodegeneration through a significant increase in hippocampal volumes and a significant decrease in posterior lateral ventricle volumes (**Fig. 2.8E,G**). There were no obvious differences in neurodegeneration between saline- and HMGB1 inhibitor-treated PS19-E3 mice (**Fig. 2.8E,G**).

In summation, these findings illustrate that treatment of PS19-E4 mice with HMGB1 inhibitors can effectively block the nucleo-cytoplasmic translocation of HMGB1 and prevent the development of prominent APOE4-driven pathologies, including gliosis, Tau pathology, myelin deficits, and neurodegeneration. This also provides evidence that HMGB1 inhibitors are ineffective at providing significant therapeutic effects in the context of APOE3, potentially suggesting that HMGB1 inhibitors are an APOE isoform-specific therapeutic agent.

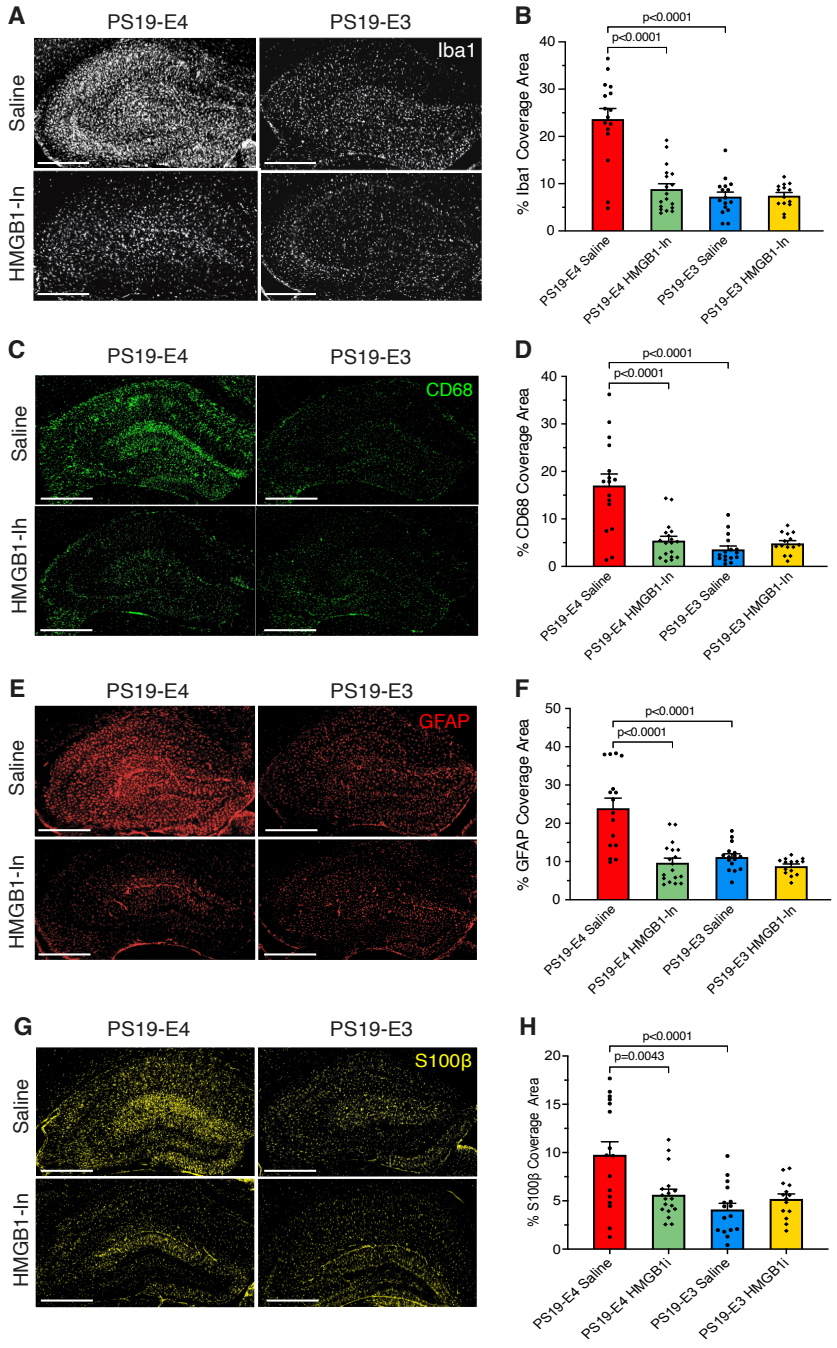

Figure 2.7. Treatment of PS19-E4 mice with HMGB1 inhibitors significantly reduces gliosis. **A**, Representative images of microglia immunostaining with anti-Iba1 in the hippocampus of saline- or HMGB1 inhibitor-treated mice (scale bar, 500 μm). **B**, Quantification of the percent Iba1 coverage area in the hippocampus of saline- or HMGB1 inhibitor-treated mice. **C**, Representative images of activated microglia immunostaining with anti-CD68 in the hippocampus of saline- or HMGB1 inhibitor-treated mice (scale bar, 500 μm). **D**, Quantification of the percent CD68 coverage area in the hippocampus of saline- or HMGB1 inhibitor-treated mice. **E**, Representative images of astrocyte immunostaining with anti-GFAP in the hippocampus of saline- or HMGB1 inhibitor-treated mice (scale bar, 500 μm). **F**, Quantification of percent GFAP coverage area in

the hippocampus of saline- or HMGB1 inhibitor-treated mice. **G**, Representative images of activated astrocyte immunostaining with anti-S100β in the hippocampus of saline- or HMGB1 inhibitor-treated mice (scale bar, 500 μm). **H**, Quantification of percent S100β coverage area in the hippocampus of saline- or HMGB1 inhibitor-treated mice. For all representative images and quantified data, mice were 9.5-months-old and belonged to either the PS19-E4 or PS19-E3 genotype groups treated with saline or HMGB1 inhibitors. Quantified data in B,D,F,H (PS19-E4 saline, n=16; PS19-E4 HMGB1-Inhibitor, n=18; PS19-E3 saline, n=16, PS19-E3 HMGB1-Inhibitor, n=14) are represented as mean±SEM, one-way ANOVA with Tukey's post hoc multiple comparisons test. HMGB1-In, HMGB1-Inhibitors.

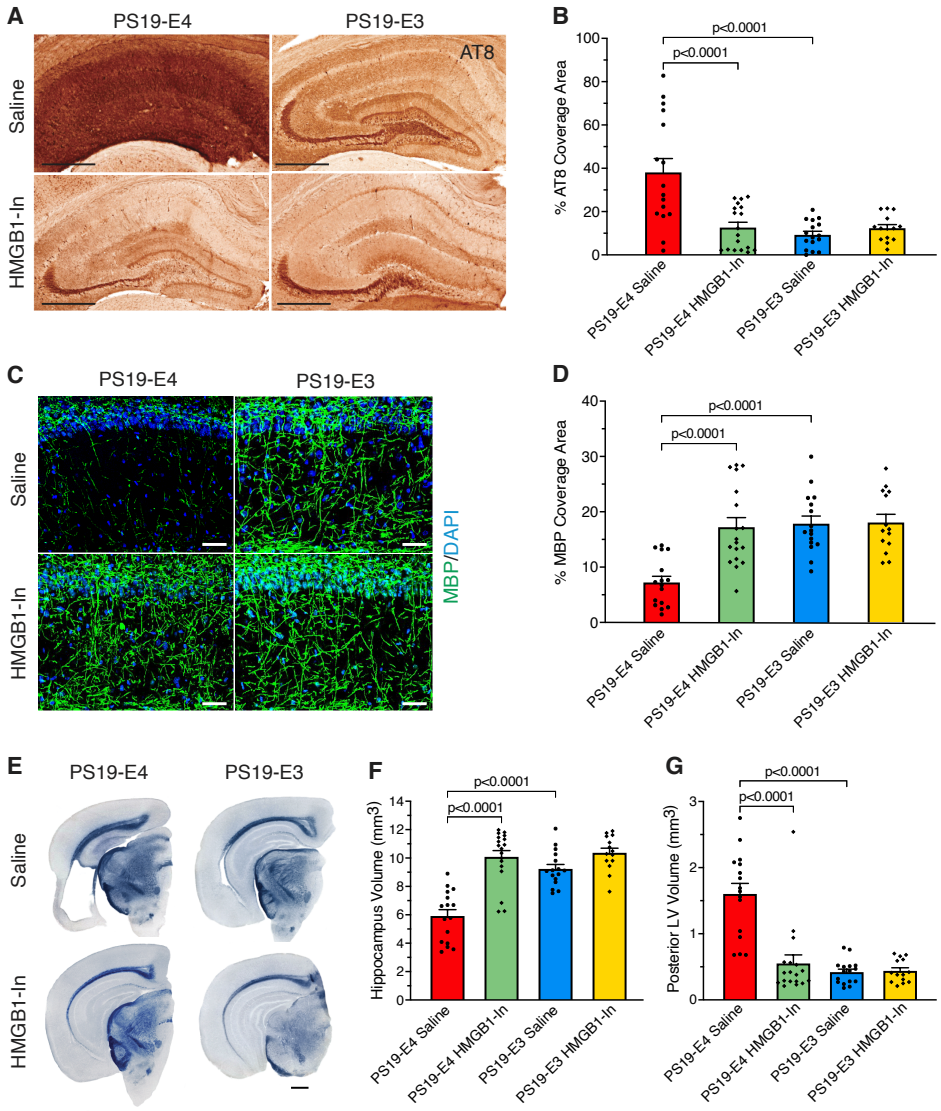

Figure 2.8. Treatment of PS19-E4 mice with HMGB1 inhibitors drastically reduces Tau pathology, myelin deficits, and neurodegeneration. A, Representative images of pTau immunostaining with anti-AT8 in the hippocampus of saline- or HMGB1 inhibitor-treated mice (scale bar, 500 µm). **B**, Quantification of percent pTau (AT8) coverage area in the hippocampus of saline- or HMGB1 inhibitor-treated mice. **C**, Representative images of myelin sheath staining with anti-MBP and DAPI in the stratum radiatum of the hippocampus underneath the pyramidal cell layer of CA1 in saline- or HMGB1 inhibitor-treated mice (scale bar, 50 µm). **D**, Quantification of the percent MBP coverage area in the hippocampal CA1 subregion of saline- or HMGB1 inhibitor-treated mice. **E**, Representative images of the ventral hippocampus of saline- or HMGB1 inhibitor-treated mice after staining with Sudan Black (scale bar, 1 mm). **F,G**, Quantification of hippocampal volume (F) and posterior lateral ventricle volume (G) in saline- or HMGB1 inhibitor-treated mice. For all representative images and quantified data, mice were 9.5-months-old and belonged to either the PS19-E4 or PS19-E3 genotype groups treated with saline or HMGB1 inhibitors. Quantified data in B,D,F,G (PS19-E4 saline, n=16; PS19-E4 HMGB1-Inhibitor, n=18; PS19-E3 saline, n=16, PS19-E3 HMGB1-Inhibitor, n=14) are represented as mean±SEM, one-way ANOVA with Tukey's post hoc multiple comparisons test. HMGB1-In, HMGB1-Inhibitors.

Discussion

In AD and other tauopathies, neuroinflammation is an important contributor to neurodegeneration[6,7,54], and APOE4 is a potent promoting factor of inflammation and gliosis[23,27,46]. Still, the mechanism by which APOE4 promotes gliosis and subsequent neurodegeneration is unclear. Since a vast majority of AD patients are carriers of APOE4[11], unraveling the mechanism of APOE4-driven pathogenesis is critically important as it would aid the development of targeted therapies to combat AD and other tauopathies in patients with the APOE4 genotype.

In the present study, we utilize a mouse model of tauopathy to demonstrate that HMGB1 plays a central role in the induction and exacerbation of APOE4-driven AD pathogenesis. Specifically, we show that [1] APOE4 leads to significantly more nucleo-cytoplasmic translocation and release of HMGB1 protein from neurons than APOE3 [2] higher amounts of extranuclear HMGB1 protein induced by APOE4 correlates to more severe microgliosis and hippocampal degeneration; [3] APOE4-driven HMGB1 cellular release acts as a potent inducer of gliosis; [4] Treatment with HMGB1 inhibitors can effectively block APOE4-induced HMGB1 translocation and release and prevent subsequent induction of gliosis; [5] Treatment with HMGB1 inhibitors also drastically reduces the extent of APOE4-driven gliosis, Tau pathology, myelin deficits, and neurodegeneration. Taken together, these findings indicate that HMGB1 plays an essential role in the pathogenic mechanism of APOE4-promoted gliosis and neurodegeneration. Importantly, we show that HMGB1 inhibitors represent a promising therapeutic agent to combat APOE4-driven AD and other tauopathies. This data also suggests that it may be important to stratify patients by APOE genotype in future clinical trials involving HMGB1 inhibitors to treat AD and other tauopathies, as we provide evidence that this treatment may offer more beneficial therapeutic effects for patients with the APOE4 genotype than APOE3 genotype.

APOE4 has a clear effect on promoting neuroinflammation in tauopathy, as our study and others have shown that it promotes microgliosis and astrogliosis in mouse models of tauopathy[7,23]. This connection between APOE4 and inflammation is maintained in humans, as analysis of post-mortem AD patient samples show a greater extent of gliosis throughout the brain [55] and higher levels of CD68 activated microglia[56] in APOE4 than APOE3 carriers. Although it was previously unclear how APOE4 induces neuroinflammation, we show that it has a compelling effect on promoting the neuronal translocation and release of HMGB1, which is a key neuroinflammatory cytokine in the brain[32,48]. While our study is the first to report this connection between APOE4 and neuronal HMGB1 translocation and release within the hippocampus, these findings complement a previous study showing that HMGB1 is released from astrocytes in the presence of Tau oligomers[41]. Although the previous study did not determine whether there is an APOE genotype-specific effect on astrocyte HMGB1 release, the APOE gene is expressed in both neurons and astrocytes[26,57], so it is possible that APOE4 would also promote the translocation of HMGB1 in astrocytes. Furthermore, we found that the relative amount of extranuclear HMGB1 in hippocampal neurons is associated with the severity of hippocampal degeneration in the context of APOE4, suggesting a link between HMGB1 translocation and neurodegeneration. This finding is in accordance with a recent study of human patients that reports an interactive effect between APOE4 and HMGB1 on reduced cortical thickness in patients with mild cognitive impairment, although this study utilized systemic levels of HMGB1 in the plasma for their comparisons and used a relatively small cohort[22]. Another study found higher levels of HMGB1 within the CSF of some AD patients relative to control individuals[39]. Considering these studies and our findings that extranuclear HMGB1 correlates with the extent of microgliosis and the severity of neurodegeneration in APOE4 mice, it is possible that HMGB1 levels in the CSF of human patients could serve as a potential biomarker of AD progression in APOE4 patients, which is worthy of further study.

While there is currently no effective treatment to slow AD progression[2], the mounting numbers of failed clinical trials for AD have raised concerns over using a one-size-fits-all approach for AD therapy and calls for a paradigm shift towards developing therapeutics that target specific genetically-driven pathogenic mechanisms[58–60]. Our study supports the notion that targeting the detrimental effects of APOE4 on HMGB1 translocation and release could serve as a therapeutic approach towards combating pathologies that are specifically driven by the APOE4 genotype. We demonstrate that treatment with two well-characterized small molecule inhibitors of HMGB1, ethyl pyruvate (EP) and glycyrrhizic acid (GA)[50–52], prevents HMGB1 translocation and release and leads to a striking reduction in a variety of prominent AD pathologies, including Tau pathology, gliosis, myelin deficits, and neurodegeneration, in APOE4 but not APOE3 tauopathy mice. These findings provide strong evidence that treatment with HMGB1 inhibitors represents a novel and effective approach towards combating APOE4-driven pathogenesis of AD and other tauopathies.

This study also has limitations to consider. While the PS19 mouse model used in this study are widely utilized as a valuable tauopathy model to study AD *in vivo*, this model does not entirely recapitulate the disease processes that occur in human AD. In particular, this model possesses a more virulent form of Tau that expedites disease progression and the development of pathologies compared to the slower disease progression that occurs in human AD patients. As such, the implications of this study to human disease and treatment requires further preclinical and clinical investigation. Furthermore, ethyl pyruvate and glycyrrhizic acid are both classified as GRAS (generally regarded as safe) by the U.S. Food and Drug administration (FDA), are found to be safe in humans at clinically relevant doses, and can easily cross the blood brain barrier in humans[61–65]. However, more work needs to be done to determine the correct dosage and proper route of administration of these inhibitors within humans to maintain effectiveness against APOE4-driven HMGB1 translocation and release in future clinical trials. Furthermore, we initiated treatment with HMGB1 inhibitors when the tauopathy mice were 6.5-months-old, which is before

they develop severe gliosis or degeneration phenotypes[44]. When considering the treatment of human APOE4 AD patients with HMGB1 inhibitors, it will be important to consider at which stage in the disease the inhibitors will be most effective. It is reasonable to suspect that HMGB1 inhibitors would be most effective prior to the onset of severe pathology, such as in APOE4 patients diagnosed with mild cognitive impairment. Still, it is possible that the inhibitors would also help slow disease progression even in AD patients that present with severe pathology since the inhibitors may reduce gliosis and mitigate further neurodegeneration, although this requires additional investigation.

In conclusion, our study identifies HMGB1 translocation and release as a key player in the pathogenic mechanism of APOE4-promoted gliosis, Tau pathology, myelin deficits, and neurodegeneration. This work further reinforces the idea that the disease processes occurring in the context of the APOE4 or the APOE3 genotype differ from one another, as we show that HMGB1 translocation and release is more strongly induced by APOE4 than APOE3 mice and that treatment with HMGB1 inhibitors only provide significant therapeutic effects in APOE4-expressing tauopathy mice. Therefore, HMGB1 inhibitors represent a promising and effective therapeutic approach towards combating APOE4-driven AD and other tauopathies.

References

1. Huang, Y. & Mucke, L. Alzheimer mechanisms and therapeutic strategies. *Cell* vol. 148 1204–1222
2. Marasco, R. A. Current and evolving treatment strategies for the Alzheimer disease continuum. *Am J Manag Care* **26**, S167–S176 (2020).
3. Chang, C.-W., Shao, E. & Mucke, L. Tau: Enabler of diverse brain disorders and target of rapidly evolving therapeutic strategies. *Science* **371**, eabb8255 (2021).
4. Ballatore, C., Lee, V. M. Y. & Trojanowski, J. Q. Tau-mediated neurodegeneration in Alzheimer's disease and related disorders. *Nat Rev Neurosci* **8**, 663–672 (2007).
5. Kosik, K. S. & Shimura, H. Phosphorylated tau and the neurodegenerative foldopathies. *Biochim Biophys Acta* **1739**, 298–310 (2005).
6. Leyns, C. E. G. & Holtzman, D. M. Glial contributions to neurodegeneration in tauopathies. *Mol Neurodegender* **12**, 50 (2017).
7. Shi, Y. *et al.* Microglia drive APOE-dependent neurodegeneration in a tauopathy mouse model. *J Exp Med* **216**, 2546–2561 (2019).
8. Corder, E. H. *et al.* Gene dose of apolipoprotein E type 4 allele and the risk of Alzheimer's disease in late onset families. *Science* **261**, 921–923 (1993).
9. Saunders, A. M. *et al.* Association of apolipoprotein E allele ϵ4 with late-onset familial and sporadic alzheimer's disease. *Neurology* **43**, 1467–1472 (1993).
10. Lambert, J. C. *et al.* Meta-analysis of 74,046 individuals identifies 11 new susceptibility loci for Alzheimer's disease. *Nat Genet* **45**, 1452–1458 (2013).
11. Farrer, L. A. *et al.* Effects of age, sex, and ethnicity on the association between apolipoprotein E genotype and Alzheimer disease. A meta-analysis. APOE and Alzheimer Disease Meta Analysis Consortium. *JAMA* **278**, 1349–56 (1997).
12. Bales, K. R. *et al.* Lack of apolipoprotein E dramatically reduces amyloid β-peptide deposition. *Nat. Genet.* vol. 17 263–264 Preprint at https://doi.org/10.1038/ng1197-263 (1997).

13. Kim, J., Basak, J. M. & Holtzman, D. M. The role of apolipoprotein E in Alzheimer's disease. *Neuron* **63**, 287–303 (2009).

14. Kanekiyo, T., Xu, H. & Bu, G. ApoE and Aβ in Alzheimer's disease: accidental encounters or partners? *Neuron* **81**, 740–54 (2014).

15. Wang, C. *et al.* Gain of toxic apolipoprotein E4 effects in human iPSC-derived neurons is ameliorated by a small-molecule structure corrector. *Nat. Med.* **24**, 647–657 (2018).

16. Brecht, W. J. *et al.* Neuron-specific apolipoprotein E4 proteolysis is associated with increased Tau phosphorylation in brains of transgenic mice. *J Neurosci* **24**, 2527–2534 (2004).

17. Lin, Y.-T. *et al.* APOE4 causes widespread molecular and cellular alterations associated with Alzheimer's disease phenotypes in human iPSC-derived brain cell types. *Neuron* **98**, 1141-1154.e7 (2018).

18. Zhao, J. *et al.* APOE4 exacerbates synapse loss and neurodegeneration in Alzheimer's disease patient iPSC-derived cerebral organoids. *Nat Commun* **11**, 1–14 (2020).

19. Muth, C., Hartmann, A., Sepulveda-Falla, D., Glatzel, M. & Krasemann, S. Phagocytosis of apoptotic cells is specifically upregulated in apoe4 expressing microglia in vitro. *Front Cell Neurosci* **13**, 181 (2019).

20. Koutsodendris, N., Nelson, M. R., Rao, A. & Huang, Y. Apolipoprotein E and Alzheimer's disease: findings, hypotheses, and potential mechanisms. *Ann Rev Pathol* **17**, 73–99 (2022).

21. Mishra, S. *et al.* Longitudinal brain imaging in preclinical Alzheimer disease: Impact of APOE ϵ4 genotype. *Brain* **141**, 1828–1839 (2018).

22. Operto, G. *et al.* Interactive effect of age and APOE-E4 allele load on white matter myelin content in cognitively normal middle-aged subjects. *Neuroimage Clin* **24**, 101983 (2019).

23. Shi, Y. *et al.* ApoE4 markedly exacerbates tau-mediated neurodegeneration in a mouse model of tauopathy. *Nature* **549**, 523–527 (2017).

24. Buttini, M. *et al.* Expression of human apolipoprotein E3 or E4 in the brains of Apoe−/− mice: isoform-specific effects on neurodegeneration. *J Neurosci* **19**, 4867–4880 (1999).

25. Andrews-Zwilling, Y. *et al.* Apolipoprotein E4 causes age-and Tau-dependent impairment of GABAergic interneurons, leading to learning and memory deficits in mice. *J Neurosci* **30**, 13707–13717 (2010).

26. Zalocusky, K. A. *et al.* Neuronal apoE upregulates MHC pathways to drive selective neurodegeneration in Alzheimer's disease. *Nat Neurosci* **24**, 786–798 (2021).

27. Gale, S. C. *et al.* APOε4 is associated with enhanced in vivo innate immune responses in human subjects. *J. Allergy Clin. Immunol.* **134**, 127–134 (2014).

28. Maroso, M. *et al.* Toll-like receptor 4 and high-mobility group box-1 are involved in ictogenesis and can be targeted to reduce seizures. *Nat Med* **16**, 413–419 (2010).

29. Okuma, Y. *et al.* Anti-high mobility group box-1 antibody therapy for traumatic brain injury. *Ann Neurol* **72**, 373–384 (2012).

30. Sasaki, T. *et al.* Anti-high mobility group box 1 antibody exerts neuroprotection in a rat model of Parkinson's disease. *Exp Neurol* **275 Pt 1**, 220–231 (2016).

31. Andersson, A. *et al.* Pivotal advance: HMGB1 expression in active lesions of human and experimental multiple sclerosis. *J Leukoc Biol* **84**, 1248–1255 (2008).

32. Magna, M. & Pisetsky, D. S. The role of HMGB1 in the pathogenesis of inflammatory and autoimmune diseases. *Mol Med* **20**, 138–146 (2014).

33. Naglova, H. & Bucova, M. HMGB1 and its physiological and pathological roles. *Bratisl Lek Listy* **113**, 163–171 (2012).

34. Rovere-Querini, P. *et al.* HMGB1 is an endogenous immune adjuvant released by necrotic cells. *EMBO Rep* **5**, 825–830 (2004).

35. Paudel, Y. N. *et al.* HMGB1: A common biomarker and potential target for TBI, neuroinflammation, epilepsy, and cognitive dysfunction. *Front Neurosci* **12**, 628 (2018).

36. Bianchi, M. E. *et al.* High-mobility group box 1 protein orchestrates responses to tissue damage via inflammation, innate and adaptive immunity, and tissue repair. *Immunol Rev* **280**, 74–82 (2017).

37. Scaffidi, P., Misteli, T. & Bianchi, M. E. Release of chromatin protein HMGB1 by necrotic cells triggers inflammation. *Nature* **418**, 191–195 (2002).

38. Gauley, J. & Pisetsky, D. S. The translocation of HMGB1 during cell activation and cell death. *Autoimmunity* **42**, 299–301 (2009).

39. Fujita, K. *et al.* HMGB1, a pathogenic molecule that induces neurite degeneration via TLR4-MARCKS, is a potential therapeutic target for Alzheimer's disease. *Sci Rep* **6**, 31895 (2016).

40. Nan, K. *et al.* HMGB1 gene silencing inhibits neuroinflammation via down-regulation of NF-κB signaling in primary hippocampal neurons induced by Aβ 25-35. *Int Immunopharmacol* **67**, 294–301 (2019).

41. Gaikwad, S. *et al.* Tau oligomer induced HMGB1 release contributes to cellular senescence and neuropathology linked to Alzheimer's disease and frontotemporal dementia. *Cell Rep.* **36**, 109419 (2021).

42. Saunders, A. M. *et al.* Apolipoprotein E epsilon 4 allele distributions in late-onset Alzheimer's disease and in other amyloid-forming diseases. *Lancet* **342**, 710–711 (1993).

43. Bien-Ly, N., Gillespie, A. K., Walker, D., Yoon, S. Y. & Huang, Y. Reducing human apolipoprotein E levels attenuates age-aependent Aβ accumulation in mutant human amyloid precursor protein transgenic mice. *J Neurosci* **32**, 4803–4811 (2012).

44. Yoshiyama, Y. *et al.* Synapse loss and microglial activation precede tangles in a P301S tauopathy mouse model. *Neuron* **53**, 337–351 (2007).

45. Zhao, J. *et al.* APOE4 exacerbates synapse loss and neurodegeneration in Alzheimer's disease patient iPSC-derived cerebral organoids. *Nat. Commun.* **11**, 1–14 (2020).

46. Zhu, Y. *et al.* APOE genotype alters glial activation and loss of synaptic markers in mice. *GLIA* **60**, 559–569 (2012).

47. Yamada, K. *et al.* In vivo microdialysis reveals age-dependent decrease of brain interstitial fluid tau levels in P301S human hau transgenic mice. *J. Neurosci.* **31**, 13110–13117 (2011).

48. Yang, H., Wang, H., Czura, C. J. & Tracey, K. J. The cytokine activity of HMGB1. *J Leukoc Biol* **78**, 1–8 (2005).

49. Knoferle, J. *et al.* Apolipoprotein E4 produced in GABAergic interneurons causes learning and memory deficits in mice. *J. Neurosci.* **34**, 14069–14078 (2014).

50. Ulloa, L. *et al.* Ethyl pyruvate prevents lethality in mice with established lethal sepsis and systemic inflammation. *Proc Natl Acad Sci USA* **99**, 12351–12356 (2002).

51. Sun, Y. *et al.* Glycyrrhizin protects mice against experimental autoimmune encephalomyelitis by inhibiting high-Mobility group Box 1 (HMGB1) expression and neuronal HMGB1 release. *Front Immunol* **9**, 1518 (2018).

52. Mollica, L. *et al.* Glycyrrhizin binds to high-mobility group box 1 protein and inhibits its cytokine activities. *Chem Biol* **14**, 431–41 (2007).

53. Davé, S. H. *et al.* Ethyl pyruvate decreases HMGB1 release and ameliorates murine colitis. *J Leukoc Biol* **86**, 633–643 (2009).

54. Malpetti, M. *et al.* Neuroinflammation predicts disease progression in progressive supranuclear palsy. *J Neurol Neurosurg Psychiatry* **92**, 769–775 (2021).

55. Egensperger, R., Kösel, S., Von Eitzen, U. & Graeber, M. B. Microglial activation in Alzheimer disease: association with APOE genotype. *Brain Pathol* **8**, 439–447 (1998).

56. Minett, T. *et al.* Microglial immunophenotype in dementia with Alzheimer's pathology. *J Neuroinflammation* **13**, 135 (2016).

57. Xu, Q. *et al.* Profile and regulation of apolipoprotein E (ApoE) expression in the CNS in mice with targeting of green fluorescent protein gene to the apoE locus. *J Neurosci* **26**, 4985–4994 (2006).

58. Safieh, M., Korczyn, A. D. & Michaelson, D. M. ApoE4: an emerging therapeutic target for Alzheimer's disease. *BMC Med* **17**, 1–17 (2019).

59. Yamazaki, Y., Painter, M. M., Bu, G. & Kanekiyo, T. Apolipoprotein E as a therapeutic target in Alzheimer's disease: a review of basic research and clinical evidence. *CNS Drugs* **30**, 773–789 (2016).

60. Kosik, K. S., Sejnowski, T. J., Raichle, M. E., Ciechanover, A. & Baltimore, D. A path toward understanding neurodegeneration. **6302**, 872–3 (2016).

61. Bennett-Guerrero, E. *et al.* A phase II multicenter double-blind placebo-controlled study of ethyl pyruvate in high-risk patients undergoing cardiac surgery with cardiopulmonary bypass. *J Cardiothorac Vasc Anesth* **23**, 324–329 (2009).

62. Kwon, Y. J., Son, D. H., Chung, T. H. & Lee, Y. J. A Review of the Pharmacological Efficacy and Safety of Licorice Root from Corroborative Clinical Trial Findings. *J Med Food* **23**, 12–20 (2020).

63. Petramfar, P., Hajari, F., Yousefi, G., Azadi, S. & Hamedi, A. Efficacy of oral administration of licorice as an adjunct therapy on improving the symptoms of patients with Parkinson's disease, A randomized double blinded clinical trial. *J Ethnopharmacol* **247**, 112226 (2020).

64. Cao, Z. Y. *et al.* Glycyrrhizic acid as an adjunctive treatment for depression through anti-inflammation: A randomized placebo-controlled clinical trial. *J Affect Disord* **265**, 247–254 (2020).

65. Worku, N. *et al.* Ethyl Pyruvate Emerges as a Safe and Fast Acting Agent against Trypanosoma brucei by Targeting Pyruvate Kinase Activity. *PLOS ONE* **10**, e0137353 (2015).

Conclusions and Future Directions

All in all, our work has provided key insights into the pathogenic mechanisms of APOE4-driven AD, highlighting two critical players involved in promoting the development of prominent APOE4-related AD pathologies. First, we demonstrate that neuronal APOE4 plays a major role in promoting Tau pathology accumulation and spread, neurodegeneration, gliosis, myelin deficits, and neurodysfucntion. We also observed that neuronal APOE4 leads to the enrichment of neurodegenerative disease-associated subpopulations of neurons, oligodendrocytes, astrocytes, and microglia, as its removal diminishes the presence of these disease-associated cell subpopulations. Second, we provide evidence that HMGB1 plays a central role in the induction of APOE4-promoted glial activation and subsequent degenerative phenotypes. We also show that the blocking HMGB1 translocation and release utilizing small molecule inhibitors can effectively prevent the development of AD-related pathologies in APOE4 tauopathy mice.

These studies provide important insights into the pathogenic mechanisms of APOE4-driven AD, however, there are still several outstanding questions. First, APOE can be produced in a variety of cell types, including astrocytes, neurons, microglia, and oligodendrocytes. Our study and others have shown that neuronal and astrocytic APOE4 exert detrimental effects, with some overlapping pathogenic effects and some detrimental effects that have only been observed for neuronal APOE4. There is also a lack of knowledge on the detrimental effects of APOE4 from microglia and oligodendrocytes on Tau pathology and neurodegeneration. It would be important to study the effects of APOE4 from these glial cell types so we can expand our current understanding of APOE biology and potentially uncover new therapeutic targets for AD. In addition to expanding our understanding of the detrimental effects of APOE4 from a variety of cell types, it would also be interesting to investigate any beneficial effects exerted by APOE depending on the cellular origin of its production. This would further inform our understanding of why these cell types, especially neurons, microglia, and oligodendrocytes, upregulate APOE during conditions of stress

or injury as a potential compensation method to combat the injury and help define the molecular processes that go awry and lead to detrimental effects. Gaining these mechanistic insights could allow us to develop therapeutics that boost identified compensation methods or inhibit the processes that lead to detrimental effects.

Second, our studies show that HMGB1 plays an important role in promoting glial activation in AD. Further work is required to understand the mechanism responsible for APOE4-induced translocation and release of HMGB1 and to better define the relationship between HMGB1 and APOE in different stages of the disease in human patients. Our studies suggest that HMGB1 triggers glial activation, but it is unclear at which stage in the disease APOE4-promoted HMGB1 translocation and release occurs within human patients, such as during the prodromal phase, pre-clinical AD, or during advanced AD. Understanding when this pathogenic change in HMGB1 occurs would help inform future clinical trials targeting the release of HMGB1. Furthermore, it would be interesting to better define the relationship between HMGB1 and APOE in different cell types. We show here that HMGB1 aberrantly translocates in neurons, potentially suggesting that dead or dying neurons play a critical role in glial activation. Other studies have suggested that HMGB1 translocation in astrocytes may play a role as well, while HMGB1 translocation in microglia and oligodendrocytes has not yet been studied in the context of AD. It would be interesting to investigate which cell type most prominently induces HMGB1 release, if the release of HMGB1 is triggered equally by APOE4 in all cell types, or if different pathological triggers are required for HMGB1 release in different cell types.

In conclusion, we demonstrate that neuronal APOE4 and HMGB1 play important roles in the pathogenic mechanisms of APOE4-driven AD. These findings provide key insights into our understanding of APOE4 biology and its cellular and molecular mechanisms in AD. Finally, our studies also identify new therapeutic targets that can be utilized to effectively combat AD.

Publishing Agreement

It is the policy of the University to encourage open access and broad distribution of all theses, dissertations, and manuscripts. The Graduate Division will facilitate the distribution of UCSF theses, dissertations, and manuscripts to the UCSF Library for open access and distribution. UCSF will make such theses, dissertations, and manuscripts accessible to the public and will take reasonable steps to preserve these works in perpetuity.

I hereby grant the non-exclusive, perpetual right to The Regents of the University of California to reproduce, publicly display, distribute, preserve, and publish copies of my thesis, dissertation, or manuscript in any form or media, now existing or later derived, including access online for teaching, research, and public service purposes.

DocuSigned by:
Nicole Koutsodendris
2F8ECD3508C3449...
Author Signature

10/21/2022
Date